NUMERICAL SOLUTION OF AXIAL-MODE INSTABILITY PROBLEMS IN SOLID PROPELLANT ROCKET MOTORS

A THESIS

Presented to

The Faculty of the Division of Graduate

Studies and Research

By

Douglas Edward Kooker

In Partial Fulfillment

of the Requirements for the Degree

Doctor of Philosophy

in the School of Aerospace Engineering

Georgia Institute of Technology

November, 1973

NUMERICAL SOLUTION OF AXIAL-MODE INSTABILITY PROBLEMS

IN SOLID PROPELLANT ROCKET MOTORS

Approved:

Ben T. Zinn, Chairman

Warren C. Strahle

James C. Wu

Date approved by Chairman: Nov. 14, 1973

ACKNOWLEDGEMENTS

I would like to express my appreciation to Prof. Ben T. Zinn for his guidance, encouragement, and many helpful discussions during the course of this research. I would also like to thank Profs. B. T. Zinn, W. C. Strahle, and J. C. Wu for their careful reading of this manuscript, and for their many useful suggestions.

A special word of thanks is due to Dr. Warren C. Strahle who patiently answered an endless stream of questions concerning the solid propellant combustion process.

The completion of this research would have been impossible without the financial support provided by a three-year NDEA fellowship and the Georgia Institute of Technology. This support is gratefully acknowledged.

TABLE OF CONTENTS

LIST OF ILLUSTRATIONS

Figure Page

NOMENCLATURE

a	$(a^*/a_r^*, \sqrt{p/\rho}\,)$, speed of sound (also, constant in burning rate law $r = ap^n$)
A	(A^*/A_{ch}^*), cross sectional area
A_{ch}^*	chamber reference area
A_p	control volume perimeter surface area
$b(t)$	(ξ-space) location of left-hand boundary of flow field region
B_r	$(B_r^*/a_r^* \hat{y}_c)$, frequency factor in Arrhenius surface reaction
$c(t)$	(ξ-space) location of right-hand boundary of flow field region
c_p^*	specific heat at constant pressure of gaseous combustion products
c_s^*	specific heat of solid propellant material
c_v^*	specific heat at constant volume of gaseous combustion products
c.s.	control surface
c.v.	control volume
c.s.p.	control surface perimeter
$\tilde{D}$	discriminant defined in Equation (2.50)
e	$(e^*/c_v^* T_r^*)$, specific internal energy of gas
E_f^*	activation energy of Arrhenius flame reaction
E_s^*	activation energy of Arrhenius surface reaction

$\sum \vec{F}$	sum of the forces acting on control surface due to surroundings
$\hat{G}$	represents boundary condition Equation (3.20)(c) at time "n"
h	$(h^*/c_p^* T_r^*,\ p/\rho)$ specific enthalpy of gas
h_c	enthalpy of combustion products entering control volume from flame zone
h_{con}	convective heat transfer coefficient
k_g^*	thermal conductivity of combustion products
k_s^*	thermal conductivity of solid propellant material
K	$\left(\frac{9}{2} \frac{\mu^* L^*}{\rho_m^* \sigma^{*2} a_r^*} \right)$, constant which follows from Stokes Flow Drag Law
L^*	axial reference length
$\dot{m}$	$(\dot{m}^*/\rho_r^* a_r^*)$, propellant surface mass flow rate per unit surface area
$\dot{m}_g$	$(\dot{m}_g^*/\rho_r^* a_r^*)$, mass flow rate of gas per unit surface area
$\dot{m}_p$	$(\dot{m}_p^*/\rho_r^* a_r^*)$, mass flow rate of particles per unit surface area
M	(u/a), Mach number
n	reaction index
p	(p^*/p_r^*), pressure
$\dot{q}_{surface}$	heat transfer rate to propellant surface
$\hat{Q}$	defined in Equation (3.11)
Q_f^*	exothermic heat release in flame reaction
Q_s^*	endothermic heat release in surface reaction

r	$(r^*/a_r^* \hat{y}_c)$, propellant surface regression rate
$\bar{r}$	value of r when no disturbances are present
R	(R^*/R_{ch}^*), local chamber radius
$\mathcal{R}$	$\left(\frac{\dot{m}'/\bar{\dot{m}}}{p'/\bar{p}} \right)$, combustion response function
	the real part is computed from the numerical solution as
	$\left(\frac{\Delta\dot{m}/\bar{\dot{m}}}{\Delta p/\bar{p}} \right)$
$\bar{R}$	$R(R_{ch}^*/L^*)$
$R_1, \ldots R_5$	defined in Equations (2.9) through (2.13)
R_{ch}^*	$\sqrt{A_{ch}^*/\pi}$, radial reference length
R_{gas}	(R_o/W^*), gas constant
R_o	universal gas constant
S	entropy of gas, defined in Equation (2.14)
t, T	$(t^* a_r^*/L^*)$, time
$\bar{t}$	(t/period of wave)
T	(T^*/T_r^*), temperature
$\hat{T}(y)$	defined before Equation (3.23)
T_{af}^*	adiabatic flame temperature
T_f^*	flame temperature
T_{cs}^*	temperature of cold solid propellant
T_{sur}^*	temperature of surface of burning propellant
u	(u^*/a_r^*), velocity of gas
u_p	(u_p^*/a_r^*), velocity of solid particles
U, U_p	transformed velocities defined in Equations (2.17) and (2.18), respectively

$v(y)$	$\hat{T}'$, see Equation (3.27)
v_g^*	velocity of gas normal to propellant surface in flame
w_s	shock wave velocity relative to fixed coordinates
W^*	molecular weight
x	(x^*/L^*), axial coordinate
X	transformed axial coordinate defined in Equation (2.15)
y	$(y^*/L^*\hat{y}_c)$, coordinate normal to regressing propellant surface
$\hat{y}_c$	$(k_s^*/\rho_s^* c_s^* a_r^* L^*)^{\frac{1}{2}}$
y_f^*	location of edge of flame
$Z_1(Q_s^*)$	$(Q_s^*/c_s^* T_r^*)$
$Z_2(Q_f^*)$	$[(k_g^* Q_f^* L^*)/(k_s^* c_p^* T_r^* \rho_s^* a_r^*)]\ \omega^*(t)$
α	$(\dot{m}^* c_p^* L^* \hat{y}_c/k_g^*)$
β	defined in Equation (2.16)
γ	isentropic index
η	$(d\xi/dx)/(c-b)$
$\theta(y)$	defined by Equation (3.32)
λ	thermal conductivity of solid propellant
λ	complex function of frequency, Ω (solution of, $\lambda(\lambda - 1) = i\Omega$)
ξ	$\xi = \xi(x)$, stretched axial coordinate
ξ_1, ξ_2, ξ_d	defined in Equation (3.40)
ρ	(ρ^*/ρ_r^*), density of gas
ρ_p	(ρ_p^*/ρ_r^*), density of solid particles in chamber volume
$\hat{\rho}_m^*$	density of solid particle material
ρ_s^*	solid propellant density

σ^*	average particle diameter
ω	$(\omega^* L^*/a_r^*)$, frequency
$\omega^*(t)$	reaction rate in gas phase flame
Ω	$(\omega/\sqrt{r^2})$

Superscripts

*	dimensional quantity
'	time-varying fluctuation

Subscripts

g	gas phase
p	solid particles
r	reference state
s	solid propellant material

SUMMARY

Nonlinear axial-mode combustion instability remains a serious problem in the development of solid propellant rocket motors. Although the use of metal-loaded solid propellants which produce solid particles in the flow has reduced the occurrence of high frequency instabilities, it has not eliminated the axial-mode intermediate frequency (100 - 1000 Hz.) problem. If such an instability reaches a large amplitude limit cycle, it may lead to an increase in mean chamber pressure and burning rate, excessive heat transfer rates, and a severe vibration level. The objective of this dissertation is to investigate the complex coupling between the chamber flow conditions and the solid propellant combustion process which may lead to large amplitude longitudinal instabilities.

This is accomplished by obtaining numerical solutions to the time-dependent conservation equations describing the one-dimensional two-phase flow in a solid rocket combustion chamber and choked nozzle system. The solution includes the unsteady flow in the nozzle, eliminating the need for an artificial nozzle boundary condition. Permissible flow field solutions include shock wave initial disturbances as well as shock waves resulting from the interaction of continuous disturbances with the combustion process. The equations governing the time-dependent pressure-coupled combustion process are solved simultaneously with the unsteady chamber flow at a series of burning stations along the propellant grain.

Predictions of the engine response to various amplitude disturbances indicate that:

(1) Small amplitude pressure oscillations in the solid propellant flame zone can lead to large amplitude spikes in propellant burning rate.

(2) A propellant system which operates on the lead portion of the combustion response curve is considerably more effective in sustaining large amplitude axial instabilities than one which operates on the lag portion of the curve.

(3) The combustion response due to pressure coupling alone has the potential for driving small amplitude disturbances in the rocket engine into large amplitude axial instabilities.

CHAPTER I

INTRODUCTION

General Introduction and Perspective

The full-thrust operating characteristics of solid propellant rocket motors are never completely time-independent. The performance of the system is acceptable with a certain amount of rough combustion, defined as small amplitude unorganized flow field oscillations. On occasion, larger amplitude organized disturbances appear in the combustion chamber and nozzle flow field during the ignition transient or after full-thrust has been obtained. If such an instability reaches a large amplitude limit cycle, it may lead to an increase in mean chamber pressure and burning rate, excessive heat transfer rates, and a severe vibration level. The occurrence of any one of these may result in malfunction or destruction of the engine.

Organized oscillations are evidence of a positive feedback between the propellant combustion process and the flow field disturbance. As noted by Price [1], a rocket motor is like a self-excited oscillator where combustion is the energy source, the flow in the combustion chamber and nozzle is the oscillator, and the propellant burning rate sensitivity to flow field disturbances is the coupling between the two. A combustion instability analysis seeks to describe how this interaction occurs, determine what combination of system parameters may lead to an unstable situation, and suggest ways it might be counteracted.

In general, rocket motor instabilities can occur in longitudinal, radial, or transverse modes at frequencies which are close to the natural acoustic frequencies of the combustion chamber. Many solid propellant rocket motors are prone to undersirable axial-mode or longitudinal instabilities in an intermediate frequency range [2] of 100 to 1000 Hz. The infrequent occurrence of high frequency modes can be attributed to the use of metalized propellants which produce solid particles in the gas flow. In these cases, the resultant drag between gas and particles and its associated energy dissipation contribute a large damping effect to the unsteady motion in the chamber. However, experimental observation and analytical considerations indicate that particulate damping is ineffective in controlling axial mode intermediate frequency instabilities. In certain instances, solid rocket engines have shown an increased susceptibility [3] to axial-mode instabilities as the metal content of the propellant is increased.

Longitudinal instabilities normally arise spontaneously, presumably triggered by the presence of small amplitude unorganized disturbances in the combustion chamber, or by a momentary flow blockage due to a solid fragment exhausting through the nozzle. Attempts to isolate controlling parameters and establish stability trends by firing full-scale engines become prohibitively expensive. Outside of a few reported cases [4-6] of instability in full-scale engines, most experimental data has been gathered from laboratory tests of small-scale motors. A very extensive investigation [7-12] has been carried out at the Canadian Armament Research and Development Establishment (CARDE) to determine the effect of chamber diameter, length, throat-to-port area ratio,

initial propellant temperature and composition of the propellant. Similar work has been conducted at Stanford Research Institute [13,14].

It was observed in References 7 and 8 that once a motor is operating in an unstable manner, its behavior is independent of the process which initiated the instability. Thus, except for a short initiation transient, artifical triggering produced the same engine response found in the spontaneous cases. In the above experiments [7-12], the ultimate test for stability was the response of the engine flow field to a sharp "pulse" [15] created by an explosive charge placed at the head end of the combustion chamber. Several charges were exploded at predetermined times during the motor firing while the pressure-time history at the head and aft ends was recorded. With this technique, the results are a measure of the nonlinear stability of the motor; i.e., does a large amplitude disturbance decay and the flow field return to steady state, or does it lead to an increasing mean chamber pressure and burning rate, and instability in the chamber? In a recent study to assess the effect of propellant composition, Roberts and Brownlee [12] attempted to correlate the onset of unstable operation (eg., transition pressure, transition burning rate) with propellant ingredients and the severity of the disturbance. Quoting from Reference (12):

> Clearly, it is possible to investigate a particular propellant system and to establish individual trends based on selected changes to the formulation. It is also evident that such trends cannot be expected to apply to propellants containing substantially different binder or oxidizer systems.

The concluding statement is: "This result serves to underline the importance of achieving an improved understanding of the physical processes

governing longitudinal combustion instability."

The purpose of this dissertation is to develop a theoretical axial-mode model of a solid propellant rocket engine with a cylindrically perforated grain which can:

(1) predict the time-dependent behavior of the combustion chamber and nozzle flow field after the introduction of an arbitrary disturbance, i.e., simulate the experimental procedure for assessing nonlinear stability, and

(2) lead to a better understanding of the complex coupling between the chamber flow conditions and the propellant combustion process in longitudinal combustion instability.

A theoretical description of the nonlinear behavior of axial instabilities will require a flow field model with certain minimum capabilities. The need for a solution to the full unsteady conservation equations for a two-phase flow is obvious. Traveling discontinuities are acceptable solutions to these nonlinear equations and hence must be provided for. In the previously mentioned experiments, the presence of traveling shock waves, although weak ($M \lesssim 1.2$), is indicated by the pressure-time histories and confirmed by optical measurements [10]. Since the growth or decay of disturbances in the combustion chamber is often decided by a slight imbalance between the overall gain and loss processes of the system, the boundary conditions imposed upon the flow field model become very important. The choked throat of the nozzle provides the physical downstream boundary condition to disturbances in the chamber. The theoretical model must account for this effect without imposing any restrictions on the magnitude of

the mean flow Mach number or the amplitude of the disturbance. Equally important is the solution to the solid propellant combustion problem which has boundary conditions dependent on the chamber flow properties. This solution must account for the unsteadiness of the burning process without making assumptions about the type of disturbance in the chamber.

Since the combustion model is a critical part of an analysis of transient behavior inside a solid propellant rocket motor, it warrants further elaboration. Regretably, the combustion of solid propellants involves complex mechanisms which are not well understood, even in steady state. Changes in composition and heterogeneity have substantial influence on the measured values of the steady-state surface regression rate as a function of pressure. This type of effect cannot be predicted theoretically with current knowledge of the combustion process. However, the difficult theoretical problem has often been avoided by use of an empirical expression of the form,

$$\text{burning rate} \quad \alpha \quad p^n$$

or

$$r = ap^n \tag{1.1}$$

where a is a constant and n is called the pressure index. This well-known burning rate "law" resulted from the correlation of experimental steady state burning rate data and is usually applicable within a restricted pressure range. Another steady state expression,

$$\frac{1}{r} = \frac{a}{p} + \frac{b}{p^{1/3}} \qquad (1.2)$$

was suggested by the Granular Diffusion Flame (GDF) theory [16] for composite propellants. The GDF model is based on a pre-mixed kinetically controlled reaction at low pressure ($r \alpha p$) and a diffusion controlled reaction involving "pockets of fuel vapor" at high pressure ($r \alpha p^{1/3}$). With suitable values of a and b, Equation (1.2) correlates [17] certain experimental data for AP - hydrocarbon binder propellants with a unimodal oxidizer particle distribution. For arbitrary propellants though, the predictive nature of both Equation (1.1) and (1.2) must be viewed with caution.

If the burning propellant is exposed to a transient flow, as in the present study, the use of any steady state burning rate expression is open to question. This difficulty can be illustrated with a simplified description of solid propellant combustion. Consider a gaseous flame zone adjacent to a regressing propellant surface ($y = 0$) in a one-dimensional situation (Figure 1). The effect of heat released in the flame zone and at the surface (if surface reactions are present) is to determine the temperature gradient in the solid at the interface $y = 0$. With this boundary condition, the time dependent energy balance in the unburned propellant determines the temperature at the interface. The mass flow rate from the surface (α surface regression rate) is primarily a function of this temperature. Hence, a step change in

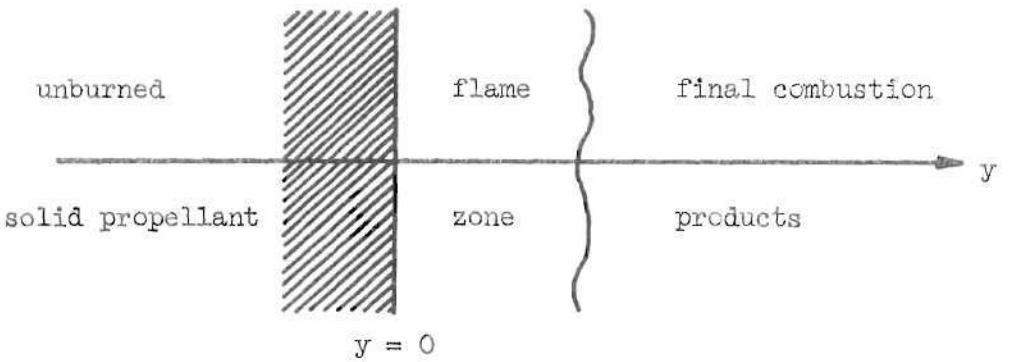

Figure 1. Typical Solid Propellant Combustion Model

pressure or temperature in the flame zone will not produce an instantaneous adjustment in surface mass flow rate. The response time (time delay) before a new equilibrium is achieved is related to the thermal wave travel time in the unburned propellant. Use of a steady state burning law implies a constant equilibrium between pressure and burning rate, which may be valid only in restrictive cases. An accurate assessment of whether a given disturbance in the combustion chamber will grow or decay must include the effect of the combustion response time.

Cheng [18-20] has analyzed solid propellant combustion with a time-lag concept inspired by Crocco's [21-23] work in liquid propellant rocket motors. The assumption is made that the mass flow rate from the surface is proportional to the pressure at a previous time, i.e.,

$$\dot{m}_g(t) \sim [p(t - \tau)]^n \qquad (1.3)$$

The time lag parameter, τ, incorporates the effect of the entire combustion process, but no method is given to compute its value. This problem also arises in the works of Grad [24] and Moore and Maslen [25] which are based on different definitions of a time lag. In addition to the fact that "τ" will be strongly dependent on the propellant properties, chamber length, type of disturbance in the chamber, flow field composition and temperature, it may also change sign. More recent analyses [26] of the solid propellant combustion response to small amplitude periodic disturbances in pressure have shown that the burning rate can lead the pressure oscillation at low frequencies. Even if a straight-forward method to compute the value of "τ" was known, the computational difficulties associated with storing flow fields obtained at previous times and then interpolating in time and space to determine the proper variable at a retarded time would be immense. Thus, the time-lag concept will not be considered in the present analysis.

A more detailed model of the combustion process is necessary to circumvent the problem of an unknown time-lag parameter. The gross features of the process can be represented by three regions: (1) the cold solid region in which a thermal wave propagates into the unburned propellant, heating the material to the surface temperature, (2) an interface region between the gas and solid phases (often treated as infinitesimal plane) in which decomposition, pyrolysis, and other surface reactions may occur, and (3) a gas-phase reaction zone (flame). Many theoretical combustion models [26], based on this interpertation of the combustion process, have been used to investigate the response of the burning propellant to small amplitude periodic pressure

disturbances. Although these models differ as to the treatment of details, they share the following simplifying assumptions:

(1) a one-dimensional homogeneous solid phase

(2) simple pyrolysis of solid to gas

(3) no condensed phase reactions

(4) quasi-steady gas phase flame zone

As demonstrated in the excellent review by Culick [26], these common assumptions are responsible for each analysis arriving at the same two-parameter form of the combustion response function, $\mathcal{R} \equiv \frac{m'/\bar{m}}{p'/\bar{p}}$, as a function of the frequency of oscillation of the disturbance. This form of the response function does predict that the surface mass flow rate as a function of time will lead a periodic pressure disturbance at low frequencies and lag at high frequencies. It also predicts a single response peak or maximum at a non-zero frequency determined by the values of the two adjustable parameters. Qualitatively, this behavior corresponds to observed experimental trends, but quantitative predictions have met with only limited success [27]. Correlation of all experimental data will undoubtedly require a very sophisticated theoretical analysis (eg., see the next paragraph) which has yet to be formulated. However, the above models have yielded considerable insight into the transient combustion response of solid propellants; hence, their basic assumptions will be adopted in the present study. But the response function derived from a linearized analysis which assumes the existance of small amplitude periodic disturbances is not applicable when arbitrary disturbances can be present in the engine flow field. The latter situation will require a time-dependent solution of the

non-linear equations which follow from the combustion model.

The above discussion of solid propellant combustion has ignored a difficult and important aspect of the problem. The unsteady propellant burning rate can be sensitive to velocity fluctuations parallel to the surface as well as pressure fluctuations in the flame zone. The former is referred to as velocity coupling. The basis for velocity coupling is often attributed to a complexity associated with the combustion of metal-loaded solid propellants - the layer of molten metal on the propellant surface. However, this is not to imply that velocity coupling must be absent if a non-metalized propellant is used. Price [28] gives the following description of the combustion of aluminized propellants:

> Because of its high boiling point, aluminum tends to accumulate on the burning surface in a condensed phase, protected from ignition by a thin layer of aluminum oxide. The aluminum leaves the burning surface primarily as agglomerates in the 30 - 300 μ diameter range (details depending on propellant variables). The accumulation process on the surface evidently involves sintering of individual particles together, probably concurrently with attainment of the melting point of the metal. This is followed eventually by the complete breakdown of the oxide "skin" on original particles and formation of reacting agglomorate droplets. The extent of reaction on the burning surface is unknown and probably dependent on ingredient and formulation variables. Ignition is often seen to occur concurrently with release from the surface, but with some propellants the luminous metal droplets remain for some time on the surface, and with other propellants no droplet ignition occurs untill after separation from the surface.
>
> Regardless of where ignition of aluminum occurs, most of its combustion occurs after it leaves the propellant surface, and proceeds for a considerable distance from the surface.

Certainly, if the characteristic times for the surface accumulation and the metal droplet combustion processes are the same order of magnitude as the travel time of a disturbance in the combustion chamber, then these processes represent additional sources of energy transfer which

may not be "in-phase" with the flow field disturbance. Hence, they are potential driving mechanisms of combustion instability. Since particle damping is minimal for the low frequency longitudinal chamber modes, it is likely that the exothermic metal combustion process and the interaction between velocity fluctuations and the molten layer on the burning propellant surface contribute to driving axial oscillations in the engine. Recall the experimental observation that increasing the percent of metal loading in the propellant composition often aggrevates the longitudinal combustion instability problem.

Evidence to date indicates that velocity coupling is insensitive to the direction of the velocity fluctuations in the chamber flow field [29]. Additionally, its contribution to the propellant response is non-zero only when the magnitude of the velocity disturbance exceeds a certain threshold value [2]. Thus, the coupling is distinctly non-linear. At present, no satisfactory theoretical model of this complex interaction is available. Besides the acoustic-type analyses [2,29-31] which treat the effect of velocity coupling, two computational methods have been used to describe this phenomenon: (1) a correlation expression [32] derived originally for steady erosive burning, and (2) use of the two-parameter response function [26,33] derived for pressure coupling, but modified [33,34] with a threshold velocity magnitude term. Without stronger theoretical and physical justifications, the applicability of these computational methods are open to question. Therefore, the description of the unsteady combustion response in the present study will be limited to consideration of pressure coupling only, recognizing that the results obtained for axial-mode instability in

a solid propellant rocket motor must be carefully interperted.

Previous Work in Nonlinear Instability

The observed behavior of solid rocket motors subjected to pulsing, and the fact that traveling compression wave axial instabilities can exist at shock strength [10] indicate that controlling mechanisms are definitely nonlinear. The need to account for nonlinear effects has long been recognized, but the solution to the full unsteady conservation equations presents a formidable problem. Furthermore, certain details of the combustion process are not well enough known to construct a realistic mathematical model. As a result, most theoretical analyses of solid rocket instability have been based on the linearized equations which govern the behavior of small amplitude disturbances. Then, the influence of a single nonlinear effect is studied within the framework of an acoustic chamber analysis.

Since axial-mode instabilities involve fluctuations of the gas velocity parallel to the propellant surface, the possible contribution of velocity coupling received early attention [29-31]. In Reference 29, the combustion response due to velocity coupling is assumed proportional to the magnitude of the difference between the mean flow velocity and the instantaneous velocity. This rectification effect introduces a nonlinearity proportional to the first order velocity perturbation, whereas the nonlinearity associated with the pressure is proportional to a squared perturbation. Use of a linearized analysis in the chamber is justified on this basis. The possibility of attenuation or amplification of disturbances adjacent to the burning propellant is discussed

in terms of the values of the pressure-coupled response function and a "frequency-dependent erosion constant", both of which are unknown. Price and Dehority [2] have examined a similar problem but introduced the further nonlinear effect of a threshold velocity, i.e., the combustion response is non-zero only when the stream velocity exceeds the threshold value (analogous to erosive burning). This analysis gives considerable insight into how velocity coupling should affect oscillations in the chamber, but it is not detailed enough to predict the growth of a disturbance to a limiting amplitude, etc.. Culick [33] looked at the stability of longitudinal oscillations with a combined wave equation valid in the chamber. The nonlinear velocity coupling phenomenon, described in a similar manner as in Reference (2), enters as a boundary term to the linear analysis.

An entirely different type of analysis was undertaken by Marxman [14] to explain the existence of traveling shock wave instabilities. Without combustion driving, a traveling shock wave would quickly be overtaken by expansion waves from the high pressure side. Thus, it is theorized that as the shock wave passes over the propellant, the increase in surface mass flow rate must be sufficient to keep the downstream flow sonic relative to the wave (similar to a detonation wave). Using a response function for pressure coupling, the minimum value of combustion response required to sustain the traveling shock is estimated from a local analysis. This estimate is in general agreement with the results found in the present study. However, Marxman's work does not account for mean flow effects, the nozzle loss, or transient behavior.

The first analysis to include coupled nonlinear effects without

recourse to order of magnitude estimates for eliminating various terms in the equations is due to Levine and Culick [34]. This investigation is based on a numerical solution of the full time-dependent conservation equations for a two-phase flow, and hence represents a new approach in the solution of instability problems. The quasi-one-dimensional model in Reference (34) invokes the standard assumptions of an inviscid, perfect gas and inert, mono-disperse, constant diameter, spherical particles. The solution for the chamber flow is formulated as an initial-value problem and solved with the method-of-characteristics. The chamber boundary condition at the nozzle entrance plane is derived from an isentropic relationship between the flow properties at the nozzle entrance and those at the sonic throat. The combustion response due to pressure coupling is based on the well-known two-parameter [26] response function obtained in linearized combustion analyses which assume small amplitude periodic motion in the gas phase. The desired combustion response is obtained in real time by evaluating the inverse Laplace transform of the given function of frequency. Velocity coupling is treated in an analogous manner [33]. The same response function but with different adjustable parameters and a multiplicative coefficient to account for the threshold-magnitude-effect is used to predict the response to velocity fluctuations. The total combustion response is taken as the sum of the two. However, since the two-parameter response function was derived for small amplitude periodic disturbances, its use in a combustion chamber with arbitrary amplitude transient disturbances raises the following questions:

(1) How can this model determine the transient response of the

propellant before a definite frequency of oscillation has been established in the chamber, and

(2) How can a linear model determine the combustion response to finite amplitude disturbances?

Statement of the Problem

It is the objective of this dissertation to develop a theoretical one-dimensional model for solid propellant rocket engines with a cylindrically perforated grain which can predict the time-dependent behavior of the combustion chamber and nozzle flow field after the introduction of an arbitrary disturbance. The solution will include the unsteady flow in the choked nozzle, eliminating the need for an artificial nozzle boundary condition. The combustion of the solid propellant will be described by a time-dependent solution obtained simultaneously with the chamber flow field. No restrictions will be placed on the amplitude or type of disturbance in the engine. Shock waves resulting from combustion driving or as an initial disturbance simulating the experimental pulsing technique, will be acceptable solutions to the theoretical model.

In what follows, Chapter II describes the development of the solutions to the nonlinear time-dependent conservation equations for a two-phase flow in the combustion chamber and nozzle. Chapter III describes the analysis and solution of the time-dependent solid propellant combustion process which will be used to predict the combustion response to arbitrary disturbances in the chamber. Chapter IV discusses the results obtained for the transient response of the engine after

introduction of various types of disturbances. Chapter V summarizes the results obtained in this investigation.

CHAPTER II

ANALYSIS OF THE COMBUSTION CHAMBER AND NOZZLE FLOW FIELD

Discussion of Assumptions

Solid propellant rocket motors exhibiting axial mode instability are usually characterized by a ratio of chamber length to chamber radius much greater than unity. Considering the high turbulence level present, radial property variations are sufficiently small that a one-dimensional formulation provides an adequate description of the flow field. To avoid placing restrictions on the type of transient behavior which may be encountered in the rocket motor, the present investigation will consider,

(a) the full non-linear, time-dependent conservation equations

(b) the flow in the choked nozzle

(c) the transient behavior of the combustion process coupled to the chamber flow field (see Chapter III).

The first requirement means that the analysis must be capable of handling traveling shock waves, if they appear in the flow field.

With these requirements, consider an axisymmetric, one-dimensional combustion chamber and nozzle system with a cylindrically perforated solid propellant grain (see Figure 2). The solid propellant is assumed to be the metal loaded type (typically, aluminum) which deposits solid particles (eg., Al_2O_3) in the flow when combustion is completed. Hence,

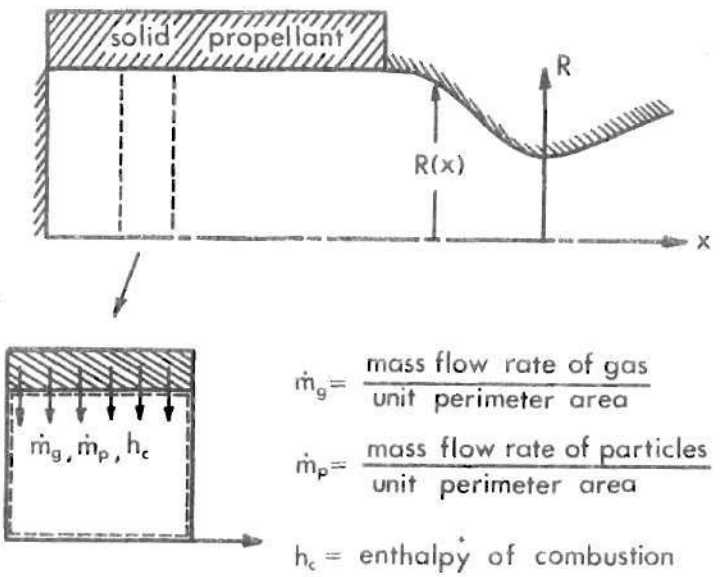

Figure 2. Solid Propellant Rocket Engine Model

the flow in the combustion chamber and nozzle is two phase. The present analysis is based on several standard assumptions:

(1) The gas medium is thermally and calorically perfect. Implied in this statement is the assumption that all combustion is complete when the gases have left the flame zone and entered the combustor control volume.

(2) The gas medium is inviscid and non-heat-conducting. However, the gas-particle interaction can involve the exchange of momentum and energy. The heat transfer process at the burning propellant surface located outside the combustor control volume perimeter boundary is dealt with separately in Chapter III.

(3) The solid particles suspended in the gas have negligible volume and exert no pressure.

(4) The actual distribution of particle sizes can be replaced with a system of non-reacting spherical particles having one average diameter constant in time. As Price [28] has emphasized, the solid particles are not produced directly in the flame zone. Since the ignition temperature is much higher than the melting point temperature for metals, a liquid layer forms on the propellant surface. Complicated condensed phase reactions occur between the gas and large agglomerates of molten metal from the surface. These reactions may take place well outside of the flame as the metal droplets are entrained in the gas flow. When combustion is complete, solid oxide particles remain suspended in the gas. In general, the resultant distribution of particle diameters is bimodol; that is, particles in the 0 - 2μ (smoke) range and the larger 5 - 20μ range. The approximate nature of assumption (4) is fully recognized, but further modeling of this complex process is beyond the scope of the present analysis.

(5) The drag force between solid particles and gas can be represented by a simple drag law as a function of Reynolds number. In view of the discussion of assumption (4), use of a drag law for spherical, non-reacting particles in the present problem is also open to question. However, the well-known Stokes Flow Drag Law is employed in this study,

recognizing that the upper Reynolds number limit may be violated in certain instances. The available higher order corrections [34,35] could easily be introduced in future work.

(6) The time rate of change of thermal energy stored by the particles is negligible compared to the time rate of change of kinetic energy. Thus, particles are assumed to leave the nozzle with whatever thermal energy they acquired in the flame zone, which is valid for a vanishingly small heat transfer coefficient. Reference (34) has not made this assumption and has included the energy transfer between gas and particles. It appears, however, that this effect is small and its treatment could be delayed until a more sophisticated combustion analysis is attempted.

(7) The mass flow rates of gas and particles from the burning propellant surface enter the perimeter boundary of the combustor control volume with negligible velocity. Thus, the mass addition at the perimeter boundary contributes zero axial momentum and zero kinetic energy to the control volume. Part of the energy in the control volume must be used to accelerate the entering mass flows of gas and particles to their respective local velocities. This results in an additional drag term in the momentum equations and a dissipation term in the energy equation, which approximates the effect of a wall boundary layer.

(8) The increase of chamber volume due to regression of the

propellant surface is assumed negligible. For a linear regression rate of one cm/sec and an initial chamber radius of one foot, the volume change after one second is about six percent. Since wave travel times are on the order of milliseconds, this effect can be ignored. The exception might be ignition transient phenomena if several seconds are involved.

The one-dimensional assumption needs further comment. The control volume shown in Figure 2 illustrates the inherent difficulty with a one-dimensional analysis as applied to this problem. The mass flow of gas and particles leaving the propellant surface enters perpendicular to the axial direction. In the present analysis, the integral of the mass flow rate over the perimeter boundary of the control volume becomes a mass source within the control volume. However, the exact process by which the mass flows of gas and particles are accelerated to their respective axial velocities within the control volume is obscured by the integral approach. Although the process is left unspecified, its effect is accounted for in the analysis. Levine and Culick [34] employ the same approximation. This avoids a difficult two-dimensional analytical problem but the higher order formulation will eventually be required to model the details of the interaction of the "core" flow with the combustion process at the boundary.

Method of Solution

With the assumptions of the previous section, the time-dependent convervation equations applied to the present problem lead to a hyper-

bolic initial-value problem. Solutions to this system of equations can include traveling discontinuities. When developing a method of solution, an important consideration is the accurate tracking of these discontinuities.

In computational fluid mechanics, two basic methods of employing the conservation equations have been advanced. One widely-used technique [36-38], referred to as the finite-element method or conservative form, is one in which mass, momentum and energy are conserved strictly for a finite-size control volume. An advantage [36] of this method is attributed to a cancellation of numerical error on interior boundaries when elements are summed over a finite domain. Since this formulation reduces to the proper jump conditions as the computational element shrinks to zero thickness, it has been claimed [38] that discontinuous behavior can be computed without special computational procedures. Using MacCormack's [39] predictor-corrector integration scheme, Kutler and Lomax [38] have computed steady flow fields (which include shock waves) over various blunt body and wing configurations. Their method is said to be "shock capturing", i.e., shock waves are smeared over three or more mesh points but automatically forced to the proper location. A second method is to solve the conservation equations in partial differential form with a finite difference technique. Then the information contained in the associated characteristic equations can be used to track discontinuities precisely. Moretti [40] has used this method for shock tube problems with multiple shock waves and contact discontinuities.

In Reference (41), the familiar problem of a piston accelerating

into a stagnate gas is used to compare the predictions of many well-known numerical integration schemes, employing both the conservative and finite difference form of the conservation equations. For the time period before shock wave formation, second-order integration schemes with the conservative form of the equations demonstrate no more accuracy than with the finite difference form. All methods yield acceptable results. However, if the computation is continued beyond the formation of the shock wave, numerical wiggles appear in the flow field with all schemes. A numerical wiggle is defined here as a "saw-tooth" oscillation (high, low, high, low, . . .) of the magnitude of a flow field variable from one mesh point to the next. Doubling the number of mesh points usually doubles the number of wiggles since no physical process is represented. Although MacCormack's [39] scheme with the conservative form of the equations (i.e., the shock capturing method) exhibits the minimum amount of this behavior, pronounced wiggles are evident on the low pressure side of the shock wave [40] even with 360 mesh points between the piston and the undisturbed portion of the gas. By contrast, Moretti [40] solved the same problem with 20 mesh points using the finite difference form of a second-order Taylor series expansion of the conservation equations and supplementary information from the method-of-characteristics, and predicted the behavior of the discrete shock wave with no wiggles. It is concluded that integrating continuous differential equations across a discontinuity will produce wiggles.

The properties demonstrated by Moretti's computational scheme are required in the present transient analysis where the location of

a shock wave in the rocket engine flow field is important in determining the instantaneous combustion response. Consequently, Moretti's [41,42] technique is adopted in this study. The method is based on three important postulates which are paraphrazed here:

(1) If a region of continuous flow is defined by continuity of second derivatives, then all integration schemes of second-order accuracy will predict acceptable results in a continuous region. Under these conditions, the conservative form of the conservation equations is no more accurate than the finite difference form.

(2) Treat discontinuities as discontinuities; i.e., do not integrate continuous differential equations across steep-fronted waves.

(3) Do not violate the conservation equations when evaluating flow field variables on a boundary.

These principles will be implemented in the present numerical integration scheme which will be outlined in the next two sections. In a brief summary, the conservation equations will be written for a general stream-tube control volume and then reduced to partial differential form by shrinking the control volume thickness to zero. These equations will then be transformed to a floating computational coordinate system which treats discontinuities as moving internal boundaries. For this formulation, a hybrid integration scheme arises naturally. All regions of continuous flow between two boundaries will be integrated forward in time with a second-order Taylor series expansion of the differential equations. Values of flow field variables on all boundaries as well as the movement of the internal boundaries will be obtained with the supplemental information from the method of characteristics.

All necessary equations are derived in the two sections which follow.

By way of comparison, the instability analysis of Levine and Culick [34] uses the method-of-characteristics to obtain the entire solution. Thus, the numerical accuracy of the present analysis should be equal to that of Reference (34). However, in a flow field with traveling regions of compression and expansion, the natural characteristic mesh system becomes very irregular and can require a lot of time-consuming interpolation. This is avoided with Moretti's method.

Derivation of Equations

Based on the assumptions discussed in the first section, the conservation of mass, momentum and energy for the general control volume shown in Figure 2 can be written as follows:

Conservation of Mass (gas phase)

$$\frac{\partial}{\partial t}\int_{c.v.}\int\int\rho dV + \int_{c.s.}\int\int \rho\vec{u}\cdot d\vec{A} = \int_{c.s.p.}\int\int \dot{m}_g dA_p \qquad (2.1)$$

Conservation of Mass (solid particles)

$$\frac{\partial}{\partial t}\int_{c.v.}\int\int\rho_p dV + \int_{c.s.}\int\int \rho_p\vec{u}_p\cdot d\vec{A} = \int_{c.s.p.}\int\int \dot{m}_p dA_p \qquad (2.2)$$

Conservation of Momentum (gas phase and solid particles)

$$\frac{\partial}{\partial t}\int_{c.v.}\int\int\int (\rho u + \rho_p u_p)\, dV + \int_{c.s.}\int\int (\rho u\vec{u} + \rho_p u_p \vec{u}_p)\cdot d\vec{A} = \sum \vec{F} \quad (2.3)$$

Conservation of Momentum (solid particles alone)

$$\frac{\partial}{\partial t}\int_{c.v.}\int\int\int \rho_p u_p\, dV + \int_{c.s.}\int\int \rho_p u_p \vec{u}_p \cdot d\vec{A}_p = \int_{c.v.}\int\int\int K\rho_p(u-u_p)\, dV \quad (2.4)$$

Conservation of Energy (gas phase and solid particles)

$$\frac{\partial}{\partial t}\int_{c.v.}\int\int\int \left\{\rho\left[\frac{e}{\gamma(\gamma-1)} + \frac{u^2}{2}\right] + \rho_p \frac{u_p^2}{2}\right\} dV$$

$$+ \int_{c.s.}\int\int \left\{\rho\left[\frac{h}{\gamma-1} + \frac{u^2}{2}\right]\vec{u} + \rho_p \frac{u_p^2}{2}\vec{u}_p\right\}\cdot d\vec{A}$$

$$= \int_{c.s.p.}\int\int \frac{h_c}{\gamma-1}\dot{m}_g\, dA_p \quad (2.5)$$

Equation of State (gas phase)

$$p = \rho e = \rho h \tag{2.6}$$

where all variables have been non-dimensionalized with respect to the following reference state,

$$p_r^* = \rho_r^* R_{gas} T_r^*$$

$$a_r^{*2} = \gamma R_{gas} T_r^*$$

$$T_r^* = h_r^*/c_p = e_r^*/c_v \tag{2.7}$$

and the area A^*_{ch} and length L^*. The right-hand side of Equation (2.3) represents the reaction of the surroundings on the control surface due to internal pressure forces. The right-hand side of Equation (2.4) represents the volumetric drag due to the presence of solid particles traveling with velocity u_p. The parameter K,

$$K \equiv \frac{9}{2} \frac{\mu^*}{\hat{\rho}^*_m \sigma^{*2}} \cdot \left(\frac{L^*}{a_r^*} \right) \tag{2.8}$$

results from the application of the Stokes Flow Drag Law.

By shrinking the control volume to zero size, Equations (2.1) through (2.5) can be written in the partial differential form needed for a Taylor series expansion. After some manipulation, these equations become,

Conservation of Mass (gas phase)

$$\frac{\partial \rho}{\partial t} + \rho \frac{\partial u}{\partial x} + u \frac{\partial \rho}{\partial x} = R_1 \equiv \frac{2\dot{m}_g}{\bar{R}} - \rho u \frac{d\ln A}{dx} \qquad (2.9)$$

Conservation of Mass (solid particles)

$$\frac{\partial \rho_p}{\partial t} + \rho_p \frac{\partial u_p}{\partial x} + u_p \frac{\partial \rho_p}{\partial x} = R_2 \equiv \frac{2\dot{m}_p}{\bar{R}} - \rho_p u_p \frac{d\ln A}{dx} \qquad (2.10)$$

Conservation of Momentum (gas phase)

$$\frac{\partial u}{\partial t} + u \frac{\partial u}{\partial x} + \frac{1}{\gamma \rho} \frac{\partial p}{\partial x} = R_3 \equiv - \left\{ K \rho_p (u - u_p) + \frac{2}{\bar{R}} \dot{m}_g u \right\} / \rho \qquad (2.11)$$

Conservation of Momentum (solid particles)

$$\frac{\partial u_p}{\partial t} + u_p \frac{\partial u_p}{\partial x} = R_5 \equiv K(u-u_p) - \frac{2}{R} \frac{\dot{m}_p u_p}{\rho_p} \tag{2.12}$$

Conservation of Energy (gas phase)

$$\frac{\partial S}{\partial t} + u \frac{\partial S}{\partial x} = R_4 \equiv \frac{\gamma(\gamma-1)}{p} \left\{ \frac{2}{R} \left[\dot{m}_g \left(\frac{h_c - h}{\gamma - 1} \right) \right. \right.$$

$$\left. \left. + \frac{1}{2} (\dot{m}_g u^2 + \dot{m}_p u_p^2) \right] + K \rho_p (u-u_p)^2 \right\} \tag{2.13}$$

where

$$h = p/\rho$$

and

$$S \equiv \ln p - \gamma \ln \rho \tag{2.14}$$

In Equation (2.14), the reference state is assigned a zero entropy value.

These equations are employed in a computational coordinate system which contains two fixed boundaries (the head end of the combustion chamber, and the nozzle supersonic exit plane) and any number (which may be zero) of internal moving boundaries as shown in Figure 3. A

shock wave discontinuity is treated as a moving boundary, and the flow field in a region between any two boundaries is assumed continuous. In the general case, the two boundaries of a flow field region may move independently of each other. To avoid having to compute the movement of a boundary over a system of fixed mesh points and to simplify the calculation procedure, the independent variables are normalized for one region. These computational coordinates will then "float" with the movement of the boundaries. Consider the following transformation:

(1) First, let $\xi = \xi(x)$ be a stretching function which allows equally spaced grid points in ξ to represent a non-uniform distribution in x. With the proper weighting, this function permits a minimum total number of mesh points to accurately represent regions where flow field properties are changing rapidly (e.g., near the choked throat).

(2) Then, in ξ-space, let the instantaneous location of the right hand boundary be given by $c(t)$, and the left hand boundary by $b(t)$. For a typical region of continuous flow, define

$$X \equiv \frac{\xi(x) - b(t)}{c(t) - b(t)}$$

$$T \equiv t \tag{2.15}$$

where $X = 0$ and $X = 1$ locate the left and right hand boundaries respectively (see Figure 3).

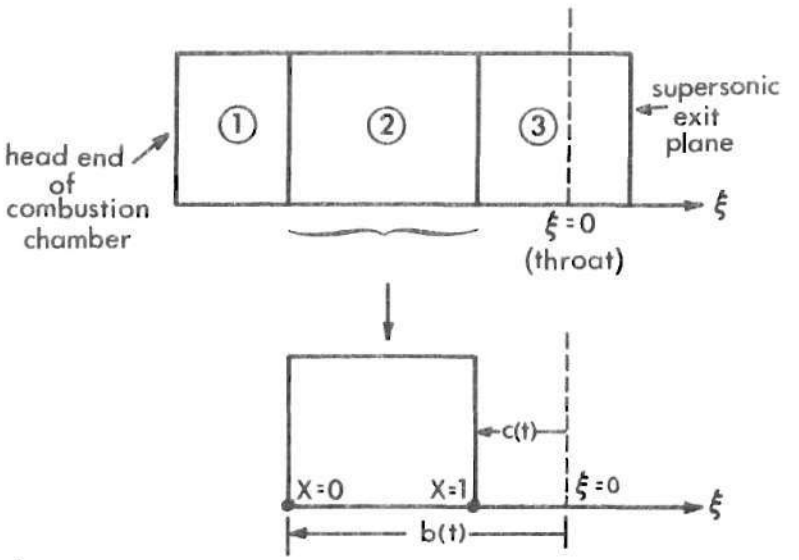

Figure 3. Computational Coordinate System

The partial derivatives transform as

$$\frac{\partial}{\partial x} = \eta \frac{\partial}{\partial X} \tag{2.16}$$

$$\frac{\partial}{\partial t} = \frac{\partial}{\partial T} + \frac{\beta}{c-b} \frac{\partial}{\partial X}$$

where

$$\eta \equiv \frac{d\xi/dx}{c-b}$$

$$\beta \equiv (X-1)\frac{d}{dt}\,b(t) - X\frac{d}{dt}\,c(t)$$

By letting,

$$U \equiv \eta u + \frac{\beta}{(c-b)} \tag{2.17}$$

$$U_p \equiv \eta u_p + \frac{\beta}{(c-b)} \tag{2.18}$$

then Equations (2.9) through (2.13) transform to,

$$\frac{\partial \rho}{\partial T} + U\frac{\partial \rho}{\partial X} + \eta\rho\frac{\partial u}{\partial X} = R_1 \tag{2.19}$$

$$\frac{\partial \rho_p}{\partial T} + U_p\frac{\partial \rho_p}{\partial X} + \eta\rho_p\frac{\partial u_p}{\partial X} = R_2 \tag{2.20}$$

$$\frac{\partial u}{\partial T} + U\frac{\partial u}{\partial X} + \frac{\eta}{\gamma\rho}\frac{\partial p}{\partial X} = R_3 \tag{2.21}$$

$$\frac{\partial u_p}{\partial T} + U_p\frac{\partial u_p}{\partial X} = R_5 \tag{2.22}$$

$$\frac{\partial S}{\partial T} + U \frac{\partial S}{\partial X} = R_4 \tag{2.23}$$

In the special case when all internal boundaries are absent, $c - b = 1$, and the stretching function is linear, $\eta = d\xi/dx = 1$, then $U = u$, $U_p = u_p$ (since $dc/dt = db/dt = 0$ for the stationary boundaries) and the above set of equations reduces to the original form, Equation (2.9) through Equation (2.13).

Forward time integration of Equations (2.19) through (2.23) in a continuous region is accomplished with a finite-difference approximation to a Taylor series expansion, truncated after the second-order terms. This insures an accurate representation of the non-homogeneous parts of the equations. It is not clear that a straight-forward application of well-known schemes such as MacCormack's [39] or the two-step Lax-Wendroff [43] would provide the proper accuracy for these non-homogeneous terms. The Taylor series expansion for the dependent variables at time $T = T_o + \Delta T$ (denoted by subscript 1) in terms of the known information at T_o (denoted by subscript o) is

$$\rho_1 = \rho_o + \rho_T|_o \Delta T + \rho_{TT}|_o \frac{\Delta T^2}{2} \tag{2.24}$$

$$\rho_{p_1} = \rho_{p_o} + \rho_{p_T}|_o \Delta T + \rho_{p_{TT}}|_o \frac{\Delta T^2}{2} \tag{2.25}$$

$$u_1 = u_o + u_T|_o \Delta T + u_{TT}|_o \frac{\Delta T^2}{2} \tag{2.26}$$

$$u_{p_1} = u_{p_o} + u_{p_T}|_o \Delta T + u_{p_{TT}}|_o \frac{\Delta T^2}{2} \tag{2.27}$$

$$S_1 = S_o + S_T|_o \Delta T + S_{TT}|_o \frac{\Delta T^2}{2} \tag{2.28}$$

The first-order time derivatives follow directly from Equations (2.19) through (2.23) with a centered differencing method for spatial derivatives. Thus for the mesh system,

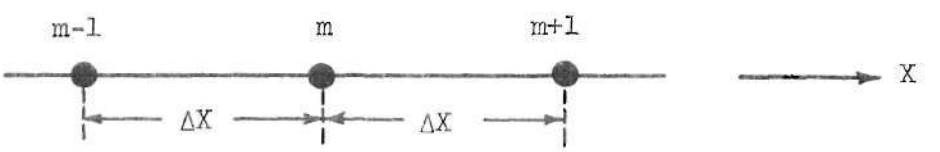

Equation (2.19) at point "m" becomes

$$\rho_T|_o = R_{1_m} - U_m \left[\frac{\rho_{m+1} - \rho_{m-1}}{2\Delta X} \right] - \eta_m \rho_m \left[\frac{u_{m+1} - u_{m-1}}{2\Delta X} \right] \tag{2.29}$$

The second order time derivatives are obtained from Equation (2.19) through (2.23) by an additional time differentiation. From Equation (2.19) it follows that

$$\rho_{TT}\Big|_o = R_{1_T} - \left\{U_T\rho_X + U\rho_{TX} + \eta(\rho_T u_X + \rho u_{TX}) \right.$$

$$\left. + \eta_T \rho u_X \right\} \qquad (2.30)$$

where a term like u_{TX} can be evaluated from Equation (2.21) as

$$(u_T)_X = R_{3_X} - \left\{U_X u_X + U u_{XX} + \frac{\eta}{\gamma\rho}\left[p_{XX} - p_X\rho_X/\rho\right]\right\} \qquad (2.31)$$

Second order spatial derivatives, such as u_{XX}, are simply

$$u_{XX} = \frac{u_{m+1} + u_{m-1} - 2u_m}{\Delta X^2} \qquad (2.32)$$

By continuing this development, the right-hand sides of Equations (2.24) through (2.28) can be expressed entirely in terms of the known solution at time T_o. Given the proper ΔT, these equations determine the new flow field variables at time $T_o + \Delta T$ for all interior mesh points, as shown in Figure 4.

However, the Taylor series expansion does not yield values of flow field variables on a boundary. Determining these boundary values is the subject of the next section.

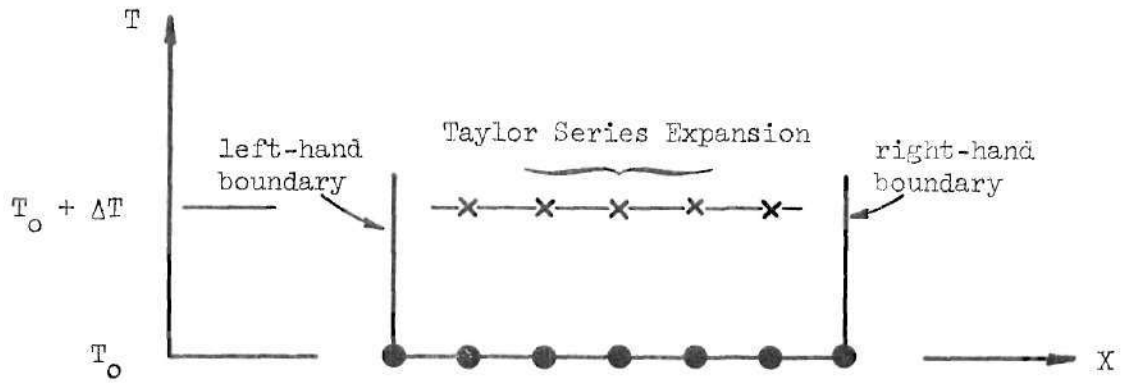

Figure 4. Region of Applicability of Taylor Series Integration

Boundary Conditions and Shock Waves

The information contained in the system of Equations (2.19) through (2.23) when written in characteristic form will be used to track the moving boundaries and establish values of flow field variables on fixed boundaries. If the pressure gradient term in Equation (2.21) is replaced by

$$\frac{\partial p}{\partial X} = p\left[\frac{\partial S}{\partial X} + \frac{\gamma}{\rho}\frac{\partial \rho}{\partial X}\right] \tag{2.33}$$

then the system becomes five equations in the five dependent variables ρ, ρ_p, u, u_p and S. The five characteristic directions in the transformed coordinate system are found to be,

$$\frac{dX}{dT} = \begin{cases} U \\ U + \eta a \\ U - \eta a \\ U_p \text{ (double root)} \end{cases} \tag{2.34}$$

where $a^2 = p/\rho$. If the equation describing energy transfer between gas and particles had been included in the system, then U_p would become a triple root. The general compatibility relation is given by,

$$\left(\frac{dX}{dT} - U_p \right)^2 \left\{ \left(\frac{dX}{dT} - U \right)^2 \left(\frac{d\rho}{dT} - R_1 \right) + \left(\frac{dX}{dT} - U \right) \left(\frac{du}{dT} \right.\right.$$

$$\left.\left. - R_3 \right) \eta\rho + \frac{\rho a^2 \eta^2}{\gamma} \left(\frac{dS}{dT} - R_4 \right) \right\} = 0 \tag{2.35}$$

For the individual roots, Equation (2.35) yields:

(a) along $\frac{dX}{dT} = U$ (gas path stream line)

$$dS = R_4 \, dT \tag{2.36}$$

which is the energy equation.

(b) along $\frac{dX}{dT} = U \pm \eta a$ (left and right-running characteristics)

$$\left(\frac{a}{\gamma p} \right) dp \pm du = \left\{ \pm R_3 + a \left(\frac{R_1}{\rho} + \frac{R_4}{\gamma} \right) \right\} dT \qquad (2.37)$$

For the special case of no heat or mass addition from combustion, single phase flow, and stationary coordinates, Equations (2.36) and (2.37) reduce to the familar gas dynamic relations,

$$dS = 0 \quad \text{along} \quad \frac{dx}{dt} = u$$

$$\left(\frac{dp}{p} \right) \pm \gamma \left(\frac{du}{a} \right) = 0 \quad \text{along} \quad \frac{dx}{dt} = u \pm a \qquad (2.38)$$

A peculiar difficulty arises along the characteristic direction $dX/dT = U_p$ (double root). The general compatibility relation (i.e., Equation 2.35) yields only the trivial result, $0 = 0$. Normally, this indicates that two equations in the system are already in characteristic form. This is true for the particle momentum equation (i.e., Equation 2.22) which can be written as,

$$\frac{\partial u_p}{\partial T} + U_p \frac{\partial u_p}{\partial X} = \frac{du_p}{dT} = R_5 \qquad (2.39)$$

along $dX/dT = U_p$. However, the particle continuity equation (i.e., Equation 2.20) cannot be written in characteristic form. The contradiciton can be traced to the lack of an equation of state for the solid particle flow. With no mechanism relating particle density to pressure, and hence no particle speed of sound, the particle momentum equation is not coupled to the particle continuity equation. The present analysis will interpret this to mean that Equation (2.20) in the form,

$$\frac{d\rho_p}{dT} = R_2 - \eta\rho_p \frac{\partial u_p}{\partial X} \tag{2.40}$$

can be integrated along $dX/dT = U_p$ after an integration of Equation (2.39). The results from Equation (2.39) can be used to estimate an average value of $\partial u_p/\partial X$. Reference (34) handled this problem in a similar manner.

In the X-T computational space of the previous section, the flow field representing the combustion chamber and nozzle has two stationary boundaries and any number of internal moving boundaries. As an illustration, consider a flow field with one right running shock wave (Figure 5). The head end of the combustion chamber is $X = 0$ in region [1], the right-running shock wave is the boundary between [1] and [2], and the exit plane of the nozzle is $X = 1$ in region [2].

Two boundary conditions are known at the head end of the combustion chamber, namely

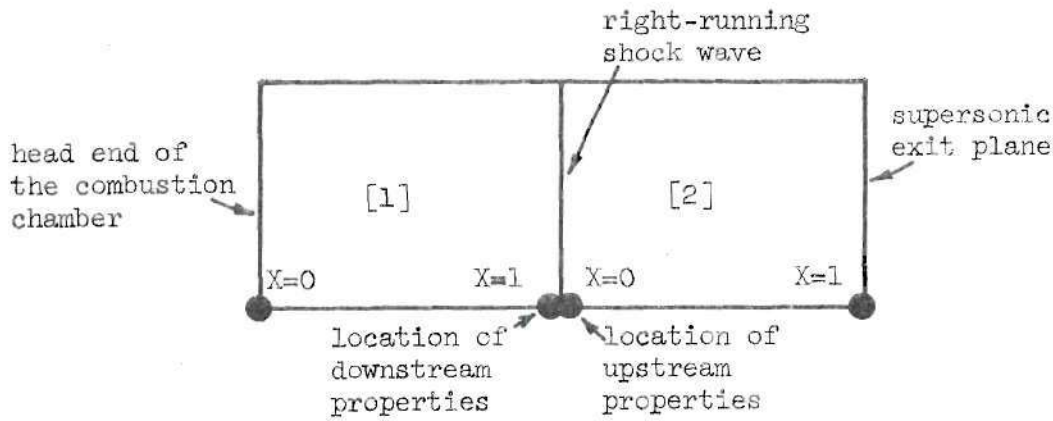

Figure 5. Computational Coordinates for Example Problem With One Right-Running Shock Wave

$$u|_{X=0}^{[1]} = u_p|_{X=0}^{[1]} = 0 \qquad (2.41)$$

However, the numerical computation also requires values of ρ, ρ_p, and S at this location at every time step. These are determined with the method-of-characteristics. From the T - X diagram shown in Figure 6,

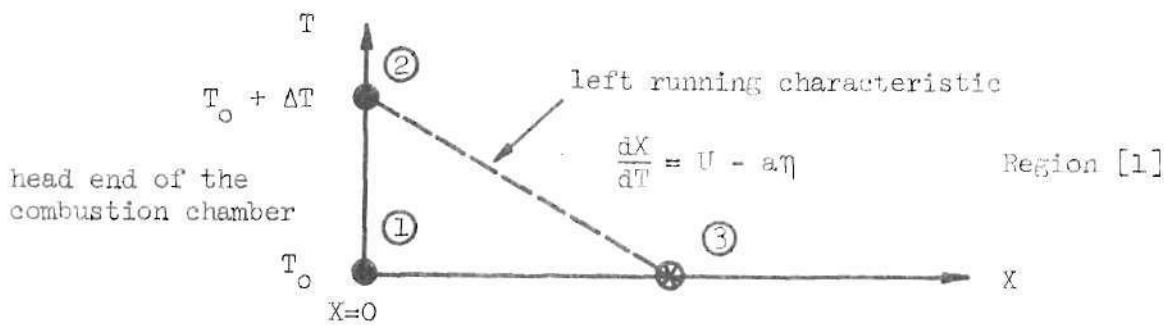

Figure 6. Method Used to Compute Boundary Values at Head End of Combustion Chamber

it can be seen that the left-running characteristic reaches the new wall point ② from some location along the known datum plane $T = T_o$. The compatibility relation (i.e., Equation 2.37) along this characteristic line can be written as follows

$$\left(\frac{a}{\gamma p} \right)_{ave} (p_2 - p_3) + u_3 = \left\{ - R_3 + a \left(\frac{R_1}{\rho} + \frac{R_4}{\gamma} \right) \right\}_{ave} \Delta T \quad (2.42)$$

where p at ② is unknown. The line ① - ② is a stream line for both gas and particle flows. Thus from Equation (2.36)

$$S_2 - S_1 = R_4 \big|_{ave} \Delta T \quad (2.43)$$

and from Equation (2.40)

$$(\rho_{p_2} - \rho_{p_1}) = \left(R_2 - \eta \rho_p \frac{\partial u_p}{\partial X} \right)_{ave} \Delta T \quad (2.44)$$

These equations along with the definition of entropy determine ρ, ρ_p and S at point ②. In practice, an iteration process involving an average speed of sound between ② and ③ is required to accurately locate the point ③. Normally, this iteration converges in about three cycles.

The second stationary boundary of the problem is the supersonic exit plane of the nozzle located at X = 1 in region [2]. In single phase flow (gas only), a common procedure is to linearly extrapolate all variables from the two adjacent upstream mesh points assuming they are in supersonic flow. Errors introduced by this extrapolation never influence the upstream calculations since the flow velocity exceeds the local speed of propagation of a disturbance. This method yields acceptable results in the present analysis when the particle flow is deleted. With the particle flow included, however, the small errors in u_p and ρ_p at the boundary do propagate upstream and eventually destroy the solution. A speed of propagation characteristic of the suspended particles alone has not been defined. Since the speed of sound in a gas-particle mixture is less than its value in the gas alone, attempts to explain this behavior on the basis of an effective speed of propagation have not been successful. The current analysis avoids this difficulty with a complete method of characteristics solution at the exit plane for all five flow field variables. This is illustrated on a T - X diagram in Figure 7 for the example of Figure 5. The compatibility relations along these directions are written in a form similar to Equations (2.42) through (2.44) and a standard iteration technique is used to locate the intersection points ③, ④, ⑤ and ⓪. This solution at the supersonic boundary eliminates the upstream error propagation observed with the extrapolation technique.

The properties upstream and downstream of a traveling shock wave are determined at the next time step in an analogous manner. For the right-running shock wave in Figure 5, upstream properties are located

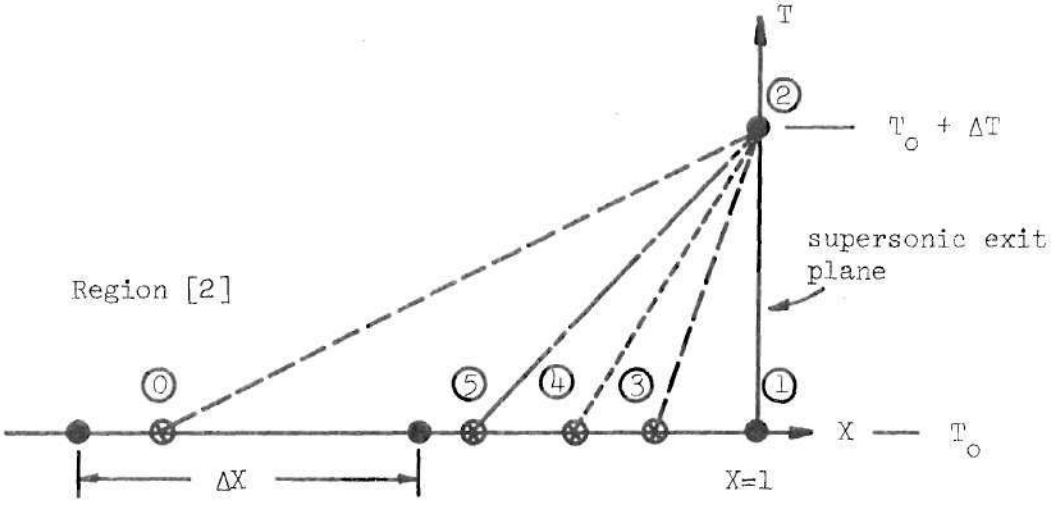

Line ⓪ - ② right running characteristic $\frac{dX}{dT} = U + a\eta$

③ - ② left running characteristic $\frac{dX}{dT} = U - a\eta$

④ - ② particle path streamline $\frac{dX}{dT} = U_p$

⑤ - ② gas path streamline $\frac{dX}{dT} = U$

Figure 7. Method of Characteristics Solution to Obtain Boundary Values at Supersonic Exit Plane

at X = 0 in region [2] and downstream properties are at X = 1 in region [1]. These two points are treated separately in the computational method, but they represent the same point in physical space. The

integration procedure is shown in the physical t - x plane by Figure 8.

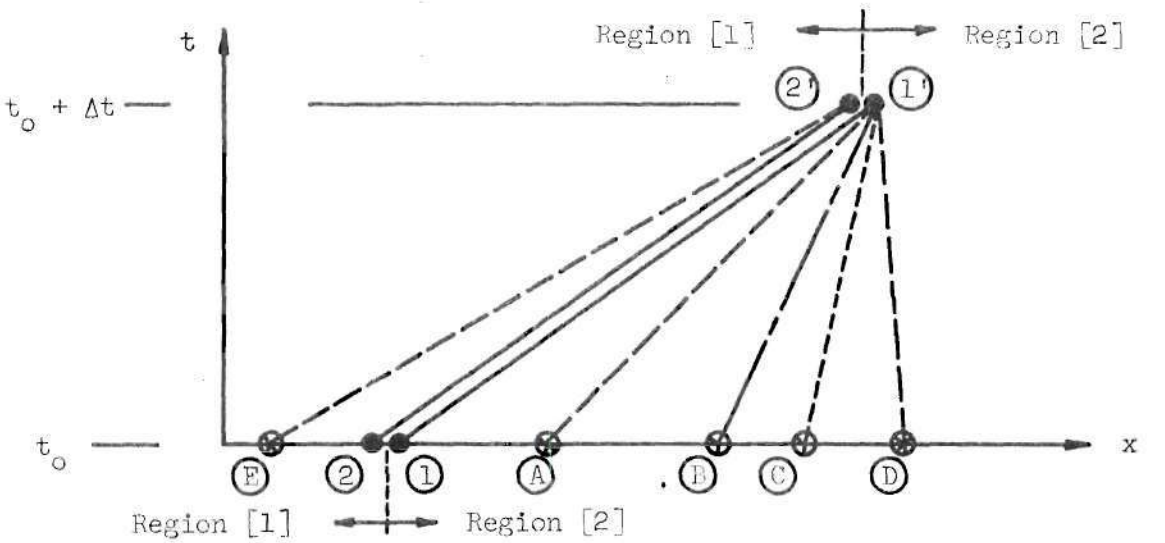

Line (E) - (2') and (A) - (1') : right running characteristic $\frac{dx}{dt} = u + a$

(D) - (1') : left running characteristic $\frac{dx}{dt} = u - a$

(B) - (1') : gas path streamline $\frac{dx}{dt} = u$

(C) - (1') : particle path streamline $\frac{dx}{dt} = u_p$

shock wave path

Figure 8. Method Used to Compute Shock Wave Propagation

The shock wave velocity at time $t = t_o$ is integrated with respect to time to give the new location (1') (same as (2')). In agreement with intuition, the method to predict the upstream properties at this new location is based only on information ahead of the wave. This is accomplished with a complete method of characteristics solution in the triangular region (A) - (D) - (1') . The routine is the same one used to obtain the supersonic boundary condition. Since the suspended solid particles exert no pressure, they are not influenced by the discontinuous jump through the shock wave. Hence values of ρ_p and u_p determined in the upstream property solution at (1') are assigned to (2') . Of course, the particle flow is involved in a relaxation process downstream of the wave. Three gas properties (ρ, u, S) at the downstream location of the shock wave, (2') , and the new shock wave velocity, w_s, remain to be determined. Three of the necessary equations come from the Rankine-Hugoniot relations which conserve mass, momentum and energy across the discontinuity. In a stationary coordinate system where subscripts 1 and 2 indicate upstream and downstream respectively, these equations are

$$\rho_2 u_2 - w_s(\rho_2 - \rho_1) = \rho_1 u_1 \tag{2.45}$$

$$h_2\rho_2/\gamma + \rho_1 u_1(u_2 + w_s) - \rho_1 u_2 w_s = p_1/\gamma + \rho_1 u_1^2 \tag{2.46}$$

$$\frac{h_2}{\gamma-1} + \frac{u_2^2}{2} + w_s(u_1 - u_2) = \frac{h_1}{\gamma-1} + \frac{u_1^2}{2} \qquad (2.47)$$

The shock wave velocity w_s relative to the fixed coordinate system is positive for a right-running wave. The fourth equation is the compatibility relation along the trailing subsonic characteristic which reaches the shock from the high pressure side. In the present example, this is the right-running characteristic (E) - (2'). The solution to this system of four simultaneous equations is obtained with a minimization scheme due to Davidon [44,45]. The values of ρ, ρ_p, u, u_p and S determined on the downstream side of the shock wave are assigned to the variables at X = 1 in region [1] and the upstream values are assigned at X = 0 in region [2]. Thus, all boundary conditions are obtained in a manner consistent with the conservation equations and no continuous differential equation is integrated across a discontinuity.

It is anticipated that, under certain conditions, continuous disturbances in the rocket engine flow field could steepen and eventually form shock waves. Hence, use of the above computational method is contingent upon recognizing the formation of an embedded shock wave in a region of continuous flow. Any attempt to equate an infinite pressure gradient (indicating the presence of a shock wave) with a large number computed from finite-difference values is arbitrary at best. Hence, a more sensitive method is required to predict the onset of the discontinuity. Figure 9 illustrates a typical situation in the numerical

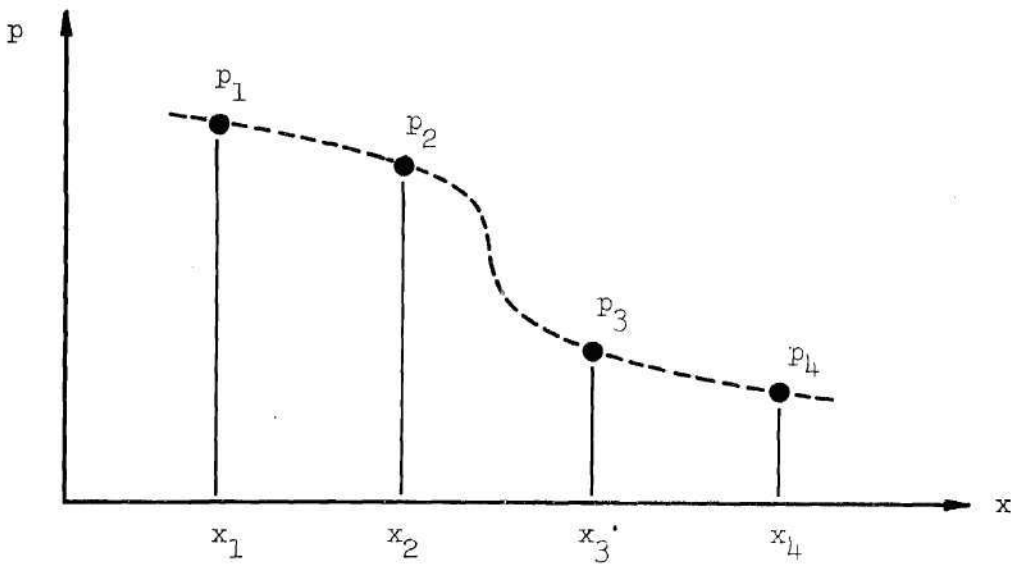

Figure 9. Pressure Waveform During Steepening of a Compression Wave in the Numerical Flow Field

flow field when a compression wave is steepening. Following Moretti's work [42], a third-order polynomial fitted to the values at four mesh points is assumed to represent the pressure distribution in this interval. If this polynomial predicts an infinite gradient, its location is taken as the origin of the discontinuity. Numerically, this is done in the following manner. Given the two functions, $p = F(x)$ and $x = G(p)$ in the interval $x_1 \leq x \leq x_4$, the location at which $dF/dx \rightarrow \infty$ is also defined by $dG/dp = 0$. Thus the polynomial,

$$x = G(p) = Ap^3 + Bp^2 + Cp + D \qquad (2.48)$$

is specified by the constants A, B, C, D determined by the given values at the mesh points, (p_i, x_i) $i = 1 \ldots 4$. The zero derivative must satisfy

$$\frac{dx}{dp} = 0 = \frac{dG}{dp} = 3Ap^2 + 2Bp + C \tag{2.49}$$

Real roots of Equation (2.49) are possible only for non-negative values of the discriminant $\tilde{D}$, where

$$\tilde{D} = B^2 - 3AC \tag{2.50}$$

In the present problem, $\tilde{D}$ maintains a negative value for continuous pressure distributions which do not steepen. This provides an easy check for the steepening of compression waves. At each time step, a computer search routine checks for a non-negative value of $\tilde{D}$ for all combinations of four adjacent mesh points in the continuous regions; if one is found, the x location of the roots of Equation (2.49) are calculated with Equation (2.48). If a root lies within the interval $x_1 \leq x \leq x_4$, an interior boundary is inserted at this location and the computation proceeds tracking a Mach wave as a discontinuity. Hence, as the compression wave continues to steepen, it is treated as a shock wave.

It might be argued that this "sensing" method is heavily

dependent on how well the third-order polynomial represents the actual pressure distribution. In spite of its potential short-comings, the technique has proved quite sensitive to discontinuity formation in the present investigation. Even if the formation is predicted prematurely, there are no penalties associated with tracking a Mach wave as a discontinuity. On the other hand, the author can verify that severe penalties are incurred for late recognition of discontinuous behavior.

Integration of the equations in the floating computational coordinate system with moving internal boundaries requires many decisions of a practical nature. Typical of these is how a shock wave passes through the exit plane of the nozzle. As the right-running shock wave in the example of Figure 5 travels through the throat and toward the exit plane, the physical length c - b of region [2] becomes small. An infinite number of calculations would be necessary to reach the exit plane since the forward marching time step (see next section) is proportional to this length. In the present analysis, when c - b of region [2] is less than one percent of the total flow field length, region [2] is deleted from the computation. The downstream boundary of region [1] is adjusted to the exit plane; hence, the shock wave has left the system. Repeating this calculation with a criterion of 0.1 percent has no effect on the results other than to lengthen the computation time.

Forward Marching Stability

Explicit integration techniques applied to partial differential equations must observe a forward marching stability criterion. Other-

wise, small errors associated with the finite difference approximation grow unbounded as the solution progresses. The well-known von Neumann [46] stability analysis uses the linearized equations to predict the growth or decay of these error waves. However, the analysis is impractical to perform for the present system of equations and the result would be strictly valid only for the linearized form. The success of many numerical solutions employing the Courant-Friedrichs-Lewy (C.F.L.) Condition [47] indicates that it is an acceptable substitute. The C.F.L. Condition requires the domain of dependence of each point in the finite-difference flow field to include its physical domain of dependence. This restriction on the step size means that the speed of propagation of numerical information will equal or exceed the speed of propagation in the physical flow. This can be seen with the aid of Figure 10 where the point B' is located at the intersection of the characteristic line with the maximum slope through point A and its mirror image through point C. With the maximum slope defined as $|u| + a$, the C.F.L. Condition requires

$$\frac{\Delta x}{\Delta t} \geq |u| + a \tag{2.51}$$

or

$$\Delta t \leq \frac{\Delta x}{|u| + a} \tag{2.52}$$

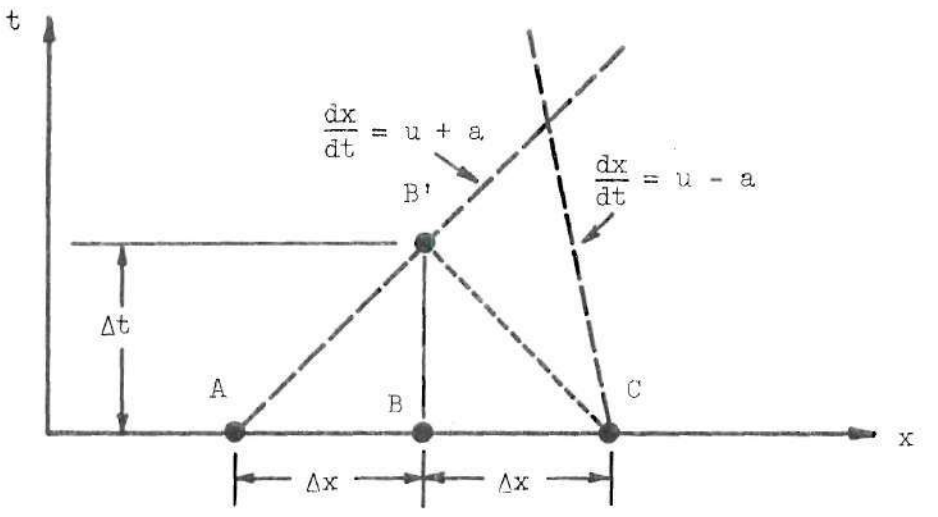

Figure 10. Illustration of the C. F. L. Condition

The present analysis uses this stability condition in the form,

$$\Delta t = 0.7 \left\{ \frac{\Delta x}{|u| + a} \right\}_{\substack{\text{minimum over} \\ \text{the flow field}}} \tag{2.53}$$

where the value of the constant was influenced by Kentzer's [48] analysis of group velocity and propagation of numerical errors.

It is sometimes reported that a well-behaved solution to a non-linear problem was gradually or even suddenly destroyed by numerical wiggles. Their appearance is often attributed to "non-linear instability". The present investigation subscribes to Moretti's [41,42] theory that numerical non-linear instability does not exist. Deterioration of a numerical solution can always be traced to an improper numerical treat-

ment. Computations which integrate continuous equations across discontinuous phenomena, incorrectly determine boundary values, or fail to recognize regions of large truncation error will generate non-physical solutions to the equations.

Recently, Cheng [36] has questioned the ability of an explicit integration technique to accurately predict oscillatory behavior. Part of the discussion is directed toward a monotonically damped wave solution of Burger's Equation, i.e.,

$$u_t + uu_x - u_{xx} = 0$$

Using the two-step Lax-Wendroff [43] technique (equivalent to a second-order Taylor series) and evaluating initial conditions and boundary values from a known analytical solution, Reference (36) shows a progressively deteriorating approximation to the known solution. The solution is no longer useful after a computation of one wave length. The failure is attributed to phase errors caused by dispersion, with the suggested cure being difference schemes of higher than second-order accuracy. This has a serious impact on the present combustion instability analysis which is required to predict oscillatory motion, with or without shock waves.

A simple test case was constructed from the general equations to examine this difficulty in detail. For small amplitude disturbances, the dependent variables can be expressed in the form,

$$p(x,t) = \bar{p}(x) + p'(x,t)$$

$$\rho(x,t) = \bar{\rho}(x) + \rho'(x,t)$$

$$u(x,t) = U(x) + u'(x,t)$$

where

$$(p'/\bar{p})^2 \ll 1 \quad \text{etc.}$$

When combustion, solid particles and mean flow are absent, Equations (2.9) and (2.11) reduce to,

Continuity

$$\frac{\partial p'}{\partial t} + \gamma \bar{\rho} a^2 \frac{\partial u'}{\partial x} = 0$$

Momentum

$$\bar{\rho} \gamma \frac{\partial u'}{\partial t} + \frac{\partial p'}{\partial x} = 0$$

where $\rho' = p'/\gamma a^2$ follows from isentropic flow. This system is equivalent to the linear second order wave equation. The behavior of simple wave motion between two solid boundaries was computed as a function of time. Following Reference (36), an exact analytical solution was used to evaluate the initial conditions and all boundary values. After three cycles, the numerical solution no longer resembled the initial wave form. However, re-running the same problem using the method of characteristics to determine boundary values resulted in a wave form that was indistinguishable from the initial wave after 23 cycles. This behavior can be explained by the fact that the analytical solution to a set of differential equations is not the same [49] as the analytical solution to the corresponding finite-difference equations. If the equations describe oscillatory motion, there is a small phase difference between the corresponding solutions which grows in time. Thus, using the exact analytical solution of the differential equations to specify boundary conditions to a numerical solution of the finite-difference equations means that a slight error is committed at the boundary. These errors propagate inward and eventually destroy the solution.

It is concluded that forward marching integration based on a second-order Taylor series expansion which observes the Courant-Friedrichs-Lewy Condition and obtains boundary values with the method of characteristics is internally consistent and hence stable.

CHAPTER III

THE COMBUSTION RESPONSE MODEL

Problem Formulation

The response model of the burning solid propellant must predict how the combustion process is altered by changes in pressure in the thin flame zone adjacent to the surface. This information is supplied to the combustion chamber analysis of Chapter II through the time-dependent quantities $\dot{m}_g$, $\dot{m}_p$, and h_c which enter the control volume perimeter boundary from the propellant flame zone. The combustion process which specifies this variation is strongly dependent on the nature of the disturbance in the chamber, suggesting the necessity of a simultaneous solution to both problems. This will be done in the present study in the following manner.

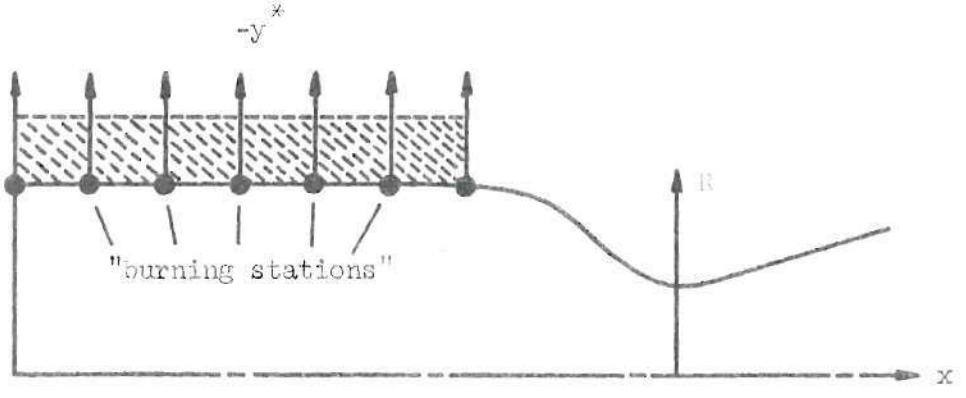

Figure 11. Method Used to Represent Cylindrically Perforated Solid Propellant

It will be assumed that the combustion of the cylindrically perforated propellant can be represented by a series of fixed burning stations as shown in Figure 11. In the flame zone adjacent to the propellant, property variations in the y direction are much greater than those in the x direction, which allows the process to be treated as one-dimensional at each station. Each local burning solution will depend in the chamber flow conditions in the control volume directly below, i.e., at the same axial location. In this way, the combustion response of the solid propellant to arbitrary disturbances in the chamber is determined by the history stored at each location, over the length of the grain.

The combustion model used at each burning station along the propellant is based on four simplifying assumptions which have been employed in nearly all combustion instability studies to date [26]. These assumptions are:

(1) The solid phase (unburned propellant) is homogeneous and one-dimensional. Thus, the analysis will be unable to distinguish between homogeneous, double-based, and composite propellants. The solution must be based on average values of propellant composition. Three-dimensional surface topological effects are lost in the one-dimensional approximation which means that the surface regression rate must be viewed as an an average rate.

(2) The conversion of the solid phase to gas is represented by a simple pyrolysis law. Usually the interface region between solid phase and the gas phase is collapsed to a plane, which effectively "lumps" all decomposition,

pyrolysis and other surface reactions into a single reaction. This overall pyrolysis reaction is taken to be an Arrhenius type, which may have either an endothermic or exothermic net heat release. The present analysis will assume

$$r^* = \text{regression rate} = B_r^* \, e^{-E_s^*/R_o T_{sur}^*}$$

where the possible pressure dependence [50] of B_r^* is neglected.

(3) Condensed phase reactions are neglected. In view of Prices [28] description of the combustion of metal loaded solid propellants, this assumption necessarily obscures important details. Except for the exploratory work of Kumar and Culick [50] with a global condensed phase reaction, this assumption is state-of-the-art. Without a proper description of the generation of solid oxide particles, the present analysis will assume that the mass flow rate of particles to the control volume, $\dot{m}_p$, is a constant fraction of the gaseous mass flow rate, $\dot{m}_g$. This fraction is taken as the percentage of metal loading in the unburned propellant.

(4) The behavior of the gas-phase flame zone is quasi-steady. The specific heats of the gas-phase constituents are the same order of magnitude as the specific heat of the solid propellant. Since the density of the unburned solid

propellant is very much greater than the density of the gas-phase, the volumetric heat capacity of the solid compared to the gas is of the order of the density ratio. This fact supports the argument that the gas-phase will adjust to thermal changes much more rapidly than the solid phase, i.e., $\frac{\partial}{\partial t}\Big|_{\text{gas-phase}} \ll \frac{\partial}{\partial t}\Big|_{\text{solid-phase}}$. In addition, the characteristic times for most chemical reactions are much smaller than thermal wave propagation times in the solid. Thus, it is assumed that the controlling time-dependent process is the thermal wave propagation in the solid, and the flame region can be described by a steady-state solution adjusted at each instant of time. This affords a great simplification if the flame temperature is assumed known, since the analysis becomes insensitive to the time-dependent kinetics and transport processes in the gas-phase flame.

The accuracy of the quasi-steady assumption is still open to question. It is often claimed that this approximation should remain valid for cases of low or intermediate frequency instabilities such as found in the present study. However, a detailed and sophisticated analysis will be required to verify this. Further comment will be made in Chapter V.

Many well-known combustion response theories based on pressure coupling have been compared in an excellent review by Culick [26]. All contain the standard assumptions outlined above, although they differ in the treatment of details. Each theory has assumed the existance of

small amplitude periodic oscillations in the gas-phase flame zone. It is shown that as a consequence of the above assumptions, each linearized analysis predicts the same two-parameter (A, B) form of the combustion response function, i.e.,

$$\mathcal{R} \equiv \frac{m'/\bar{m}}{p'/\bar{p}} = \frac{nAB}{\lambda + \lambda/A - (1 + A) + AB} \tag{3.1}$$

where m' = surface mass flow rate perturbation

p' = pressure perturbation

n = pressure index for time-independent burning

λ = function of frequency of oscillation (complex number)

The steps leading to Equation (3.1) can be found in Reference (26). This equation predicts the trend of experimental data for acoustic oscillations in a T-burner [27], etc. A plot of $\mathcal{R}$ versus Ω, defined as the ratio of frequency to burning rate squared, shows evidence of a resonance effect at a non-zero value of frequency, determined by the values of A and B (see Figure 12). The shape of the curve and the peak response varies with the values of A and B. However, even with the adjustable parameters, Equation (3.1) is not able to correlate all available experimental data. The degree of simplicity which can be tolerated in a theoretical model of the combustion process remains an open question.

The instability analysis of Levine and Culick [34] uses Equation (3.1) as the basis for the transient combustion response. Since $\mathcal{R}$ is

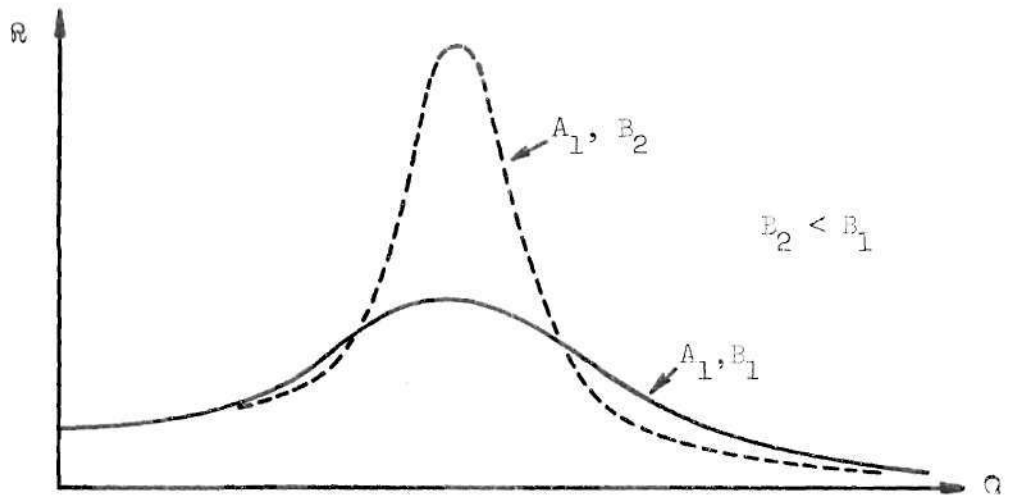

Figure 12. Typical Two-Parameter Combustion Response Curves as a Function of Frequency

a given function of frequency, an inverse Laplace transform must be evaluated to transform the results into the real-time plane. It is not clear, however, how results derived for small amplitude periodic oscillations can be applied in an analysis of the transient combustion response which may accompany arbitrary amplitude disturbances. To avoid this difficulty, the present analysis will solve the full non-linear time-dependent equations of the combustion model simultaneously with the conservation equations in the combustion chamber.

The combustion response model in the current study diverges from previous efforts in two areas; these are:

(1) It will not be assumed that a disturbance in the gas-phase is oscillating with a known frequency, and instead, the full transient behavior of the combustion response will be determined.

(2) No restrictions will be placed on the magnitudes of the gas and solid phase disturbances.

The mathematical model of the solid propellant combustion process follows from a development in Reference (34) and employs the four assumptions outlined in the beginning of this chapter. In Figure 13 is a description of the problem as seen from a coordinate system attached to the propellant surface, which is regressing at speed r^*.

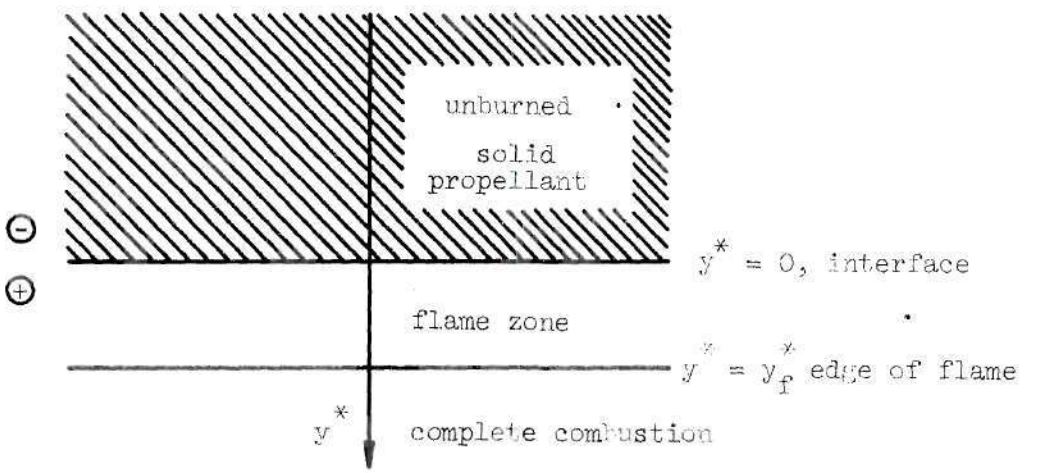

Figure 13. One-Dimensional Model of the Solid Propellant Combustion Process

At the chamber pressures involved in the present study, both diffusion and chemical kinetics will influence the structure of the flame zone. Since a detailed gas-phase solution is beyond the scope of this work, the combustion process is assumed to be distributed in such a manner that the flame zone exists from $y^* = 0$ to $y^* = y_f^*$. This is in contrast to a flame sheet approximation (i.e., all combustion occurs at $y^* = y^*_f$) which may be valid at low pressures where reaction rates are much

slower than mixing processes. A simple one-step global reaction is assumed in the flame; i.e.,

$$\text{Oxidizer} + \text{Fuel} \rightarrow \text{Products}$$

implying a gas-phase reaction rate, ω^*, proportional to p^{*2}. It is further assumed that the product of reaction rate (actually, production rate of products) and heat release, $\omega^* Q_f^*$, can be taken as constant across the width of the flame. This set of assumptions permits a separation of the problem into three distinct regions [33], each of which is analyzed individually. These are:

(1) The non-reacting solid phase ($-\infty \leq y^* \leq 0$) region. The unburned solid propellant is assumed to be incompressible and hence the equations of continuity and momentum become trivial. The energy equation can be written as,

$$\rho_s^* c_s^* \frac{\partial T^*}{\partial t^*} + \rho_s^* c_s^* r^* \frac{\partial T^*}{\partial y^*} - k_s^* \frac{\partial^2 T^*}{\partial y^{*2}} = 0 \qquad (3.2)$$

If the overall pyrolysis of solid to gas follows a first order Arrhenius type reaction, then

$$r^* = B_r^* e^{-E_s^*/R_o T_{sur}^*} \qquad (3.3)$$

where

$$B_r^* = \text{constant}$$

$$T_{sur}^* = \text{surface temperature}$$

(2) The solid-gas interface ($y^* = 0$). For a control volume with zero thickness which surrounds the plane, $y^* = 0$, the conservation of mass yields,

$$\dot{m}^* = \text{surface mass flow rate} \equiv \rho_s^* r^* \big|_{\ominus} = \rho_g^* v_g^* \big|_{\oplus} \qquad (3.4)$$

A first integral of the energy equation evaluated between the propellant side (-) and the gas flame side (+) gives

$$\dot{m}^* h_{s\,\ominus}^* - \left[k_s^* \frac{\partial T^*}{\partial y^*} \right]_{\ominus} = \dot{m}^* h_{g\,\oplus}^* - \left[k_g^* \frac{\partial T^*}{\partial y^*} \right]_{\oplus} \qquad (3.5)$$

Letting Q_s^* be the heat of reaction for the surface pyrolysis reaction,

$$Q_s^* \equiv h_{g\,\oplus}^* - h_{s\,\ominus}^* \qquad (3.6)$$

where Q_s^* is positive for an endothermic heat release, Equation (3.5) can be rewritten as,

$$\left[k_s^* \frac{\partial T^*}{\partial y^*}\right]_{\ominus} = - \dot{m}^* Q_s^* + \left[k^*_g \frac{\partial T^*}{\partial y^*}\right]_{\oplus} \tag{3.7}$$

This relationship is the basis for the time-dependent boundary condition imposed on the thermal profile in the unburned solid.

(3) The gas-phase flame zone ($0 \leq y^* \leq y_f^*$). When the assumptions of a thin flame zone and quasi-static behavior (i.e., $\frac{\partial}{\partial t} \to o$) are applied to the conservation equations for mass and momentum, the result is,

$$\rho_g^* v_g^* = \text{constant} = \dot{m}^* \tag{3.8}$$

$$p^* = \text{constant} \tag{3.9}$$

These constant values across the flame zone are the instantaneous values of mass flow rate and pressure, and hence they vary with time. The quasi-steady energy equation can be written as

$$\dot{m}^* c_p^* \frac{\partial T^*}{\partial y^*} - k_g^* \frac{\partial^2 T^*}{\partial y^{*2}} = Q_f^* \omega^* \tag{3.10}$$

where

$$Q_f^* \omega^* = \begin{cases} \text{constant} & 0 \le y^* \le y_f^* \\ 0 & y_f^* < y^* < +\infty \end{cases}$$

Again, since the reaction rate is a function of the pressure in the flame, the "constant" value of $Q_f^* \omega^*$ changes with time.

In terms of the following non-dimensional variables,

$$T \equiv T^*/T_r^*$$

$$y \equiv y^*/L^* \hat{y}_c$$

$$t \equiv t^*(a_r^*/L^*)$$

$$r \equiv r^*/a_r^* \hat{y}_c$$

$$\alpha \equiv \dot{m}^* c_p^* L^* \hat{y}_c / k_g^* \qquad (3.11)$$

$$Z_1 \equiv Q_s^*/c_s^* T_r^*$$

$$\hat{Q}(t) = \left(\frac{k_s^*}{k_g^*} \right) \left(\frac{Q_f^*}{c_s^* T_r^*} \right) \left(\frac{L^*}{\rho_s^* a_r^*} \right) \omega^*(t)$$

where

$$\omega^*(t) = \omega_{con} \, p^2 \, e^{-E_f^*/R_o T_f^*}$$

and

$$\hat{y}_c \equiv (k_s^*/\rho_s^* c_s^* a_r^* L^*)^{\frac{1}{2}}$$

the equations in the three regions can be rewritten as follows:

(1) Solid phase ($-\infty < y \leq 0$)

$$T_t + rT_y - T_{yy} = 0 \tag{3.12}$$

(2) Interface ($y = 0$)

$$T_y \big|_{\ominus} = -Z_L r + \frac{k_g^*}{k_s^*} T_y \big|_{\oplus} \tag{3.13}$$

(3) Gas phase $(0 \leq y < +\infty)$

$$\alpha T_y - T_{yy} = \hat{Q} \tag{3.14}$$

where

$$\hat{Q} = \begin{cases} \text{constant} & 0 \leq y \leq y_f \\ 0 & y_f < y < +\infty \end{cases}$$

The temperature distribution in the flame zone can be found immediately if it is assumed that the gases achieve the flame temperature when combustion is complete. Thus, if $T = T_{af}$ as $y \to +\infty$, Equation (3.14) yields

$$T(y) = T_{af} \quad \text{for} \quad (y_f \leq y < +\infty) \tag{3.15}$$

Matching the temperature and its first derivative at $y = y_f$, the thermal profile in the flame zone, $0 \leq y \leq y_f$, must be

$$T(y) = T_{af} + \frac{\hat{Q}}{\alpha}(y - y_f) + \frac{\hat{Q}}{\alpha^2}\left[1 - e^{\alpha(y-y_f)}\right] \tag{3.16}$$

$$(0 \leq y \leq y_f)$$

The temperature gradient in the gas phase at the interface is then given by,

$$T_y|_{y=0} = \frac{\hat{Q}}{\alpha} [1 - e^{-\alpha y_f}] \tag{3.17}$$

Since,

$$\omega^* y_f^* = \dot{m}^* = \rho_s^* r^*$$

it can easily be shown for the cases of interest in the present study that

$$\alpha y_f \approx 10 r^2$$

This means that the value of the exponential term in Equation (3.17) is negligible for all but very low burning rates (see also comments in Reference 34). Hence, the temperature gradient of the gases at the interface may be taken as,

$$T_y\big|_{\oplus} = T_y\big|_{y=0} = \hat{Q}/\alpha \tag{3.18}$$

Equation (3.13) can then be written as,

$$T_y\big|_{\ominus} = -Z_1 r + Z_2 r \tag{3.19}$$

where

$$Z_2 = Z_2(t) \equiv \left(\frac{k_g^*}{k_s^*}\right)\left(\frac{Q_f^*}{c_p^* T_r^*}\right)\left(\frac{L^*}{\rho_s^* a_r^*}\right)\omega^*(t)$$

This equation is the time-dependent heat transfer boundary condition imposed on the temperature profile in the solid. Thus, the system reduces to the problem of describing the behavior of the temperature distribution in the unburned solid propellant, which is governed by the following initial-value problem:

$$T_t + rT_y - T_{yy} = 0 \qquad (-\infty \le y \le 0) \tag{3.20}$$

I.C. $\qquad T(y,0) = T_o(y) \qquad$ (a)

B.C. $$T(-\infty,t) = T_{cs} \qquad (b)$$

$$T_y(0,t) = \underbrace{-Z_1(Q_s^*)r}_{\text{reaction at surface}} + \underbrace{Z_2(Q_f^*)/r}_{\text{reaction in flame}} \equiv \hat{G}(t) \qquad (c)$$

The instantaneous value of the surface temperature, $T_{sur} = T(0,t)$, predicted by this solution determines the surface regression rate r,

$$r = B_r \, e^{-E_s^*/R_o \dot{T}_{sur}^*} \qquad (3.21)$$

which specifies the mass flow rate from the surface according to

$$\dot{m} = (\rho_s^* \hat{y}_c / \rho_r^*) r \qquad (3.22)$$

Since this theory assumes a homogeneous solid phase, it is unable to distinguish between mass flow rates of gas and particles. The present analysis assumes that the weight percent loading of solids in the unburned propellant can be used directly to determine $\dot{m}_g$ and $\dot{m}_p$ which enter the control volume perimeter.

Method of Solution

The solution of Equation (3.20) is obtained with a method of

invariant imbedding discussed by Meyer [51] where the desired solution is imbedded in a family of initial value solutions as opposed to a family of boundary value solutions (e.g., see Lee [52]). Meyer's method follows from the early work of Vichnevetsky [53]. The partial differential equation at the current value of time is replaced by an ordinary differential equation in the space variable. Of course, the solution to this equation is a function of the solution at the previous time step. Then, using the theory of characteristics for an initial value problem, a general solution can be found to the ordinary differential equation in the space coordinate. Imposing the boundary conditions determines the desired solution. This technique exhibits an implicit behavior [51] which damps numerical error, and hence is stable in a forward marching sense.

For convenience, use the notation,

$$\hat{T} = \hat{T}(y) \equiv T(y, \text{ time "n"})$$

$$\hat{T}^{n-1} = \hat{T}^{n-1}(y) \equiv T(y, \text{ time "n-1"})$$

where all information is assumed known at time "n-1". Discretize the partial time derivative in Equation (3.20) with a backward difference to obtain,

$$T_t = (\hat{T} - \hat{T}^{n-1})/\Delta t \tag{3.23}$$

Substituting Equation (3.23) into Equation (3.20) results in a second-order ordinary differential equation in y at time "n", viz.

$$\hat{T}'' = r\hat{T}' + \frac{1}{\Delta t}\hat{T}' - \frac{1}{\Delta t}\hat{T}^{n-1} \tag{3.24}$$

where

$$\hat{T}' \equiv \frac{d\hat{T}}{dy}\ ,\ \hat{T}'' \equiv \frac{d^2\hat{T}}{dy^2}$$

The boundary conditions to Equation (3.24) follow directly from Equations (3.20(b)) and (c),

$$\hat{T}(-y_o) = T_{cs} \tag{3.25}$$

$$\hat{T}'(0) = \hat{G} = \hat{G}(\text{time "n"}) \tag{3.26}$$

To circumvent a numerical integration to minus infinity, the solid boundary condition is applied at the finite location, $-y_o$. Obviously,

this point must be located deeper in the solid than any thermal wave can penetrate.

By defining the variable, v, as

$$v \equiv \hat{T}' \tag{3.27}$$

Equation (3.24) can be represented by the equivalent first order system,

$$\hat{T}' = v \tag{3.28}$$

$$v' = rv + \frac{1}{\Delta t}\hat{T} - \frac{1}{\Delta t}\hat{T}^{n-1} \tag{3.29}$$

If these equations are regarded as characteristic equations for an initial value problem then characteristic theory [54] for a first order partial differential equation states that the solution of Equations (3.28) and (3.29) generates the integral surface $\hat{T}(y,v)$ of the equation (see Appendix A),

$$\frac{\partial \hat{T}}{\partial y} + \frac{\partial \hat{T}}{\partial v}\left[rv + \frac{1}{\Delta t}\hat{T} - \frac{1}{\Delta t}\hat{T}^{n-1}\right] = v \tag{3.30}$$

The general solution of Equation (3.30) can be shown [51] to have the form,

$$\hat{T}(y,v) = \theta(y)v + w(y) \tag{3.31}$$

Substitution of Equation (3.31) into (3.30) shows that $\theta(y)$ and $w(y)$ must satisfy the equations

$$\theta' = 1 - r\theta - \frac{1}{\Delta t}\theta^2 \tag{3.32}$$

$$w' = -\frac{1}{\Delta t}\theta(w - \hat{T}^{n-1}) \tag{3.33}$$

and the boundary conditions,

$$\theta(-y_o) = 0 \tag{3.34}$$

$$w(-y_o) = T_{cs} \tag{3.35}$$

which satisfy Equation (3.25). The solutions of Equations (3.32) and (3.33) specify the integral surface $\hat{T}(y,v)$ in which the desired solution

is imbedded. This particular solution is determined by satisfying the remaining boundary condition at y = 0; i.e.,

$$v|_0 = \hat{G} \tag{3.36}$$

The solutions $\theta(y)$ and $w(y)$ can be found without knowledge of v by integrating Equations (3.32) and (3.33) from $(-y_o)$ to (0). Then the above boundary condition (Equation 3.36) must be satisfied at y = 0. The regression rate r, and $\hat{G}$ which is a function of r, depend on the surface temperature

$$\hat{T}(0,v|_0) = \theta(0)\, v|_0 + w(0) \tag{3.37}$$

This means an iteration procedure is required to satisfy Equations (3.32) and (3.33) simultaneously with the boundary condition, Equation (3.36). Once the boundary condition has been satisfied, the functional form of v is found from Equation (3.29) integrated from (0) → $(-y_o)$,

$$v' = v[r + \theta(y)/\Delta t] + \frac{1}{\Delta t}\,[w(y) - \hat{T}^{n-1}] \tag{3.38}$$

Finally, the temperature profile is given by

$$T(y, \text{time "n"}) = \hat{T}(y) = \theta(y)v(y) + w(y) \qquad (3.39)$$

The advantage offered by this method is the minimum amount of computation time required. For the special case when r in Equation (3.24) is constant, only two integration passes are needed to completely determine the solution, i.e., (1) Equations (3.32) and (3.33) are integrated from $(-y_o)$ to (0), and the boundary condition Equation (3.36) is satisfied at y = 0, (2) Equation (3.38) is integrated from (0) to $(-y_o)$. When the r in Equation (3.24) is not constant, a simple but rapidly converging iteration cycle is required as mentioned above. The alternative way to solve this second-order differential equation with split boundary conditions is known as the "shooting" technique. Beginning at one end of the domain, the unknown value of the dependent variable or its derivative must be estimated, which allows the equation to be integrated to the opposite end. If the boundary condition at this end is not satisfied, the estimated boundary condition must be revised and the integration repeated. When the equation or the boundary conditions are nonlinear, this process is at best uncertain and may require a large number of iterations.

In the computer program, the solutions to Equations (3.33) and (3.38) are obtained with a numerical integration scheme based on the trapezoidal rule. Equation (3.32) is a Riccati equation which with the boundary condition Equation (3.34) can be solved analytically to give,

$$\theta(y) = [1 - e^{\xi_d(y+y_o)}]/[\xi_1 e^{\xi_d(y+y_o)} - \xi_2] \qquad (3.40)$$

$$(-y_o \le y \le 0)$$

where

$$\xi_1 \equiv \sqrt{\left(\frac{r}{2}\right)^2 + \frac{1}{\Delta t}} - \frac{r}{2}$$

$$\xi_2 \equiv -\left[\sqrt{\left(\frac{r}{2}\right)^2 + \frac{1}{\Delta t}} + \frac{r}{2}\right]$$

$$\xi_d \equiv \xi_2 - \xi_1$$

The above algorithm can be summarized as follows:

(1) $\hat{T}^{n-1}(y)$ is known; let $r = r[\hat{T}^{n-1}(0)]$

(2) Evaluate $\theta(y)$ from Equation (3.40)

(3) Solve the initial value problem

$$w' = -\frac{1}{\Delta t}\theta[w - \hat{T}^{n-1}] \; ; \; w(-y_o) = T_{cs}$$

from $y = -y_o$ to $y = 0$

(4) Determine,

$$\hat{T}(0) = \theta(0)\,\hat{G} + w(0)$$

If $r[\hat{T}(0)]$ differs from previous r, return to (2); otherwise, proceed to (5)

(5) Integrate the equation,

$$v' = v(r + \theta/\Delta t) + \frac{1}{\Delta t}\,(w - \hat{T}^{n-1})$$

from $y = 0$ to $y = -y_o$, using the initial condition $v(0) = \hat{G}$

(6) Evaluate

$$\hat{T}(y) = \theta(y)v(y) + w(y)$$

(7) Set

$$\hat{T}^{n-1}(y) = \hat{T}(y)$$

and return to step (1)

Comparison with Previous Models

With the development of the combustion model complete, it is possible to compare the final formulation in the present study with the solid propellant combustion analyses of the Princeton group, led by Summerfield. These investigations [55-59] are directed toward ignition and depressurization problems in solid propellant rockets, but the combustion process is treated in a similar manner. Each of these studies incorporates the standard assumptions (1) through (4) (see pages 56-58) or their equivalent. Hence the description of the combustion response reduces to a thermal theory (as in the present investigation) which determines a time-dependent temperature distribution in the unburned solid. The basis for comparison will be the type of initial value-boundary value problem which is derived in the solid phase region, i.e., the equivalent of Equation (3.20). Since the analyses differ as to coordinate system, nomenclature, and non-dimensionalization, the comparison in terms of symbols will be approximate.

The work of Most, et. al. [55] is an ignition study designed to predict the "start-up" thrust transient in a solid propellant rocket engine with low internal gas velocities (e.g., large port to throat area ratio). Spatial variations of static pressure and temperature in the chamber are neglected. Ignition of the propellant is assumed to occur when the surface temperature exceeds a given constant value. Above this temperature, the burning rate is given by the steady state expression, $r = ap^n$. Below this temperature, the solid undergoes a heating process due to the ignitor gases. The heating process is governed by,

$$T_t - T_{yy} = 0$$

I.C. $$T(y,0) = T_o(y)$$

B.C. $$T(-\infty,t) = T_{cs}$$

$$kT_y(0,t) \approx q_{surface} + h_{con} (T_{gas} - T_{sur})$$

$$\left[\begin{array}{l}\text{"preignition"}\\ \text{surface reactions}\end{array}\right] + \left[\begin{array}{l}\text{convective heat transfer}\\ \text{from ignitor gas}\end{array}\right]$$

Since the present analysis is concerned with the transient behavior in the engine after the propellant has ignited, this heating effect was not studied.

Krier, et. al. [56] were the first to present nonlinear results for the unsteady burning of solid propellants. Their analysis makes use of the dependence of the steady state regression rate on pressure as,

$$r = ap^n$$

and on temperature as

$$r = b(T_{sur} - T_{cs})^m$$

For values of m on the order of 10, the latter expression approximates the temperature dependence of an Arrhenius type law. Using these steady state relations to estimate instantaneous burning rates, the time dependent problem for the temperature field in the unburned solid is given by,

$$T_t + rT_y - T_{yy} = 0$$

I.C. $$T(y,0) = T_o(y)$$

B.C. $$T(-\infty,t) = T_{cs}$$

$$kT_y(0,t) \approx q_{surface}\, r + \frac{p^{2n}(p^{n/m} - q_{surface})}{r}$$

where

$$r \sim T_{sur}^m$$

There are several differences with the present analysis, but the functional form of the unsteady heat transfer boundary condition to the solid is quite similar. This system was solved numerically for assumed pressure variations in the flame which simultate ignition, depressurization, and oscillatory motion. The results show the possiblity of a run-away burning rate under certain conditions when the surface reaction is exothermic. They also indicate nonlinear wave forms for burning rate as a function of time for sinusoidal pressure oscillations in the flame. These results and a conclusion that the extent of exothermic reactions on the burning surface is a major factor in determining unstable burning rates are supported qualitatively by the present analysis (see Chapter IV).

Also discussed in Reference (56) is the important point concerning the effect of pressure variations in the flame on the flame temperature. It is often argued that high frequency disturbances occur adiabatically, which allows the instantaneous flame temperature to be computed as an isentropic function of pressure. At low frequencies, the outer region of the flame is usually assumed to be isothermal. It is quite possible that neither limiting case is true in the actual flame, as Summerfield [57,58] has pointed out. Reference (57) speculates that entropy waves may appear in the chamber as a result of the interaction between pressure disturbances and the fluctuating flame temperature. Krier, et. al. [56] were the first to present estimates of the magnitude of this entropy variation as a function of frequency. Their results (Figure 11, Reference 56) confirm that the edge of the flame zone is isothermal under conditions of a low frequency pressure

oscillation. Since the flame temperature, and hence the enthalpy of combustion, h_c, is assumed to be constant in the present analysis, the fundamental chamber frequency was computed for all the example cases and compared to Krier's predictions. In all cases, the frequencies are well inside the range where the isothermal assumption was found to be valid.

Krier's combustion model is extended in the work of Merkle, et. al. [59] where the major difference is the treatment of the gas-phase flame region. Reference (59) is concerned with the extinguishment of burning solid propellants and hence must consider the burning process at pressures much lower than the chamber pressure. The improved gas-phase flame analysis is based on Summerfield's [16] Granular Diffusion Flame theory. At low pressures (and low temperatures) the flame reaction is assumed to be kinetically controlled and at high pressures, it is diffusion controlled. The combination of these mechanisms allows both processes to be active at intermediate pressure levels, but the limiting cases are recovered at the pressure extremes. The analysis also uses an Arrhenius-type surface reaction law in place of the previous power law temperature dependence. With the exception of some assumptions regarding the gas-phase reaction rate, this analysis and the model used in the present investigation are comparable at high chamber pressures where diffusion dominates. The results presented in Reference (59) describe the extinction boundaries, i.e., the conditions under which the combustion process is quenched. No predictions were made for oscillating instability-type pressure disturbances.

The recent study of Peretz et. al. [60] presents an analysis of

the starting transient of solid propellant rocket motors with high internal gas velocities. The time-dependent behavior of the single phase flow in the combustion chamber is found with a numerical solution of the one-dimensional finite-difference conservation equations. Provisions are made for the ignitor gases and the approximate effect of the nozzle. Below a given value of ignition temperature, the propellant grain undergoes a heating process by the ignitor gases, described by

$$T_t - T_{yy} = 0.$$

I.C. $$T(y,0) = T_o(y)$$

B.C. $$T(-\infty,t) = T_{cs}$$

$$kT_y(0,t) = - h_{con}(T_{gas} - T_{sur})$$

where the heat transfer coefficient, h_{con}, is an empirical expression accounting for many effects. The problem is reduced to a single ordinary differential equation in time by assuming the spatial dependance of the temperature distribution to be a third-order polynomial. The resulting ordinary differential equation for the propellant surface temperature is solved simultaneously with the chamber flow. When the surface temperature exceeds the ignition value, the burning rate is

assumed to be predicted by

$$r = ap^n + kh_{con}\, e^{-(\beta r \rho_s / u\rho)}$$

The second term accounts for the contribution of erosive burning if the appropriate constants (k, h_{con}, β) are known. The final results for pressure transients in the engine during ignition compare well with the experimental data if the contribution of erosive burning is included. Even if the present study had included the effect of erosive burning in the above manner, comparisons with Reference (60) would be difficult due to the steady state burning experssion used after the propellant is ignited.

The related field of armament problems also requires an analysis of the solid propellant combustion problem. In place of a combustion chamber lined with propellant grain, the analysis must model a cylindrical shell partially filled with a granulated propellant, hence referred to as a porous propellant. In Kuos [61] investigation of this problem, several complex methods of predicting the time-dependent heating process of the porous propellant bed are discussed. Since the analysis is directed toward the flame spreading phenomenon, dynamic burning effects are ignored. Thus, similar to Most [55], the solution to the time-dependent heating process is obtained until an ignition temperature is achieved, and from then on, the burning rate is predicted with the steady state expression, $r = ap^n$. The time-dependent problem is solved

with an integral approach which assumes the temperature distribution in a single spherical grain is given by

$$T(t,R) = T_o \left\{ e^{\Psi(t) \frac{R}{R_p}} - \Psi(t) \frac{R}{R_p} \right\}$$

where

R_p = propellant grain radius

Substituting this expression into the initial value - boundary value problem,

$$T_t - \frac{1}{R}(RT)_{RR} = 0$$

I.C. $$T(R,0) = T_o(R)$$

B.C. $$T(0,t) = T_{cs}$$

$$T_R(R_p,t) = \frac{h_{con}}{k_s} [T_{gas} - T_{sur}]$$

results in a single ordinary differential equation in time for the unknown coefficient, $\Psi(t)$,

$$\frac{d\Psi}{dt} = \text{function } (\Psi(t),\ T_{gas},\ R_p,\ \text{etc.})$$

The solution to this equation is obtained simultaneously with the gas dynamic solution of the flow in the cylindrical shell which provides T_{gas}. The present study was unsuccessful in an attempt to use a similar approach because of the complex behavior of the temperature distribution in the solid created by an oscillatory pressure in the flame.

Kitchens [62] has studied a similar problem in porous propellants using Kuo's [61] method to describe the heating process, and hence predict the flame spreading process. He correctly noted that for a spherical propellant grain with a small radius, the interior boundary condition $T(0,t) = T_{cs}$ should be replaced by a vanishing radial derivative.

Chapter IV discusses the numerical results obtained with the combustion model derived in this chapter, as well as the chamber and nozzle flow field model discussed in Chapter II. By combining these two analyses, predictions of the transient response of the complete rocket engine with a burning propellant are obtained.

CHAPTER IV

DISCUSSION OF RESULTS

Numerical predictions of the response of a rocket engine flow field to an arbitrary disturbance are obtained with a combination of two computer codes. One code incorporates the combustion chamber and nozzle flow field analysis derived in Chapter II. The other code determines the time-dependent surface mass flow rate at a given burning station along the solid propellant as derived in Chapter III. The chamber and nozzle flow field program includes the option to accept a previously-computed flow field, superpose a continuous or shock wave disturbance on this flow field, and then restart the time integration as a new initial-value problem. In the examples of this chapter, the disturbances are introduced on the steady state flow field for the engine under consideration. The steady state flow field is computed as the asymptotic limit of the time integration, starting from the assumption that the propellant is ignited and burning in equilibrium at ambient pressure. The code which computes the time-dependent burning rate of the solid propellant can be separated from the chamber and nozzle flow field program and applied to an isolated burning station. The combustion response curves characteristic of each propellant are computed with this code by imposing a particular pressure oscillation at the flame.

The full transient behavior of the rocket engine flow field is

determined with a combination of both codes. At every time step, the combustion response program determines the propellant mass flow rate at each of the burning stations along the grain. The boundary conditions needed for determining the local burning rate are based on the instantaneous chamber flow field properties directly below, i.e., at the same axial location. The chamber and nozzle flow field variables are then integrated forward in time, and all information passing through the control volume perimeter boundary is updated. Thus, the solid propellant combustion process is solved simultaneously with the chamber and nozzle flow field.

One of the complexities of the flow field analysis of Chapter II is the tracking of moving shock waves. The computer routines which perform this operation were checked in a simple test case describing the flow in a shock tube. In this computation, the effects of combustion, solid particles and area variation are ignored. A constant area chamber with closed ends is divided by a diaphram separating regions of different pressure. At t = 0, the diaphram is removed and the time-dependent calculation tracks a shock wave propagating into the low pressure region. The flow field before and after reflection from the closed end is illustrated in Figure 14. The pressure behind the shock wave at reflection agrees with the value specified in a shock-tube manual [63]. This computation used 22 grid points and required 30 seconds on the UNIVAC 1108.

Another indication of proper operation of the computer program is its ability to compute a steady state flow field as the asymptotic limit of a time-dependent computation. For the arbitrarily selected

engine parameters shown as Case (1) in Appendix B, an ignition transient computation was started with the assumption that the propellant was burning in equilibrium at ambient pressure. The propellant mass flow rate from the surface was given by

$$\dot{m}_g = 0.1p^{0.3} \tag{4.1}$$

instead of the time dependent prediction discussed in Chapter III. The pressure at the head end of the motor is plotted as a function of time in Figure 15. With the simple burning rate law, ap^n, there is no indication of oscillatory motion as the chamber fills and the pressure rises monotonically to its steady state value. An exception was found with an unrealistically large value of the constant "a". This produced a very large initial filling rate which led to the formation of a shock wave; the shock passed through the throat and out the exit plane, leaving choked flow in the nozzle. A small amplitude wave remained in the chamber but quickly decayed. The results in Figure 15 confirm that a steady flow field is the asymptotic limit of the time-dependent integration in the computer program. Several computer experiments indicated that the same steady state flow field can be predicted by a computation whose initial condition is a reasonable approximation to the final flow field. This, of course, would be expected. Since the present study is directed toward the transient behavior of the engine after it has achieved full thrust, computations of the steady state flow field for all the

cases to follow were started from an isentropic flow initial condition. The errors in this approximate initial flow field were quickly eliminated in the time-dependent computation. All flow field variables of the steady state solution are printed on cards which can be read back into the program at a later time to restart the computation.

The steady state engine flow field obtained in the above calculation was subjected to a shock wave disturbance to study the engine response characteristics. Of course, the new calculation has exactly the same engine parameters and combustion model as the previous computation. The steady state flow field was altered with the addition of a shock wave disturbance near the head end of the chamber, simulating the effect of an explosive charge (see t = 0 flow field in Figure 16). The pressures behind the shock wave are 1.4 times the steady state values and the shock begins to propagate with a Mach number of 1.17. Figure 17 shows the pressure-time history at the head end of the chamber. The disturbance is still a shock wave on the first reflection but all other reflections indicate a continuous disturbance. Spatial pressure distributions in the motor at the four time points indicated in Figure 17 are illustrated in Figure 16. The mass flow control of a choked throat is shown by the pressure profile at point ①. The shock wave has passed through the throat leaving behind a large surge of pressure which is effectively blocked by the choked condition. At this instant, the Mach number in the geometric throat is approximately 1.2, as shown in Figure 18. This would imply that an approximate nozzle entrance-plane boundary condition which assumes a unity throat Mach number introduces unknown error into the reflection process. As the pressure surge

(in ①) propagates back upstream, it reforms into a shock wave which reflects from the head end of the chamber. The strength of the reflected shock is greatly reduced, as shown in ② . After the second nozzle reflection process, the remaining disturbance is too weak to reform into a shock wave as shown in ③ . The disturbance remains a continuous wave from here on. The distribution at point ③ also indicates the appearance of a higher mode which is following the main disturbance. This is also confirmed by the time-history in Figure 17 with the smaller pressure wavelet (at $t \cong 1.4$) which is following the main disturbance. At time point ④ , the pressure distribution shows that only small amplitude disturbances remain. The rapid decay of the original shock wave disturbance is due to two effects. The convective losses through the nozzle are very large since the area ratio is 4.0, which is unrealistically low for most solid propellant rocket engines. In addition, the combustion response of the propellant was predicted with the steady state expression, $\dot{m}_g = 0.1p^{0.3}$. The ability of this model to drive or sustain a disturbance traveling in the combustion chamber is minimal. This point has been conjectured before, and it is borne out by the present computation.

The effect of solid particles in the gas flow on the engine response was investigated in a similar fashion. The steady state combustion expression, ap^n, was used with a pressure exponent of 0.4. The area ratio of the nozzle was increased to 11.6 to reduce the large convective losses of the previous case. The behavior of two nearly identical engines (see Case 2, Appendix B) was investigated, one without particles and the other with 10μ average diameter particles at a

ten percent weight loading. A continuous disturbance (see Figure 19), whose maximum amplitude was forty percent of the chamber pressure was superposed on the steady state pressure distribution in both cases. The head end pressure-time history of the altered engine flow field with no particles is shown in Figure 20. The decay rate of the disturbance is less than in Case (1) due to the increased area ratio, but the combustion response is again too weak to sustain the disturbance. The head end pressure-time history of the similar engine with 10μ diameter particles is shown in Figure 21. The dashed curve in this figure is the same result shown in Figure 20. Comparison of the two curves reveals several anticipated trends resulting from the addition of solid particles to the flow. In this example, the small amount of higher harmonic content when no particles are present is smoothed out when the 10μ particles are added to the flow. Thus, disturbances at higher frequencies than the first fundamental mode may be strongly damped by the drag effect of the particles, if the average particle diameter is tuned to that frequency. Although this smoothing effect broadens the base of the pressure wave-form at the fundamental frequency, it does not noticeably affect the decay rate of the pressure maximums. Another prominant feature is the decrease in the effective wave speed in the gas-particle mixture over a cycle, as demonstrated by the increased time between reflections at the head end.

The computer results in the above example confirm the expected effect of solid particles. They also serve to emphasize that modeling these particles as inert spheres which create drag and dissipate energy

will not provide an explanation of why longitudinal instabilities are sometimes aggrevated with the use of metalized solid propellants. Although spherical inert particles can be expected to attenuate the high frequency unsteady motion and contribute to the broadening of lower frequency large amplitude motion, their overall importance in the present problem is secondary. For this reason, further results described in this dissertation will neglect the presence of solid particles in the flow. Consequently, any conclusions drawn from results showing a decaying disturbance without particles present remain valid; however, conclusions about the growth of disturbances must be tempered with the possible contribution of the particle flow.

The behavior of the combustion response was investigated for an isolated burning station using the time-dependent model derived in Chapter III. In each of the following examples, a given pressure-time history was imposed on the gas-phase flame. Hence, it is assumed that the mass flow response from the surface has no effect on the pressure disturbance; this is not the case when the burning stations are coupled to the chamber and nozzle flow field. For the set of propellant and flame parameters listed as Case (3) in Appendix B, the time-dependent surface mass flow rate was computed for two sinusoidal pressure oscillations, each with an amplitude of ten percent of the pressure in the flame. This example demonstrates the difference in combustion response to a low frequency ($w = 2\pi$) and a high frequency ($w = 48\pi$) disturbance. Using a time-scale non-dimensionalized by the period of oscillation, the results in Figure 22 show that the mass flow rate "leads" the low frequency pressure oscillation and "lags" the high frequency one. This

is in agreement with the results from linearized combustion response theory [26]. To demonstrate some of the nonlinear character of the time-dependent model, the two cases were rerun with a ten percent amplitude square wave pressure disturbance of the same period. The response to the square wave and the sine wave are shown together in Figure 23 for the low frequency case and in Figure 24 for the high frequency case. The responses are distinctly nonlinear. These results support a conclusion from Reference (56) that the nonlinear effect on peak to peak mass flow rate variations is diminished at high frequency. The square wave pressure disturbance is admittedly artificial, but the results demonstrate an important point. When the pressure disturbance is no longer a small amplitude sinusoidal oscillation, the nonlinearity of the system (Equation 3.20) is very important in determining the transient combustion response. Thus, predicting the response to arbitrary pressure disturbances with the results of a linearized theory could lead to large errors.

One of the important results from linearized combustion response theory is a plot of the real part of the response function, $\Re \equiv \frac{\Delta\dot{m}/\bar{\dot{m}}}{\Delta p/\bar{p}}$, as a function of the nondimensionalized frequency, Ω. A curve of this type can be constructed for each propellant system. The value at a given frequency represents the magnitude of the response to a small amplitude pressure oscillation, but it is not an indication of whether a rocket engine containing this propellant will be stable or unstable. It is a useful guide to estimating the effect of a change in mean burning rate, chamber temperature, etc., on the behavior of the propellant in the engine. A similar combustion response curve can be

predicted with the nonlinear time-dependent model by repeating the computations, shown in Figure 22 for small amplitude pressure oscillations, over a wide frequency range. A value of $\Re$ is computed from each time-dependent profile. The symbols in Figure 25 are the results of such a calculation. Also plotted on the graph is the two-parameter combustion response function predicted by linear theory for the combustion model used in the time-dependent solution. The values of A and B were computed from Equations (4.14) and (4.32) of Reference (34). The agreement is good except at the higher frequencies. However, for other propellant systems to be discussed, a similar difference between the two computations also appears at low frequencies. It is believed that these discrepancies are due to the influence of the time-dependent regression rate multiplying the temperature gradient term in Equation (3.20) and the behavior of the nonlinear boundary condition, Equation (3.20)(c).

It should be emphasized that not all propellant systems respond to a ten percent amplitude sinusoidal pressure oscillation with a sinusoidal mass flow rate. The propellant parameters used in the calculation of Figure 25 lead to what might be called a "mild" response, since the value of the maximum response (where the mass flow rate is in-phase with the pressure oscillation) is about 2.2. Other more responsive propellant systems may exhibit an entirely different combustion response, as will be evident shortly.

Predictions of engine stability require the simultaneous solution of the unsteady combustion process and the unsteady flow in the chamber and nozzle. A large number of propellant and engine parameters must be specified in any one case. With the limited time available, the

present analysis chose to study the influence of the pyrolysis reaction at the propellant surface upon engine stability. There is considerable speculation about the nature and extent of this reaction. Beckstead, Derr and Price [64] have investigated the steady state burning rate of monopropellants and composite propellants with AP as an oxidizer. Their results suggest that the net heat release of this reaction is exothermic, with a value of approximately 120 cal/gm for an AP monopropellant. Since the heat of sublimation for AP is about 585 cal/gm (endothermic), a very exothermic reaction is occurring at the surface. In an attempt to isolate the effect of this reaction, the following combustion parameters were held constant in the examples which follow:

Solid propellant:

ρ_s^* = density of propellant = 1.95 gm/cm^3 = 121.8 lbm/ft^3

T_{cs}^* = cold solid temperature = 300°K = 540°R

E_s^* = activation energy of surface reaction = 20 kcal/mole

c_s^* = heat capacity of propellant = .275 cal/gm°K = .275 BTU/lb$_m$-°R

k_s^* = thermal conductivity of propellant = 1.20 x 10^{-3} cal/cm-sec-°K

= 8.06 x 10^{-5} BTU/ft-sec-°R

Gas phase:

γ = isentropic index = 1.2

c_p^* = specific heat = 0.300 cal/gm-°K = 0.300 BTU/lb$_m$-°R

T_f^* = flame temperature = 2500°K = 4500°R

W^* = average molecular weight = 22 gm/gm-mole = 22 lb$_m$/lb$_m$-mole

E_f^* = activation energy of flame reaction = 30 kcal/mole

k_g^* = thermal conductivity = 2.0 x 10^{-4} cal/cm-sec-°K

The remaining parameters are determined by balancing the equations at steady state with typical experimental values. For example, a regression rate of 1 cm/sec at a surface temperature of 880°K determines the constant B_r^* in Equation (3.3). Using this surface temperature and the assumed value for Q_s^* the steady state energy balance across the propellant and the flame specifies the heat release term, Q_f^*, in the gas phase. Then with the value of the expected chamber pressure in the engine at steady state, the heat transfer boundary condition at the propellant surface determines the constant in the gas phase reaction rate, i.e., ω_{con} (see Equation 3.11). A sample calculation is shown in Appendix C.

A starting point in the investigation of nonlinear stability of the complete rocket engine was a propellant system with only sublimation as a surface reaction. Using the above-mentioned propellant parameters which are typical of AP propellants, and the assumption that $Q_s^* = +585$ cal/gm (+ 1,053 BTU/lb_m) endothermic, the steady state balance procedure was used to determine the remaining parameters [see Case (4), Appendix B, also Appendix C]. These values were used to compute A and B for the two-parameter combustion response function which is plotted in Figure 26. The curve is quite flat, indicating no preferential range of frequencies. In this case, a small amplitude oscillation at the fundamental frequency of the chamber, corresponding to $\Omega = 10$ in Figure 26, produces a value of mass flow response less than 0.9. The steady state flow field for this engine was altered with a shock wave disturbance in the same manner as the t = 0 plot of Figure 16. The pressure increase behind the shock is forty percent of the steady state pressure

at the same location. The pressure-time history at the head end of the chamber is shown in Figure 27. The results show that the initial shock wave has become a continuous disturbance on the first reflection, and continues to decay thereafter. The effect of the flat combustion response curve is evident as the decaying fundamental mode transfers energy to the higher harmonics. Since all modes have nearly the same value of combustion response, the higher harmonics remain prominent as the wave form decays. It is concluded that this engine is stable when perturbed by a large amplitude disturbance and, therefore it is unlikely that this system would be capable of spontaneous instability in the longitudinal mode.

The effect of an exothermic surface reaction on the stability of a rocket engine is studied in the following example. The combustion response curve in Figure 25 is the result of assuming the net heat release in the pyrolysis reaction to be 100 cal/gm, exothermic. Two engines were designed so that their fundamental frequencies operate at different points on the same curve. Referring to Figure 25, Case (5) operates at $\Omega = 10$ with a response of approximately 2. Since this point is past the peak response, the propellant mass flow rate would be expected to lag a small amplitude pressure oscillation at the fundamental frequency (and for higher harmonics). Case (6) operates at $\Omega \cong 1.5$ with a response of 1.4. At this point, the propellant mass flow rate would be expected to lead a small amplitude pressure oscillation at the fundamental frequency. It would also lead at the next two harmonics, each of which has a larger value of combustion response than the fundamental mode. Both engines were subjected to an initial shock

wave disturbance which created a forty percent increase in pressure (similar to t = 0 plot of Figure 16). The head end pressure-time history, along with the instantaneous mass flow response for the burning station located at the head end, are shown together in Figure 28 for Case (5) and in Figure 29 for Case (6). Comparison of the two figures indicates a noticeable difference in the mass flow response. For a large amplitude disturbance (particularly a shock wave), the concept of leading or lagging the pressure oscillation is augmented by the difference in the transient responses. Case 5 (lag) responds with wider and more gentle mass flow rate peaks, and with very little higher harmonic content as the pressure wave form decays. The minimum amount of higher mode content in the pressure wave form is the result of the reduced mass flow response at higher frequencies with an even greater amount of lag. Case (6) (lead) shows a sharp-peaked mass flow rate which responds right behind the shock wave, further increasing the pressure at reflection. This acts as a driver for the shock wave which is sustained for two cycles. Once the initial shock becomes a large amplitude continuous wave, the mass flow response does not lead it, but remains nearly in-phase with it. In addition to the greater magnitude of response at higher frequencies, this creates a more prominent higher harmonic content in the pressure waveform. The fact that the peak value of the disturbance after six cycles is slightly greater in Case (6) [$\mathcal{R}$ = 1.4] than Case (5) [$\mathcal{R}$ = 2.0] demonstrates the importance of the phase condition. In general, a mass flow rate which responds after the pressure disturbance has passed is not an effective driver for combustion instabilities.

The rocket engines analyzed so far have been unable to sustain large amplitude disturbances and would be considered quite stable. For the engine parameters used in these examples, the combustion response is insufficient to match the losses through the nozzle. If the exothermic heat release in the surface reaction is adjusted to 115 cal/gm, the response function increases to that shown in Figure 30. The following example [Case (7), Appendix B] employs this propellant system in the rocket engine of Case (5). Again, the operating point for the fundamental mode is $\Omega = 10$, but the combustion response magnitude has increased to approximately 3, as computed by the nonlinear time-dependent combustion model. The steady state flow field for this motor was altered with a continuous disturbance with a maximum amplitude of forty percent of the chamber pressure (same as Figure 19). The head end pressure-time history of the restarted computation is illustrated in Figure 31. At the end of the first cycle the amplitude of the disturbance has increased, but it then proceeds to decay. Thus even this response function is not sufficient to sustain the disturbance when the mass flow response lags the pressure disturbances at all chamber frequencies.

Increasing the net heat release of the surface pyrolysis reaction from 115 cal/gm to 122 cal/gm (exothermic) produces a large increase in the combustion response curve, as shown in Figure 32. This combustion model was used in the same rocket engine as discussed in the previous paragraph. The nonlinear time-dependent solution for the combustion response indicates a response value of approximately 3.6 at the fundamental frequency ($\Omega = 10$) of the combustion chamber with the new model [see Case (8), Appendix B]. The steady state flow field was altered

with a continuous disturbance with a maximum amplitude of twenty percent of the chamber pressure (see Figure 33). The head end pressure-time history of the restarted computation is shown in Figure 34. The disturbance increases at first, and then decays slowly. The out-of-phase mass flow response is still evident in the behavior of the higher modes. To investigate the possibility of triggering this engine with a larger amplitude disturbance, the computation was rerun with a forty percent amplitude continuous disturbance (Figure 33) of the same shape. The head end pressure-time history along with the instantaneous mass flow rate for the burning station at the same location are shown in Figure 35. This plot indicates the possible formation of a limit cycle oscillation at nearly twice the initial disturbance amplitude. However, a dramatic change is evident in the character of the mass flow response. This behavior is a sharp but finite-amplitude "spike". As would be expected, when the burning rate spikes, the flow field pressure also rises sharply at the same location.

The phenomenon of a burning rate spike was not anticipated when the computational method was constructed. Although provisions were made for traveling discontinuities, the region between any two moving boundaries was assumed to be smooth and continuous. Hence, a Taylor series truncated after the second order term is the basis for the forward marching time integration of the conservation equations. As an illustration, consider the homogeneous equations for gas flow only:

$$f_t + Af_x = 0$$

where f is a vector with components ρ, u, and S, and A is the appropriate coefficient matrix. If this system is expanded in a second-order Taylor series, the truncation "error" is given by (41)

$$\frac{1}{6}\left[Af_{xxx}\,\Delta t\Delta x^2 + f_{ttt}\,\Delta t^3\right] + \ldots$$

If a mass flow spike creates a similar disturbance in f, then f_{ttt} and f_{xxx} can become significant (also, see Appendix D). Thus, integrating the flow field equations with the present scheme introduces unknown truncation errors whenever the mass flow spikes. There is no obvious way to properly account for this phenomenon within the present computational method without recourse to unreasonably small values of Δt and Δx. Thus, flow field predictions which include mass flow rate spikes are assumed to represent the proper trend in the rocket engine, but the numerical values have unknown accuracy. Hence, no attempt was made to compute the final form of a limit cycle oscillation in the motor under these conditions.

The behavior of the nonlinear combustion model can be studied in more detail without the combustion chamber analysis and its associated truncation error. The following results were generated by the computer code which solves the time-dependent burning problem at a single burning station for any assumed pressure variation in the flame zone. Each calculation used 1000 time "steps" per cycle of pressure oscillation and the convergence criterion for satisfying the boundary

condition at the interface was seven significant digits. The response of the combustion model used in case (8) [i.e., Figure 32, $Q_s^* = -122$ cal/gm] was determined for several sine wave pressure oscillations at the fundamental frequency of the chamber ($\Omega = 10$). Figure 36 shows the mass flow response to a sinusoidal pressure oscillation with an amplitude of five percent of the mean chamber pressure (note: the time scale is nondimensionalized by the period of the pressure oscillation, i.e., $\bar{t} = 5$ is the end of the fifth cycle). After a transient adjustment during the first cycle, the mass flow rate establishes a sinusoidal-type wave form. Closer inspection reveals that the maximum values of this wave form alternate between a high and low value for successive cycles. The minimum values are the same. The alternating high-low trend is very pronounced when the amplitude of the pressure oscillation is increased to ten percent as shown in Figure 37. This result shows a transient behavior which leads to a spike on the fifth cycle. Repeating the same calculation with a fifteen percent amplitude pressure oscillation produces an alternating pattern of spikes on every other cycle as shown in Figure 38. Finally, increasing the amplitude of the pressure oscillation to twenty percent results in a similar wave form which repeats every two cycles (see Figure 39).

These predictions of combustion response are based on sinusoidal pressure oscillations at a single frequency, corresponding to $\Omega = 10$ on the response curve shown in Figure 32. Since the surface mass flow rate lags a small amplitude pressure oscillation at this frequency, it was decided to investigate the lead portion of the curve in the same way. A lead case was chosen at $\Omega = 3$ because the combustion

response magnitude is almost identical to that at $\Omega = 10$. The propellant mass flow rate due to a five percent amplitude sinusoidal pressure oscillation at $\Omega = 3$ is shown in Figure 40 (note: the time scale is nondimensionalized by the period of the pressure oscillation). The response to a six percent pressure oscillation is also shown on the same graph. Comparison of the two curves illustrates the evolution of the spike and the small amplitude peak seen in the previous results. However, the phase characteristic plays an important role. For pressure oscillations at $\Omega = 10$, the spikes formed after the pressure maximum; at $\Omega = 3$, they appear to be forming before the pressure maximum. This is confirmed when the pressure amplitude is increased to ten percent as shown in Figure 41. Note that this wave-form is similar to that in Figure 39 which required a twenty percent amplitude pressure oscillation. However, the oscillation at $\Omega = 3$ leads to a spike on every cycle, where at $\Omega = 10$ the spike occurred on every other cycle.

It is also of interest to determine the nonlinear behavior of the combustion model at the frequency corresponding to the maximum response value. This was carried out for a combustion model with a net heat release at the surface of 120 cal/gm (exothermic). The corresponding combustion response curve is shown in Figure 42, which indicates that the mass flow rate should be in-phase with a small amplitude pressure oscillation at a frequency of $\Omega = 5.5$. The mass flow response due to a sinusoidal pressure oscillation at $\Omega = 5.5$ with an amplitude of one percent of the mean pressure in the flame is shown in Figure 43a. After a short transient period, the wave form shows no evidence of the nonlinear influence. Repeating this

calculation with a five percent amplitude pressure oscillation produces the distorted wave-form shown in Figure 43b. This closely resembles the result shown in Reference (56) for a ten percent pressure oscillation in a combustion model with H = .80 ($H \equiv - Q_s^*/c_s^*(T_{sur}^* - T_{cs}^*) = 0.75$ in the present example). If the pressure amplitude is increased to 7.5 percent, the mass flow response behaves in the transient manner shown in Figure 43c. A spike occurs just after the pressure maximum on the second cycle, but does not reappear until the fifth cycle. This behavior seems to indicate the existence of a threshold amplitude criterion, possibly including a time derivative, which must be exceeded before a spike can occur on every cycle. Whatever the criterion, it is exceeded when the pressure oscillation amplitude is increased to ten percent, as shown in Figure 43d. After the transient adjustment of the first cycle, the mass flow response is characterized by a repeating pattern of spikes. In the response to a 7.5 percent amplitude oscillation, the two mass flow rate spikes occurred <u>after</u> the pressure maximums. In the response to a ten percent amplitude oscillation, the spikes are exactly in-phase with the pressure maximums. This type of combustion response would exert a substantial driving force on a disturbance in the combustion chamber.

The combustion response spike can be examined in more detail with a semi-log plot on an expanded time scale. The mass flow rate between $\bar{t} = 3.20$ to 3.30 shown in Figure 43d is replotted in Figure 44. This time interval corresponds to 0.543 mil-sec in real time. Most of the "spike" occurs in $1/10^{th}$ of this time, of $1/100^{th}$ of the pressure oscillation. Since the spike takes place over a short time interval, it would be expected that the related temperature fluctuations in the

solid propellant will be restricted to a region close to the surface. Three temperature profiles in the unburned solid are shown in Figure 45 for the "spike" illustrated in Figure 44. The temperature profile ① at $\bar{t} = 3.022$ is before the peak, profile ② at $\bar{t} = 3.245$ is at the peak, and profile ③ at $\bar{t} = 3.283$ occurs after the peak. The temperature profile at $\bar{t} = 4.022$, i.e., one cycle later, is identical to that in ①. During the spike, the movement of the time-dependent temperature distribution in the solid is seen to be confined within three non-dimensional unit-depths from the surface. For this propellant system, three units represents 1.3×10^{-2} cm. Actually, the large amplitude temperatures propagate inward less than $1/10^{th}$ of this distance. Thus, temperature fluctuations very close to the propellant surface play a dominant role in the unsteady mass flow response.

The temperature distribution at the peak of the spike shows that a severe gradient at the surface is sustained for a short time. If the thermal conductivity of the unburned propellant were increased, this should produce a noticeable effect on the surface temperature fluctuations. The propellant system (Figure 42) which exhibits the repeating spikes shown in Figure 43d was altered by doubling the thermal conductivity of the solid propellant ($k^*_{s_{new}} = 2.4 \times 10^{-3}$ cal/sec-°K-cm). All other physical properties remained the same. This new system responds to the same ten percent amplitude pressure oscillation in the flame with the mass flow rate shown in Figure 46. The results show no trace of any spike. This change can also be reasoned from the combustion response curve shown in Figure 42. Doubling the thermal conductivity does not change the response curve, but it does shift the frequency of the

operating point. Thus, the results in Figure 46 are for a pressure disturbance at $\Omega = 11$, which is well into the lag portion of the curve. The fact that Figure 46 resembles Figure 36 is to be expected. Another important parameter governing the mass flow response is the activation energy of the surface pyrolysis reaction. Decreasing the value of the activation energy will substantially reduce the sensitivity of the regression rate to temperature variations. The propellant system with the response curve shown in Figure 42 was again altered by assuming the activation energy of the surface reaction, E_s^*, to be 10 kcal/mole. This new system was subjected to the same ten percent amplitude pressure oscillation which led to the repeating spikes of Figure 43d. The mass flow response is shown in Figure 47 to be a nearly perfect sine wave. This change might also be anticipated from the movement of the combustion response curve. Plotted on Figure 42 is the linear combustion response curve for the above propellant system with $E_s^* = 10$ kcal/mole. The operating frequency is still $\Omega = 5.5$, but the magnitude of the response is only slightly greater than unity. This accounts for the sinusoidal mass flow response shown in Figure 47.

In the study up to this point, all computations of the transient behavior of the complete rocket engine have been initiated with a large amplitude disturbance. Since longitudinal combustion instabilities in actual engines seem to arise spontaneously, they presumably originate from small amplitude unorganized disturbances which may be present in the chamber. The propellant system with $Q_s^* = -120$ cal/gm, whose combustion response curve is shown in Figure 42, was employed in a rocket engine [see Case (9), Appendix B] designed to operate near the peak

response. The propellant mass flow rate should be in-phase with a small amplitude pressure oscillation at the fundamental frequency of the chamber in Case (9). The steady-state flow field for this motor was altered with a ten percent amplitude continuous disturbance, with the same shape as shown in Figure 33. The time-history of the pressure at the head end of the chamber is shown in Figure 48 for the restarted computation. The instantaneous propellant mass flow rate at the same location is also shown in the figure. The results show that the disturbance is sustained at approximately the initial amplitude for two cycles. However, after the second reflection, the mass flow rate spikes creating a related jump in pressure. As mentioned before, the truncation error introduced into the time-dependent flow field by this behavior of the propellant burning rate will compromise its accuracy. Thus, the flow field response beyond $t = 1.3$ must be interpreted as a trend. The results show an unmistakable trend toward a large amplitude disturbance which becomes a shock wave by the sixth reflection. Thus, within the accuracy limits of the present computational scheme, a propellant system described by typical values of an AP-propellant is shown to be capable of driving a small amplitude disturbance into a large amplitude axial instability in the solid propellant rocket engine.

CHAPTER V

CONCLUSIONS AND RECOMMENDATIONS

A mathematical model describing the behavior of a solid propellant rocket engine with a cylindrically perforated propellant grain has been developed to predict the time-dependent response of the engine flow field to arbitrary disturbances. The solution includes the unsteady flow in the nozzle. The equations describing the pressure-coupled combustion response of the burning solid propellant are solved simultaneously with the chamber and nozzle flow field. The results obtained confirm that:

(a) The unsteady flow in the choked nozzle is important in determining how disturbances in the engine are reflected in the throat region. Specifically, when large amplitude disturbances are present, the Mach number in the geometric throat cannot be assumed to remain at unity.

(b) The ability of typical diameter, inert, mono-disperse solid particles to damp low frequency axial motion is minimal. Although the drag force due to the suspended inert particles will smooth out higher frequency disturbances, the overall effect of inert particles is secondary. However, if properly modeled, the actual particle formation process and the energy release associated with metal combustion in the gas-phase may play a dominant role in longitudinal instability, under certain conditions.

(c) For all flow fields examined, the steady state propellant burning rate law, $r = ap^n (n < 1)$, was incapable of sustaining longitudinal instabilities. This indicates that the dynamic burning rate characteristics of solid propellants cannot be ignored in a study of the transient behavior of a solid propellant rocket motor.

The following conclusions can be drawn from the present results for rocket engine flow field response to arbitrary disturbances:

(1) A pressure-coupled solid propellant combustion model, based on commonly employed assumptions, predicts that large amplitude burning rate spikes will occur under certain conditions when the net heat release in the surface reaction is exothermic. Thus, the details of the condensed phase of the combustion process near the surface are extremely important.

The predictions of this model must be interpreted within the constraints of the assumptions. Certainly, including a more sophisticated model of condensed phase reactions and treating the gas-phase flame as truly time-dependent may alter these predictions somewhat. The important point is, however that small amplitude pressure oscillations in the flame do not necessarily result in small amplitude propellant burning rates.

(2) With this combustion model, the numerical solution for the rocket engine flow field predicts the possibility that small amplitude disturbances may grow into large amplitude axial instabilities. These numerical results must be interpreted as a trend when the burning rate exhibits spikes, as a result of the unavoidable truncation errors in the time integration scheme. However, it appears that even without

the contribution of velocity coupling, the combustion response due to pressure coupling alone has the potential for driving large amplitude axial instabilities.

(3) Marxman's [14] conclusion that a combustion response magnitude of 3 to 4 is the minimum value needed to sustain large amplitude axial instability is qualitatively correct. However, the phase relationship between the mass flow rate of the burning propellant and the pressure disturbance is extremely important. If the disturbances in the engine achieve large amplitudes, a propellant system operating on the lead portion of the combustion response curve will be considerably more effective in driving an instability than one operating on the lag portion of the curve.

Toward the goal of making quantitative predictions of the susceptibility of a given rocket engine and propellant system to axial instability, it is recommended that the following two areas receive further attention:

(1) The solid propellant combustion process must be modeled in greater detail by removing the assumptions of a quasi-steady flame and no condensed phase reactions. A thorough study of the time-dependent behavior of this model should indicate what changes occur in the spikes found by the present analysis. If the sharp, finite-amplitude burning rate spikes remain, then a new method of integrating the conservation equations in the chamber will be required.

(2) To deal with metal-loaded composite propellants, the solid particle formation process including the combustion of molten metal agglomerates entrained in the gas flow must be accounted for in the

model. This has the potential of being a significant energy source for driving axial instabilities.

These improvements, added to the capabilities of the present analysis, should be a significant step toward "a priori" predictions of axial instabilities in rocket systems in the design stage.

APPENDIX A

DERIVATION OF EQUATION (3.30), CHAPTER III

Following Sneddon's [54] work, consider a linear first-order partial differential equation of the form,

$$P(x,y,z)\frac{\partial z}{\partial x} + Q(x,y,z)\frac{\partial z}{\partial y} = R(x,y,z) \tag{A.1}$$

The solution to Equation (A.1) is an arbitrary function of the solutions to the characteristic equations

$$\frac{dx}{P} = \frac{dy}{Q} = \frac{dz}{R} \tag{A.2}$$

or

$$\frac{dz}{dy} = R/Q \tag{A.3}$$

$$\frac{dx}{dy} = P/Q \tag{A.4}$$

To form the analogy with Equations (3.28, 3.29), let

$$\hat{T} \rightarrow z$$

$$v \rightarrow x$$

$$y \rightarrow y$$

then,

$$\frac{d\hat{T}}{dy} = R/Q \quad . \tag{A.5}$$

$$\frac{dv}{dy} = P/Q \tag{A.6}$$

Then if,

$$R(\hat{T}, v, y) = v$$

$$Q(\hat{T}, v, y) = 1$$

$$P(\hat{T}, v, y) = rv + \frac{1}{\Delta t} (\hat{T} - \hat{T}^{n-1})$$

the characteristic equations [Equations (A.5, A.6)] become

$$\hat{T}' = v$$

$$v' = rv + \frac{1}{\Delta t} (\hat{T} - \hat{T}^{n-1})$$

which are identical to Equations (3.28, 3.29). The solution to this system must then yield the solution to

$$\frac{\partial \hat{T}}{\partial y} + \frac{\partial \hat{T}}{\partial v} [rv + \frac{1}{\Delta t} (\hat{T} - \hat{T}^{n-1})] = v$$

by comparison with Equation (A.1). This is Equation (3.30).

APPENDIX B

ENGINE AND PROPELLANT PARAMETERS USED IN COMPUTATIONS

Case (1)

Chamber radius	= 1.0 ft.	Chamber temperature	= 4500°R
Engine length	= 10.0 ft.	Chamber pressure	$\cong$ 1950 psia
Grain length	= 8.0 ft.	$\dot{m}_g$	= $0.1p^{0.3}$
Nozzle area ratio	= 4.0	Isentropic index	= 1.20

Case (2)

(a) without particles:

Chamber radius	= 1.0 ft.	Chamber temperature	= 4500°R
Engine length	= 10.0 ft.	Chamber pressure	$\cong$ 397 psia
Grain length	= 8.0 ft.	$\dot{m}_g$	= $0.008p^{0.4}$
Nozzle area ratio	= 11.65	Isentropic index	= 1.20

(b) with 10μ diameter paricles

Chamber radius	= 1.0 ft.	Chamber temperature	= 4500°R
Engine length	= 10.0 ft.	Chamber pressure	$\cong$ 394 psia
Grain length	= 8.0 ft.	$\dot{m}_g$	= $0.008p^{0.4}$
Nozzle area ratio	= 11.65	$\dot{m}_p$	= 0.1 $\dot{m}_g$
K	= 54.56	Isentropic index	= 1.20

Case (3)

Flame temperature = 4500°R

Flame pressure $\cong$ 1000 psia

Isentropic index = 1.20

Mean molecular weight = 29 lb_m/lb_m-mole

$Q_s^* = -100$ cal/gm $\qquad Q_f^* = 545$ cal/gm

$c_s^* = 0.275$ cal/gm-°K $\qquad c_p^* = 0.300$ cal/gm-°K

$k_s^* = 1.2 \times 10^{-3}$ cal/cm-sec-°K $\qquad k_g^* = 2.0 \times 10^{-4}$ cal/cm-sec-°K

$\rho_s^* = 1.95$ gm/cm^3 $\qquad E_f^* = 30$ kcal/mole

$E_s^* = 20$ kcal/mole

$$r^* = 1.0 \text{ cm/sec} \ @ \ p^* = 1000 \text{ psia}, \ T_{sur}^* = 880°K$$

All the cases listed below include the following values unless otherwise noted:

Solid propellant:

$\rho_s^* = 1.95$ gm/cm^3 = 121.8 lb_m/ft^3

$T_{cs}^* = 300°K = 540°K$

$c_s^* = 0.275$ cal/gm-°K = 0.275 BTU/lb_m-°R

$k_s^* = 1.20 \times 10^{-3}$ cal/cm-sec-°K = 8.06×10^{-5} BTU/ft-sec-°R

$E_s^* = 20$ kcal/mole

Gas phase:

$\gamma = 1.20$

$T_f^* = 2500°K = 4500°R$

$c_p^* = 0.300$ cal/gm-°K = 0.300 BTU/lb_m-°R

$k_g^* = 2.0 \times 10^{-4}$ cal/cm-sec-°K

$= 1.342 \times 10^{-5}$ BTU/ft-sec-°R

$E_f^* = 30$ kcal/mole

$W^* = 22$ gm/gm-mole = 22 lb_m/lb_m-mole

Engine:

Chamber radius = 1.0 ft.

Engine length = 10.0 ft.

Grain length = 8.0 ft.

Case (4)

Nozzle area ratio = 11.65

Chamber pressure $\tilde{=}$ 396 psia

$Q_s^* = 1053.$ BTU/lb_m (endothermic)

$Q_f^* = 2215.$ BTU/lb_m (exothermic)

$r^* = 0.507$ cm/sec @ $p^* = 400$ psia, $T_{sur}^* = 880°K$

Case (5)

Nozzle area ratio = 11.65

Chamber pressure $\tilde{=}$ 397 psia

$Q_s^* = -180.0$ BTU/lb_m (exothermic)

$Q_f^* = 981.8$ BTU/lb_m (exothermic)

$r^* = 0.507$ cm/sec @ $p^* = 400$ psia, $T_{sur}^* = 880°K$

Case (6)

Nozzle area ratio = 11.1

Engine length = 15.0 ft.

Grain length = 13.0 ft.

Chamber pressure $\tilde{=}$ 1010 psia

$Q_s^* = -180.0$ BTU/lb_m (exothermic)

$Q_f^* = 981.8$ BTU/lb_m (exothermic)

$r^* = 1$ cm/sec @ $p^* = 1000$ psia, $T_{sur}^* = 880°K$

Case (7)

Nozzle area ratio = 11.65

Chamber pressure $\cong$ 397 psia

$Q_s^* = -207.0$ BTU/lb_m (exothermic)

$Q_f^* = 954.8$ BTU/lb_m (exothermic)

$r^* = 0.507$ cm/sec @ $p^* = 400$ psia, $T_{sur}^* = 880°K$

Case (8)

Nozzle area ratio = 11.65

Chamber pressure $\cong$ 397 psia

$Q_s^* = -220.0$ BTU/lb_m (exothermic)

$Q_f^* = 941.8$ BTU/lb_m (exothermic)

$r^* = 0.507$ cm/sec @ $p^* = 400$ psia, $T_{sur}^* = 880°K$

Case (9)

Nozzle area ratio = 12.1

Grain length = 8.5 ft.

Chamber pressure $\cong$ 600 psia

$Q_s^* = -216.0$ BTU/lb_m (exothermic)

$Q_f^* = 945.8$ BTU/lb_m (exothermic)

$$r^* = 0.685 \text{ cm/sec} \; @ \; p^* = 600 \text{ psia}, \; T^*_{sur} = 880^\circ K$$

APPENDIX C

SAMPLE CALCULATION OF CONSTANTS IN COMBUSTION THEORY

The following computation applies to Case (4) of Appendix B where the heat release associated with the surface reaction was assumed to be 1,053 BTU/lb_m, endothermic. The information below is assumed known from experimental data:

$$r^* = 1.667 \times 10^{-2} \text{ ft/sec}$$

at $$p^* = 400 \text{ psia}, \quad T^*_{sur} = 1585^\circ R$$

This is in addition to:

$$\rho^*_s = 121.8 \text{ lb}_m/\text{ft}^3$$
$$c^*_s = 0.275 \text{ BTU/lb}_m{}^\circ R$$
$$k^*_s = 8.06 \times 10^{-5} \text{ BTU/ft-sec-}^\circ R$$
$$E^*_s = 20 \text{ kcal/mole}$$
$$T^*_{cs} = 540^\circ R$$

$$c^*_p = 0.300 \text{ BTU/lb}_m{}^\circ R$$
$$k^*_g = 1.342 \times 10^{-5} \text{ BTU/ft-sec-}^\circ R$$
$$T^*_f = 4500^\circ R$$
$$E^*_g = 30 \text{ kcal/mole}$$
$$\gamma = 1.20$$

$$W^* = 22 \text{ lb}_m/\text{lb}_m\text{-mole}$$

Three parameters (B_r^*, Q_f^*, ω_{con}) must be determined.

(1) $$r^* = B_r^* e^{-E_s/R_o T_{sur}^*} \qquad \text{Equation (3.3)}$$

$$\rightarrow B_r^* = r^* e^{+E_s^*/R_o T_{sur}^*} = 1.535 \times 10^{-3} \text{ ft/sec}$$

(2) Overall heat balance yields,

$$Q_f^* = Q_s^* + c_s^*(T_{sur}^* - T_{cs}^*) + \dot{c}_p^*(T_f^* - T_{sur}^*)$$

$$= 2{,}215 \text{ BTU/lb}_m$$

(3) Integrated energy equation applied across interface,

$$\left[k_s^* \frac{\partial T^*}{\partial y^*}\right]_{\ominus} = -\dot{m}^* Q_s^* + \left[k_g^* \frac{\partial T^*}{\partial y^*}\right]_{\oplus}$$

or

$$T_y\Big|_{-} = -Z_1 r + Z_2/r \qquad \text{Equation (3.19)}$$

where

$$Z_1 \equiv Q_s^*/c_s^* T_r^* \,, \quad r \equiv r^*/a_r^* \hat{y}_c$$

$$Z_2 \equiv \left(\frac{k_g^*}{k_s^*}\right)\left(\frac{Q_f^*}{c_p^* T_r^*}\right)\left(\frac{L^*}{\rho_s^* a_r^*}\right)\omega^*$$

$$\omega^* = \omega_{con}\, p^2\, e^{-E_f^*/R_o T_f^*},\quad \hat{y}_c \equiv (k_s^*/\rho_s^* c_s^* a_r^* L^*)^{\frac{1}{2}}$$

Now, at steady state

$$T_y\big|_{\ominus} = (T_{sur} - T_{cs})r$$

Rearranging Equation (3.19)

$$Z_2 = (T_y\big|_{\ominus}\, r + Z_1 r^2)$$

or

$$\omega^* = \frac{\left[(T_{sur} - T_{cs}) + \left(\frac{Q_s^*}{c_s^* T_r^*}\right)\right] r^2}{\left(\frac{k_g^*}{k_s^*}\right)\left(\frac{Q_f^*}{c_p^* T_r^*}\right)\left(\frac{L^*}{\rho_s^* a_r^*}\right)}$$

finally,

$$\omega_{con} = \frac{\left[(T_{sur} - T_{cs}) + \left(\frac{Q_s^*}{c_s^* T_r^*}\right)\right] r^2}{p^2 e^{-E_f^*/R_o T_f^*}\left(\frac{k_g^*}{k_s^*}\right)\left(\frac{Q_f^*}{c_p^* T_r^*}\right)\left(\frac{L^*}{\rho_s^* a_r^*}\right)}$$

$$= 3.159 \times 10^{4} \text{ lb}_m/\text{ft}^3\text{-sec}$$

if $L^* = 10$ ft, $a_r^* = 1{,}208$ ft/sec $T_r^* = 540°R$

$p_r^* = 14.7$ psia

APPENDIX D

SOME COMMENTS ON TRUNCATION ERROR

The basis for the explicit time integration of the conservation equations in the region between two boundaries (see Chapter II) is a Taylor series expansion, truncated after the second order term. Implied in this method, as with any technique based on a second-order Taylor series (Lax-Wendroff, MacCormack's), is the assumption that all higher order terms can be neglected. This is easily justified when the flow field distributions change slowly in time and space. If the distributions change rapidly, then the truncated terms are negligible only when the increments in time and space are appropriately small.

A rough estimate of the accuracy obtained with the second-order Taylor series expansion in time used in the present study can be determined with an after-the-fact calculation. At a given point in space, the second order expansion is

$$\tilde{p}_1 = p_o + p_t|_o \Delta t + p_{tt}|_o \Delta t^2/2 \qquad (D.1)$$

where $( )_1 \rightarrow t + \Delta t$

$( )_o \rightarrow t$

Of course, the actual value of p_1 is given by

$$p_1 = \tilde{p}_1 + p_{ttt}\Big|_o \frac{\Delta t^3}{6} + \ldots \text{ h.o.t.} \qquad (D.2)$$

Using centered finite-differences for the indicated time derivatives, the values of both terms on the right-hand side of Equation (D.2) were computed for the pressure time-history at the head end of the chamber shown in Figure 34. The average value of the second term, i.e., the truncation error, was found to be less than $1/100^{th}$ of one percent of $\tilde{p}_1$. This is considered entirely acceptable. However, this level of accuracy represents only a necessary condition, and is not sufficient proof that the internal computation procedure is equally as precise.

To determine the accuracy of the second-order Taylor series expansion of the coupled system of five equations in five unknowns would require a lengthy computation. As indicated in Chapter II, the conservation equations are manipulated so that the first and second time derivatives in Equations (2.24) through (2.28) can be expressed in terms of spatial derivatives at the current value of time. Extending this proceedure to include the third time derivatives becomes complex due to the coupling in the system. However, without writing out the third-order terms, a rough estimate of the possible truncation error associated with the spatial derivatives used in the second-order expansion can be made after-the-fact. The centered-difference expressions for the first and second spatial derivatives at a mesh point m are given by

$$\left.\frac{\partial p}{\partial x}\right|_m \underset{\text{finite-difference}}{} = \frac{p_{m+1} - p_{m-1}}{2\Delta x} \qquad (D.3)$$

$$\left.\frac{\partial^2 p}{\partial x^2}\right|_m \underset{\text{finite-difference}}{} = \frac{p_{m+1} - 2p_m + p_{m-1}}{\Delta x^2} \qquad (D.4)$$

It can easily be shown that the truncation error associated with these approximations are

$$\left.\frac{\partial p}{\partial x}\right|_m \underset{\text{actual}}{} = \left(\frac{p_{m+1} - p_{m-1}}{2\Delta x} \right) - \frac{\Delta x^2}{6} p_{xxx}|_m + \text{h.o.t.} \qquad (D.5)$$

$$\left.\frac{\partial^2 p}{\partial x^2}\right|_m \underset{\text{actual}}{} = \left(\frac{p_{m+1} - 2p_m + p_{m-1}}{\Delta x^2} \right) - \frac{\Delta x^2}{12} p_{xxxx}|_m + \text{h.o.t.} \qquad (D.6)$$

It is assumed here that the truncation error, or the second term on the right-hand side, can be calculated by centered finite-differences from a spatial flow field predicted by the computer program. Using this after-the-fact method, it was found that the truncation errors could be as much as five percent of the value of the finite-difference derivatives, Equations (D.3) and (D.4), at certain local points when the pressure

wave-form had attained large amplitudes. A more extensive calculation would be required to determine how this local error affects the integration of the system of equations. However, this order of magnitude estimate indicates the possibility that the spatial mesh system should have included a greater number of grid points when disturbances reached large amplitudes in the engine flow field.

APPENDIX E

FIGURES FOR CHAPTER IV

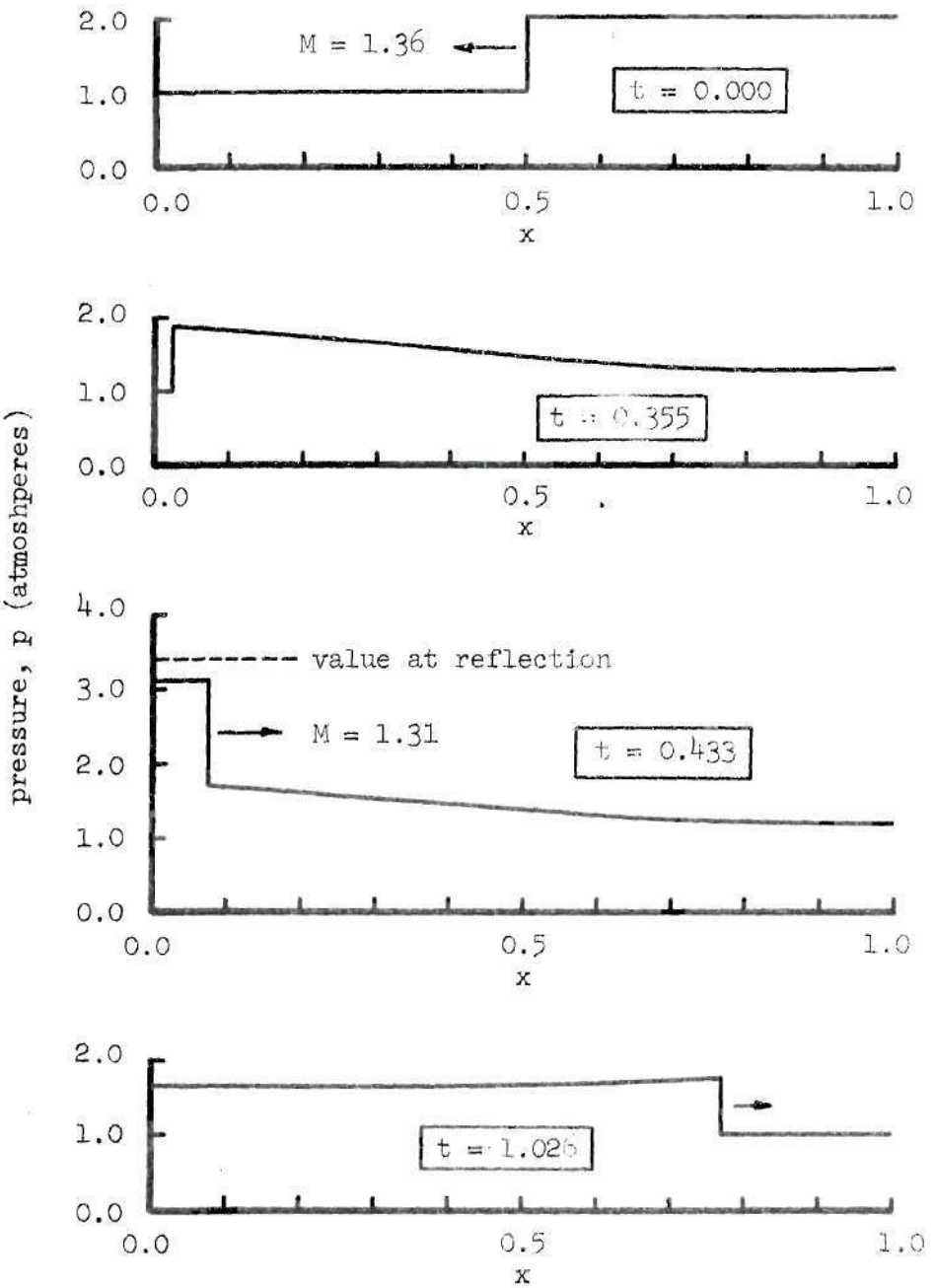

Figure 14. Propagation of a Shock Wave in a Closed Chamber

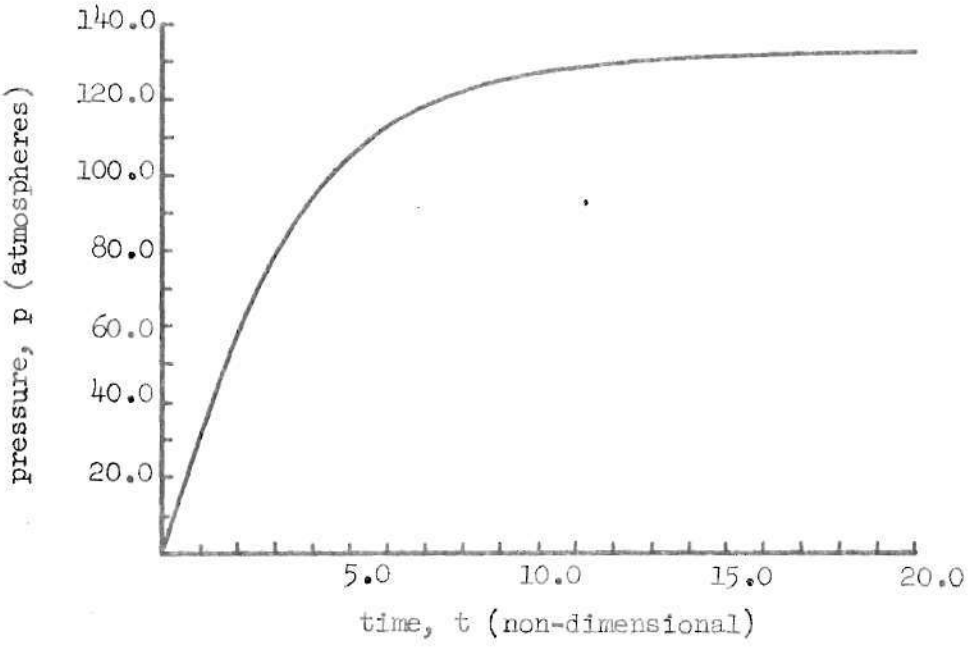

Figure 15. Pressure-Time History at the Head End of the Combustion Chamber During the Ignition Transient For Case (1)

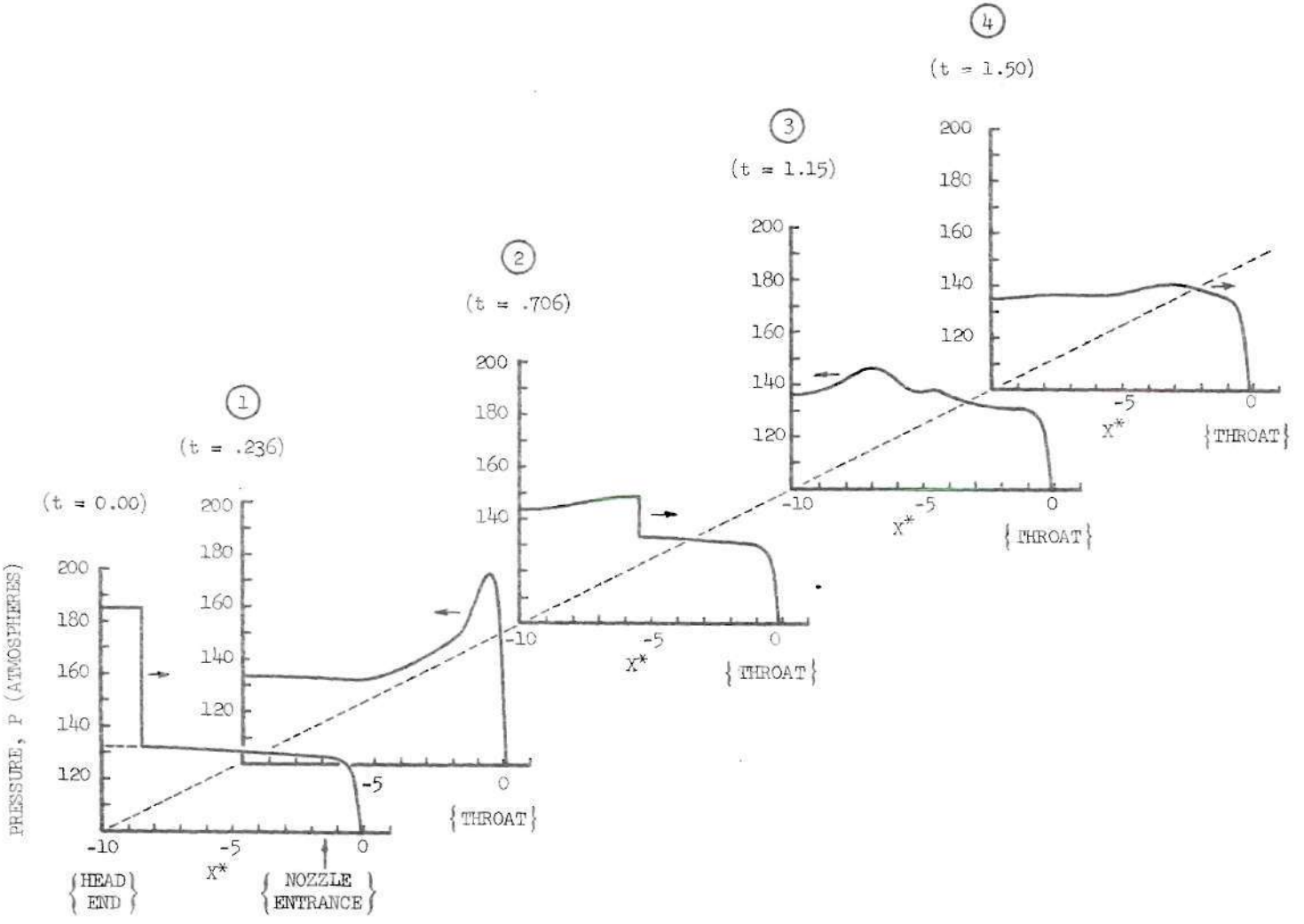

Figure 16. Pressure Distributions in Rocket Engine Flow Field of Case (1) as the Result of a Forty Percent Amplitude Shock Wave Disturbance

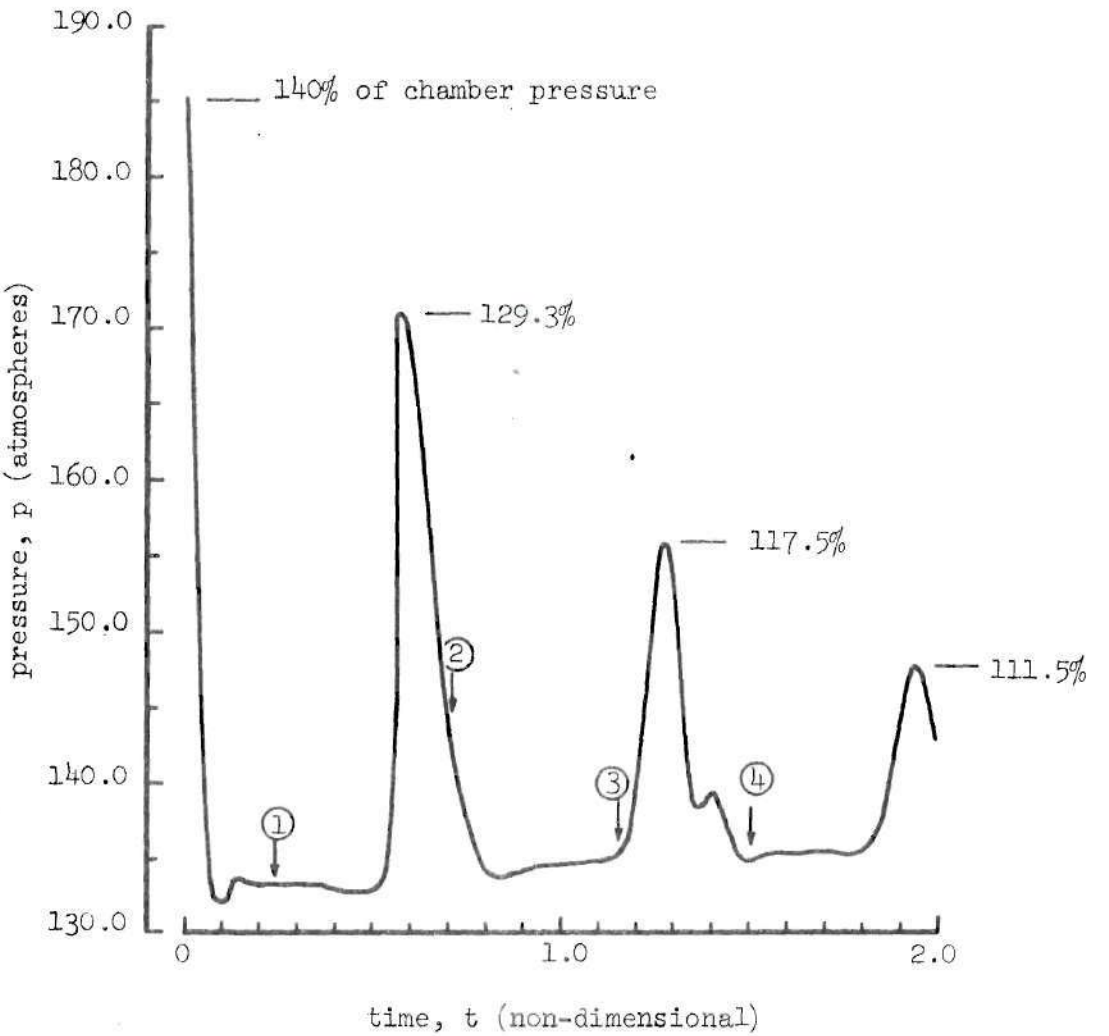

Figure 17. Pressure-Time History at the Head End of the Combustion Chamber as the Result of a Forty Percent Amplitude Shock Wave Disturbance on the Steady State Flow Field of Case (1)

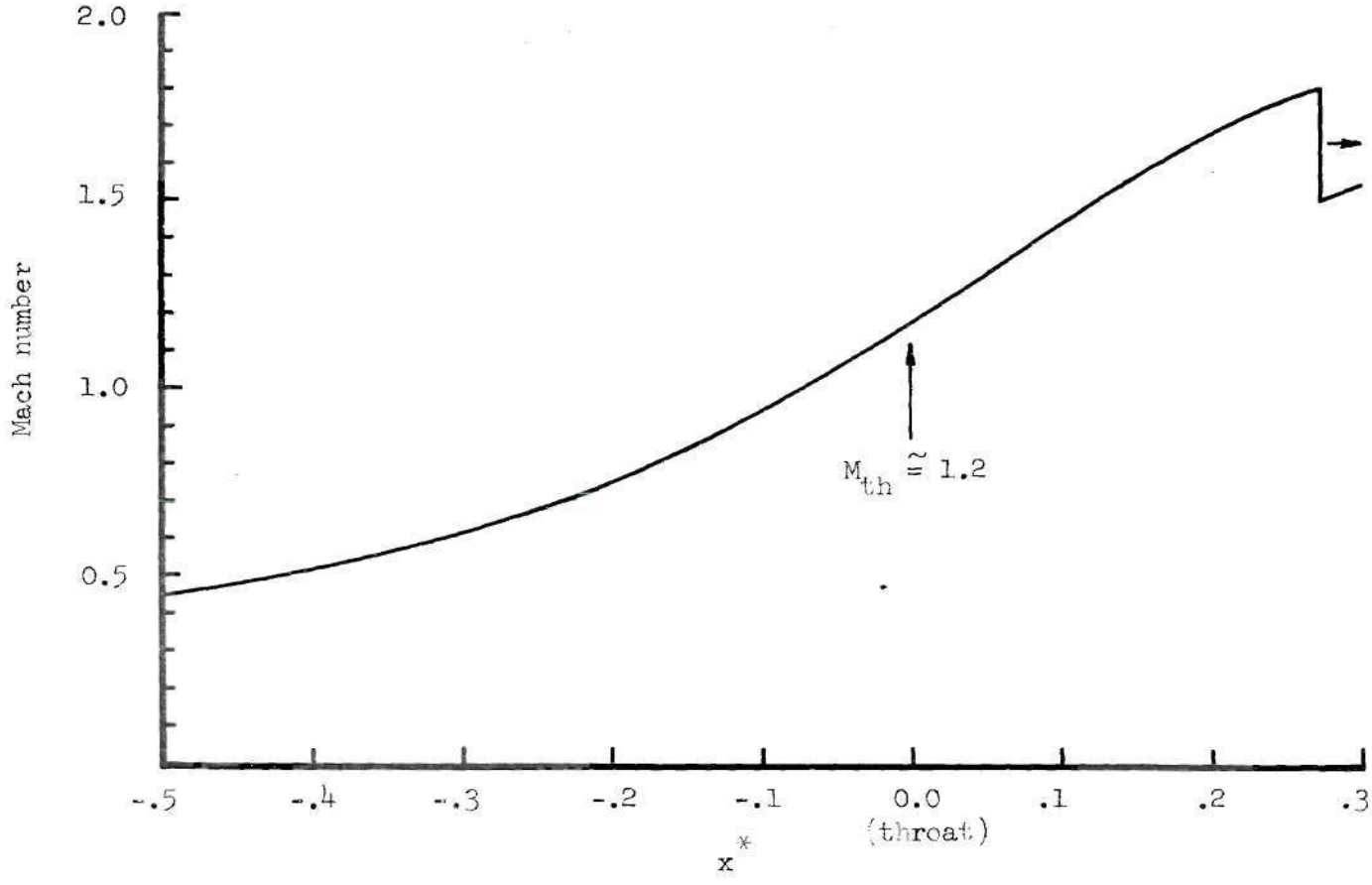

Figure 18. Instantaneous Mach Number Distribution in Throat Region for Time Point ① Indicated in Figure 16

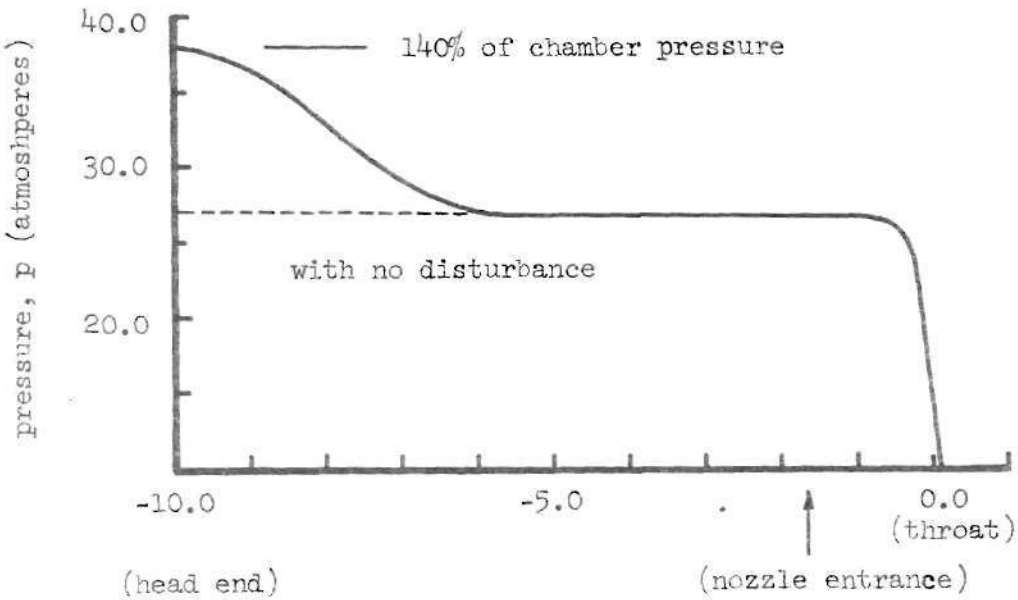

Figure 19. Continuous Type Disturbance Added to the Steady State Flow Field of Case (2)

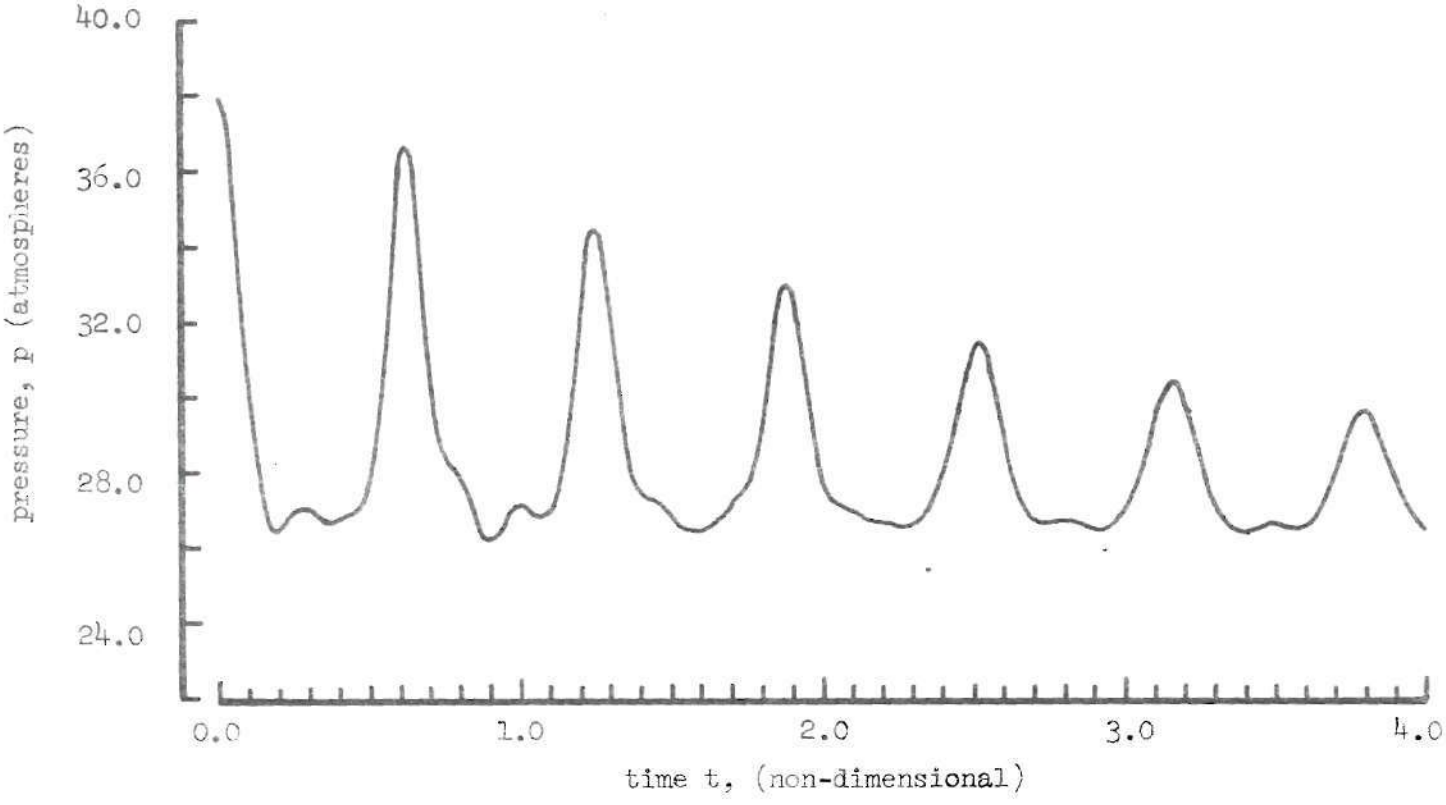

Figure 20. Pressure-Time History at the Head End of the Combustion Chamber as the Result of a Forty Percent Amplitude Continuous Disturbance Added to the Steady State Flow Field of Case (2)

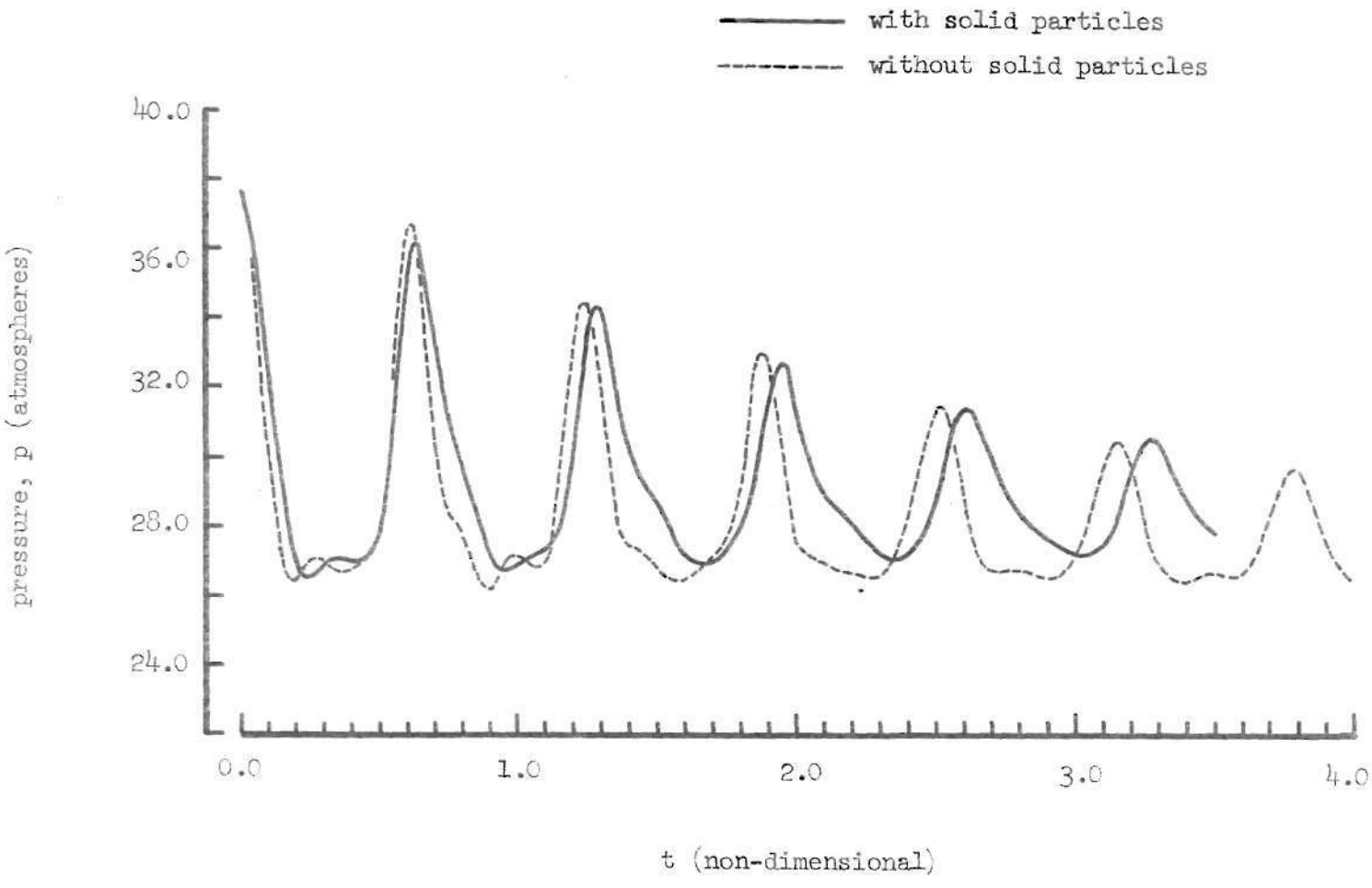

Figure 21. Comparison (With and Without 10μ Particles, Ten Percent Weight Loading) of the Pressure-Time History at the Head End of the Combustion Chamber as the Result of a Forty Percent Amplitude Continuous Disturbance, Case (2)

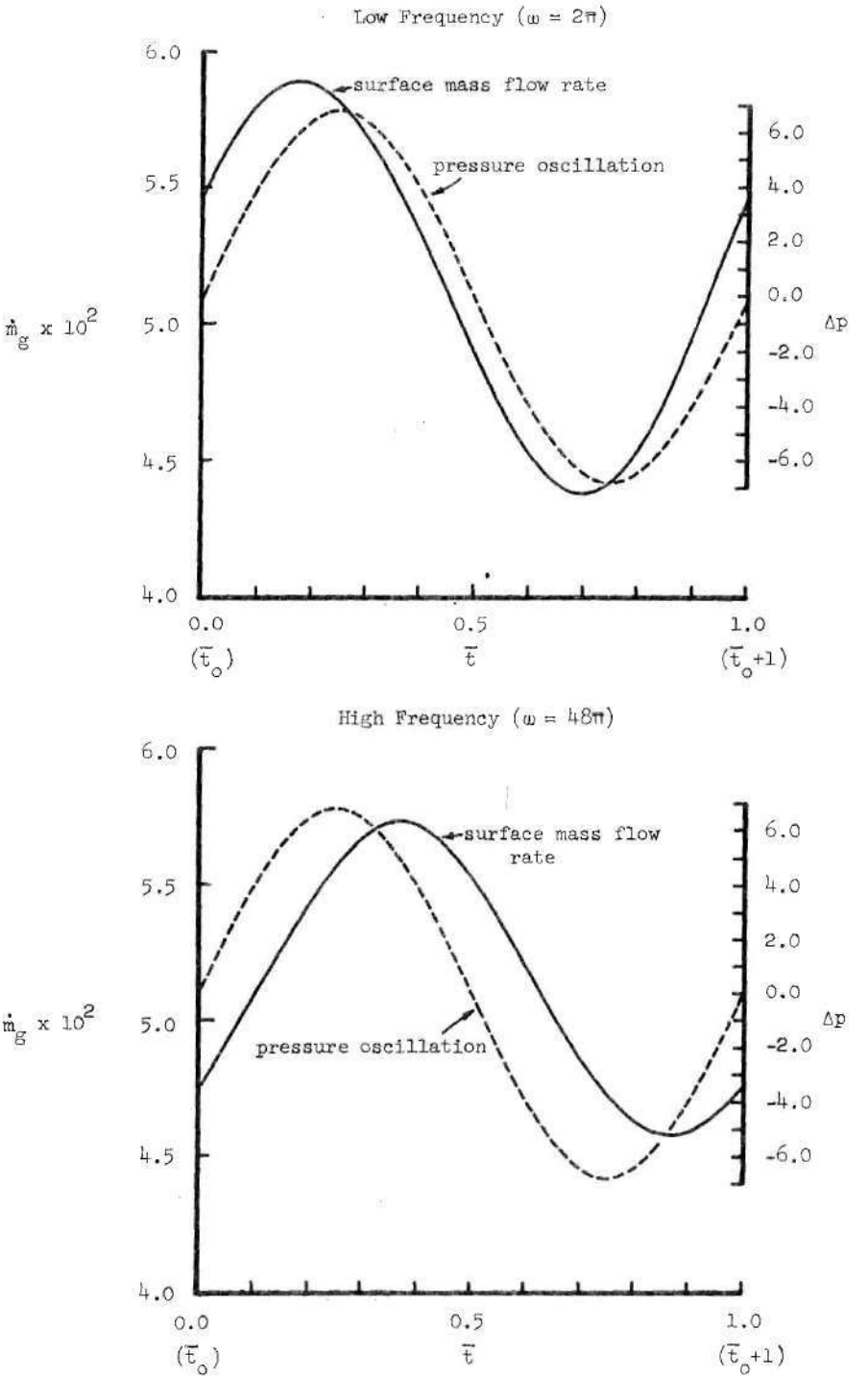

Figure 22. Propellant Surface Mass Flow Rate Due to a Ten Percent Amplitude Sinusoidal Pressure Oscillation at a Low Frequency ($\omega = 2\pi$) and a High Frequency ($\omega = 48\pi$)

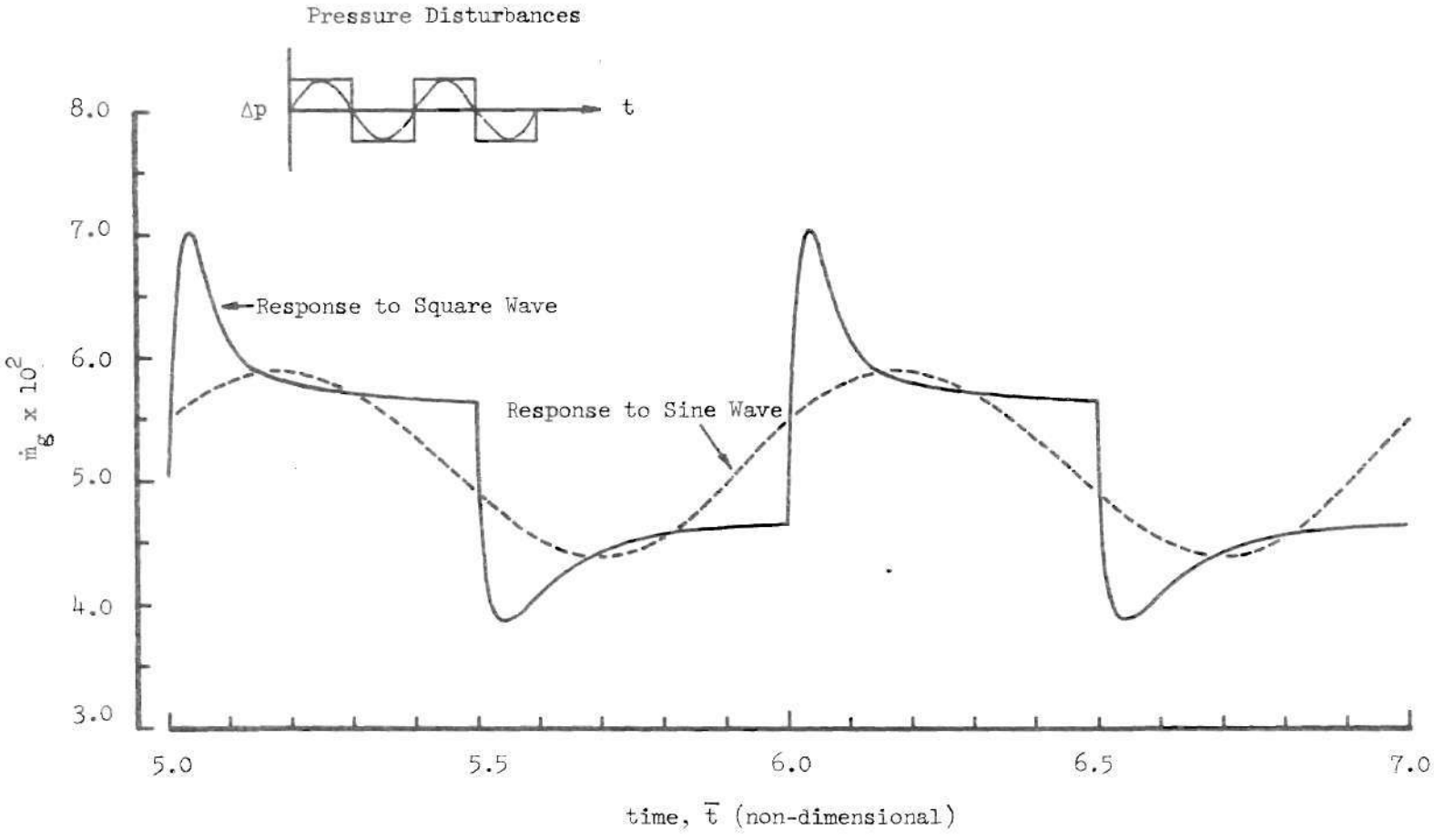

Figure 23. Comparison of Combustion Response to a Ten Percent Amplitude Square Wave Pressure Oscillation and a Sine Wave Pressure Oscillation at $\omega = 2\pi$

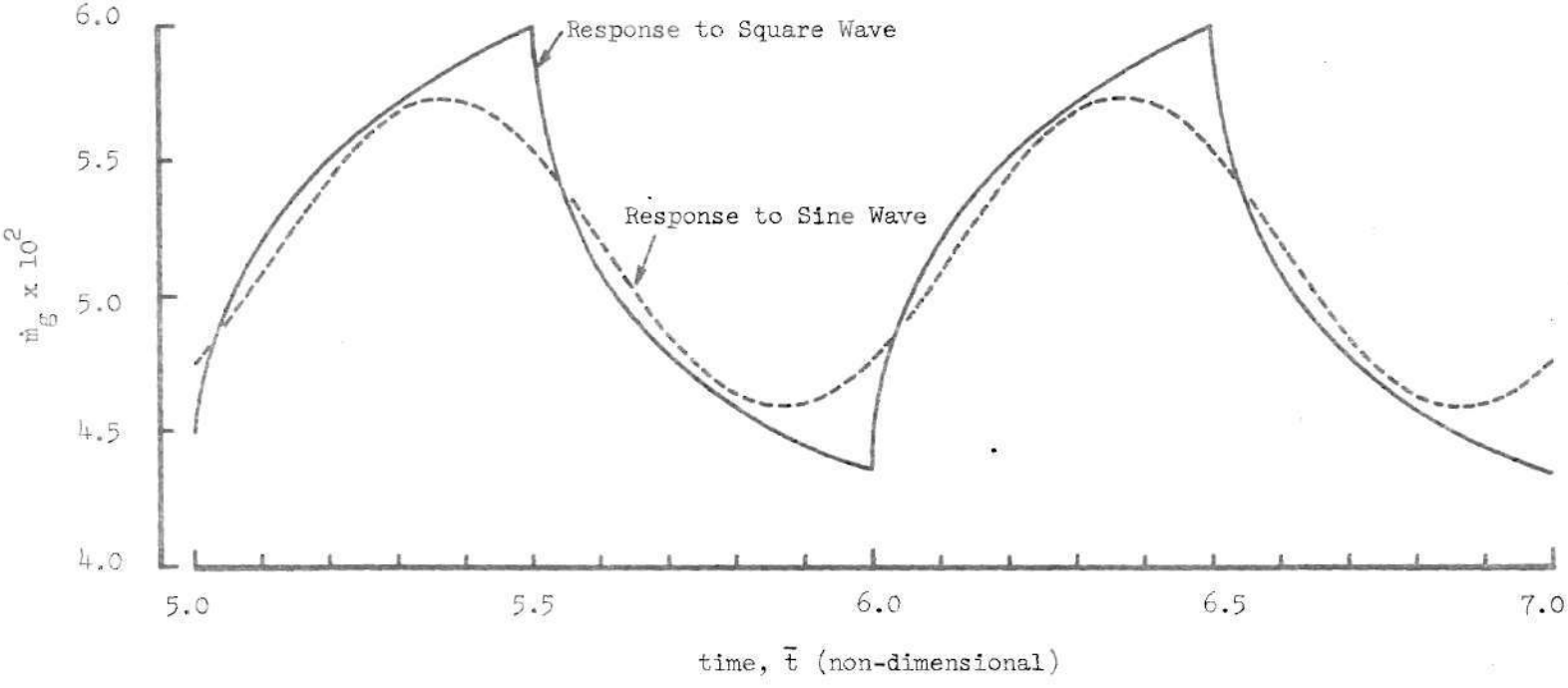

Figure 24. Comparison of Combustion Response to a Ten Percent Amplitude Square Wave Pressure Oscillation and a Sine Wave Pressure Oscillation at $\omega = 48\pi$

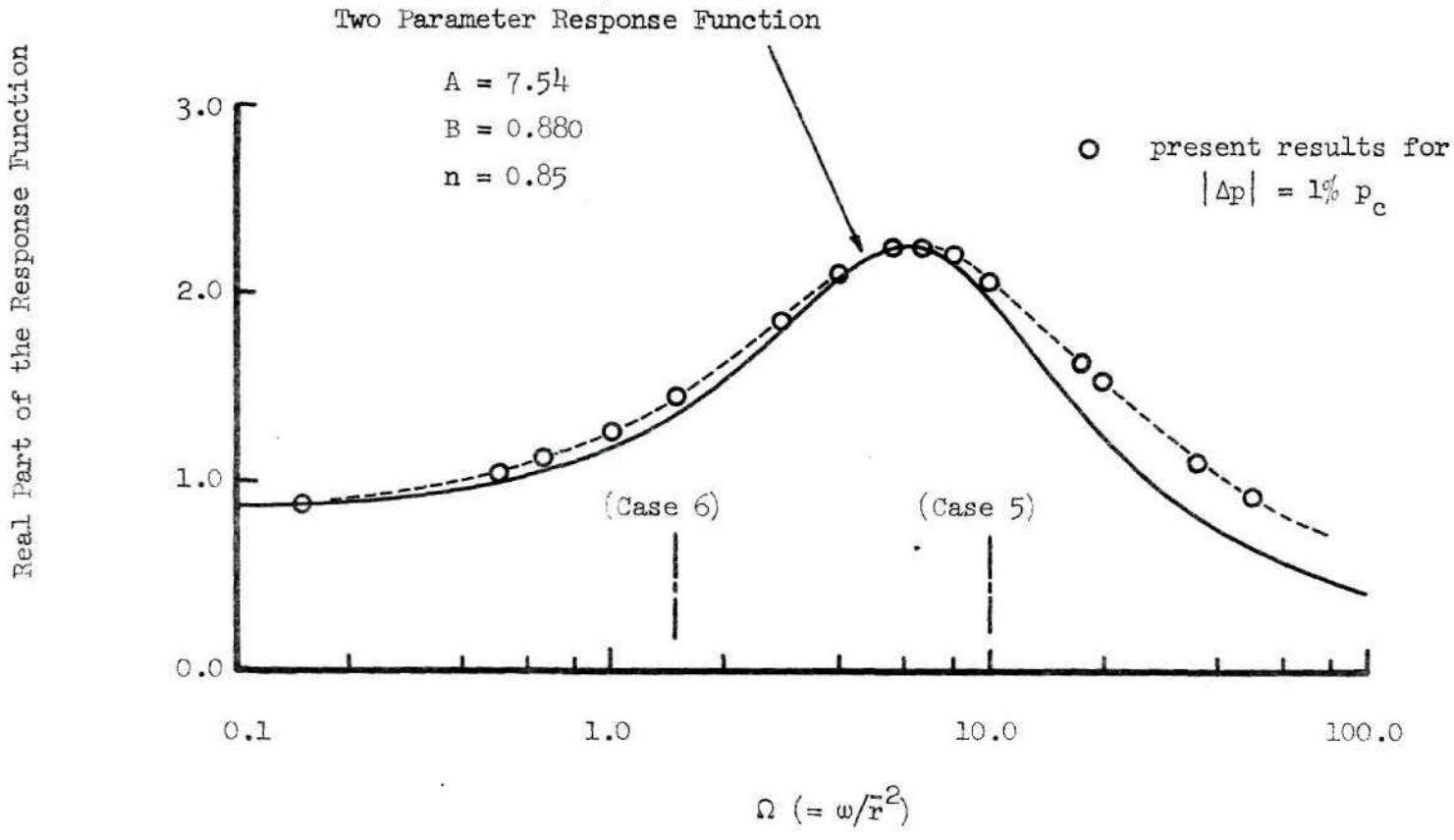

Figure 25. Combustion Response as a Function of Frequency for the Propellant System in Case (5) and (6) [$Q_s^* = -100$ cal/gm]

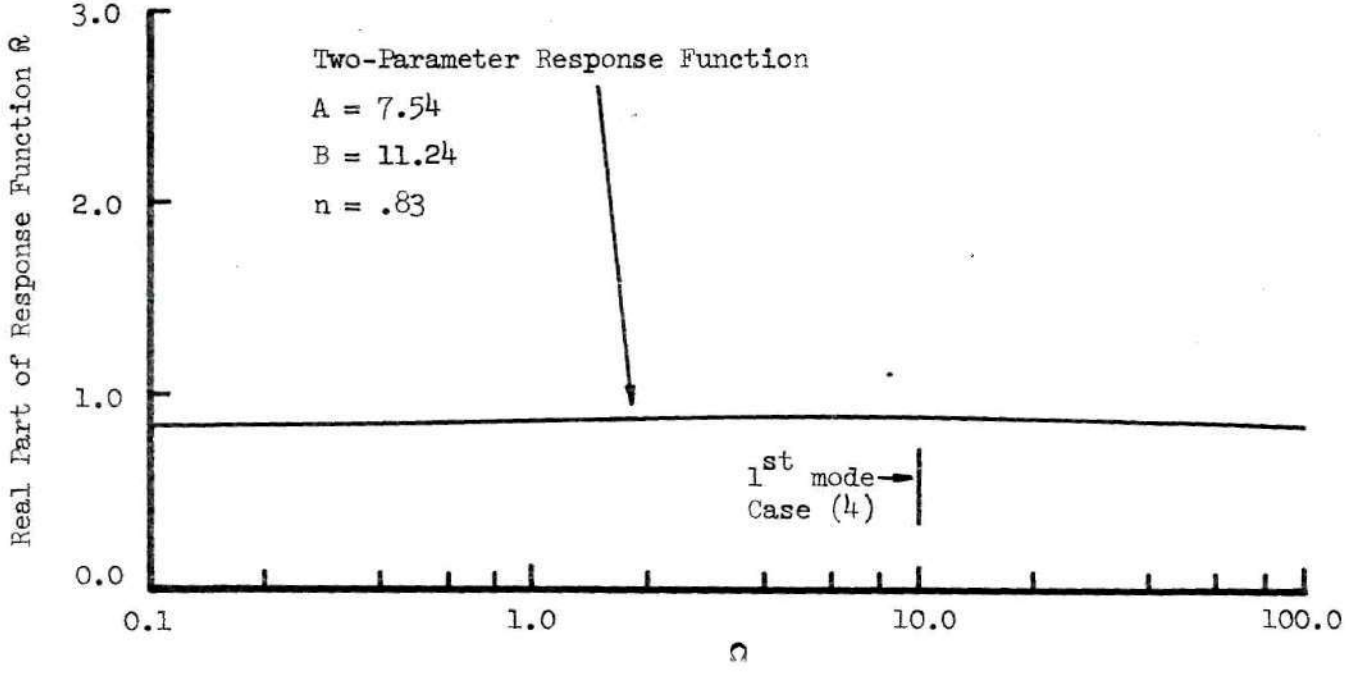

Figure 26. Combustion Response as a Function of Frequency for the Propellant System in Case (4) [$Q_s^* = +585$ cal/gm]

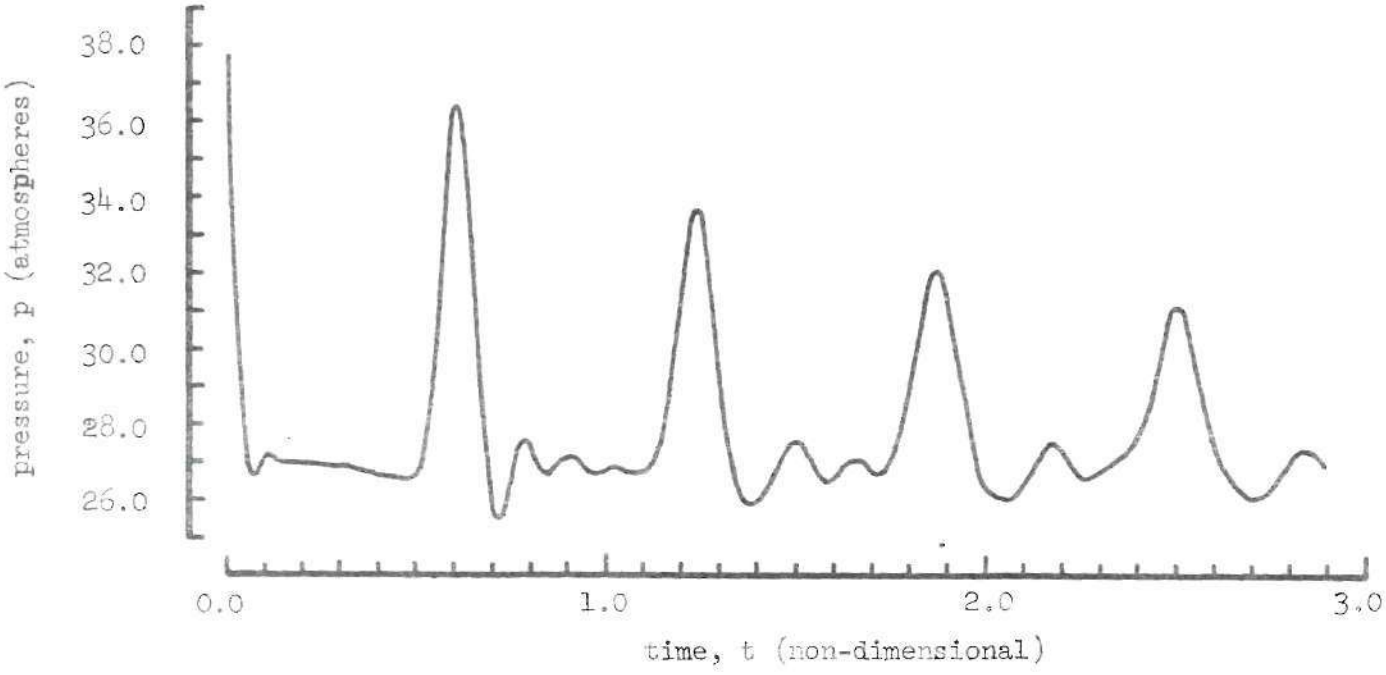

Figure 27. Pressure-Time History at the Head End of the Combustion Chamber as the Result of a Forty Percent Amplitude Shock Wave Disturbance on the Steady State Flow Field of Case (4)

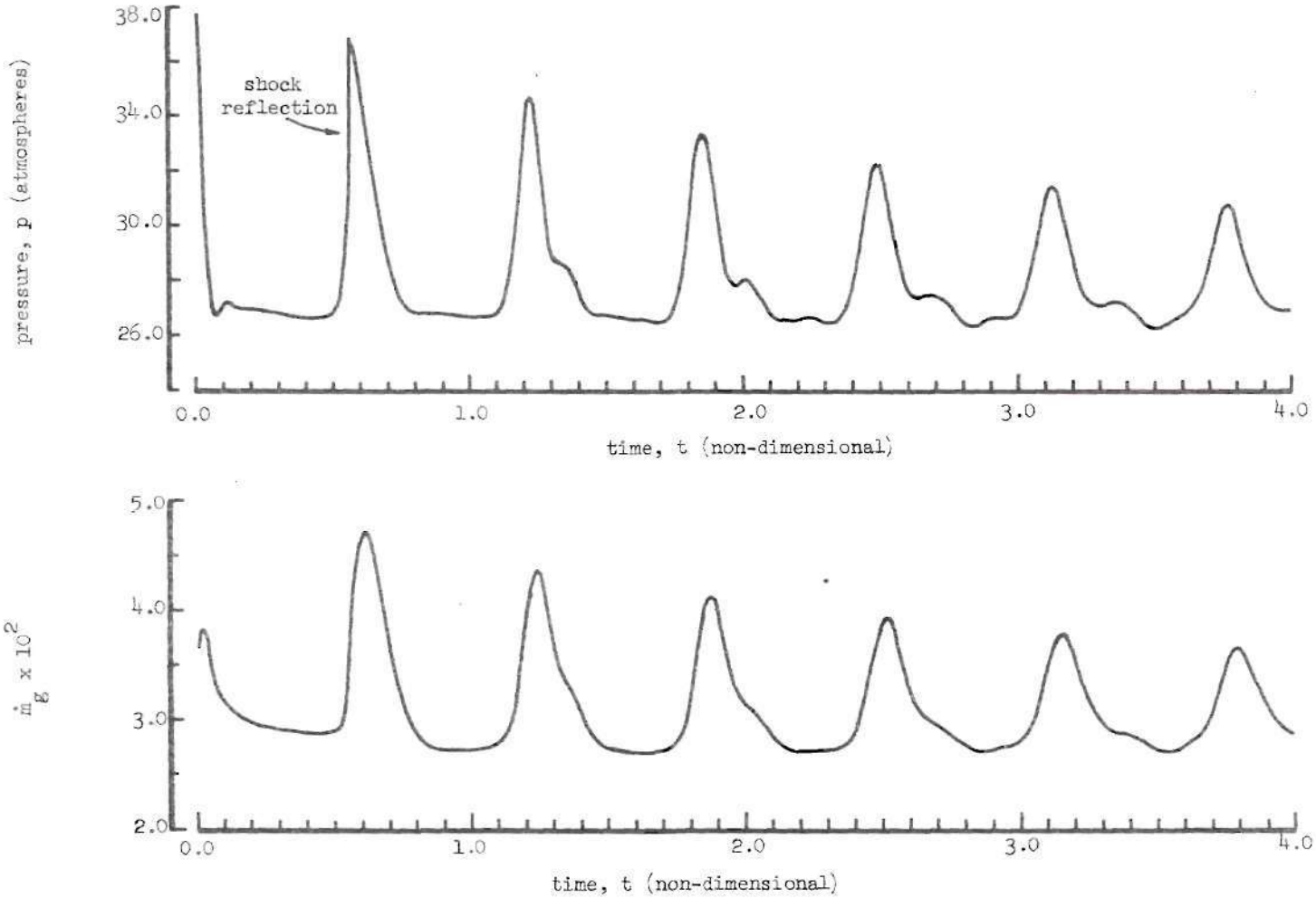

Figure 28. Time History of Pressure and Propellant Mass Flow Rate at the Head End of the Combustion Chamber as the Result of a Forty Percent Amplitude Shock Wave Disturbance on Case (5)

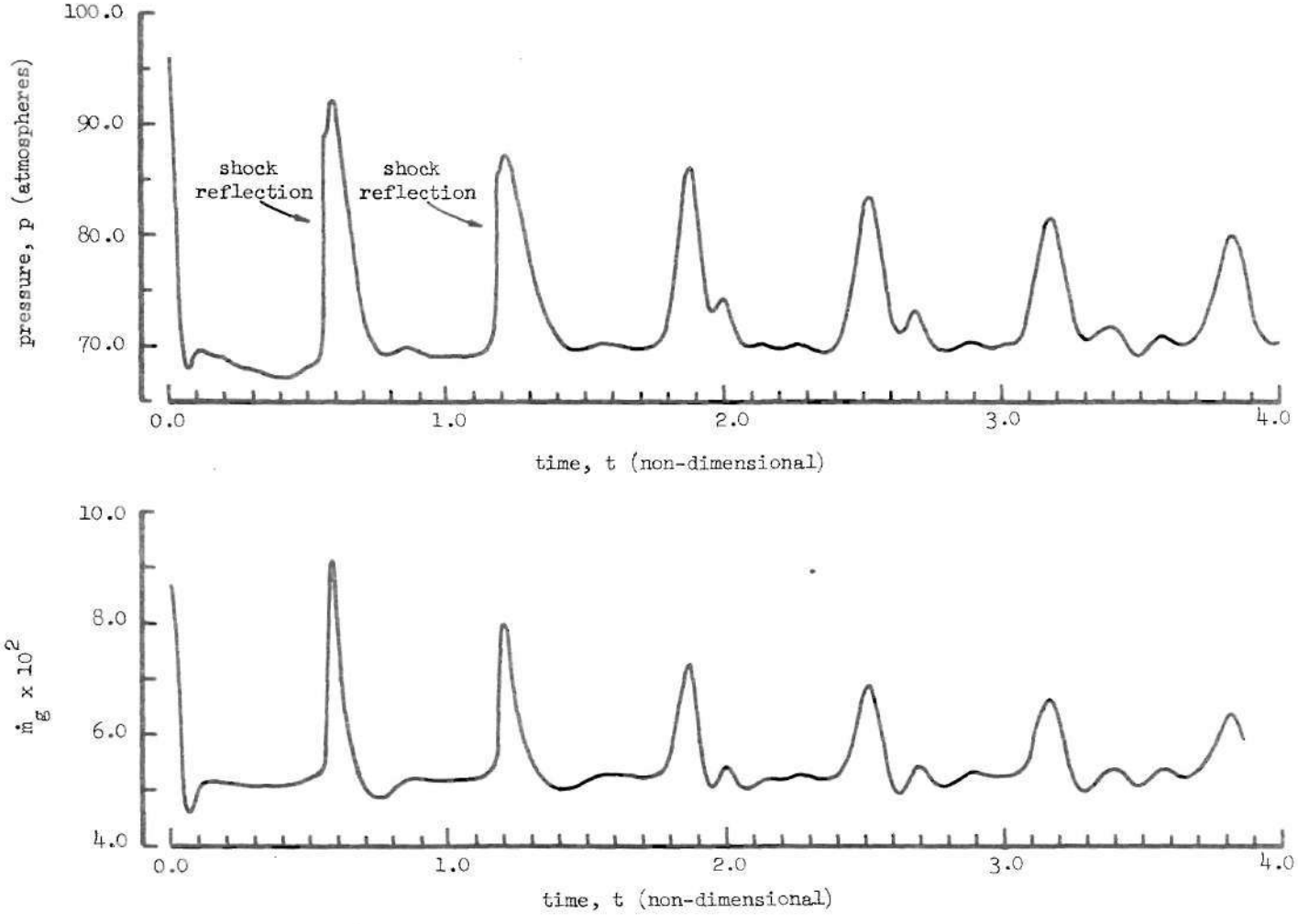

Figure 29. Time Hisotry of Pressure and Propellant Mass Flow Rate at the Head End of the Combustion Chamber as the Result of a Forty Percent Amplitude Shock Wave Disturbance on Case (6)

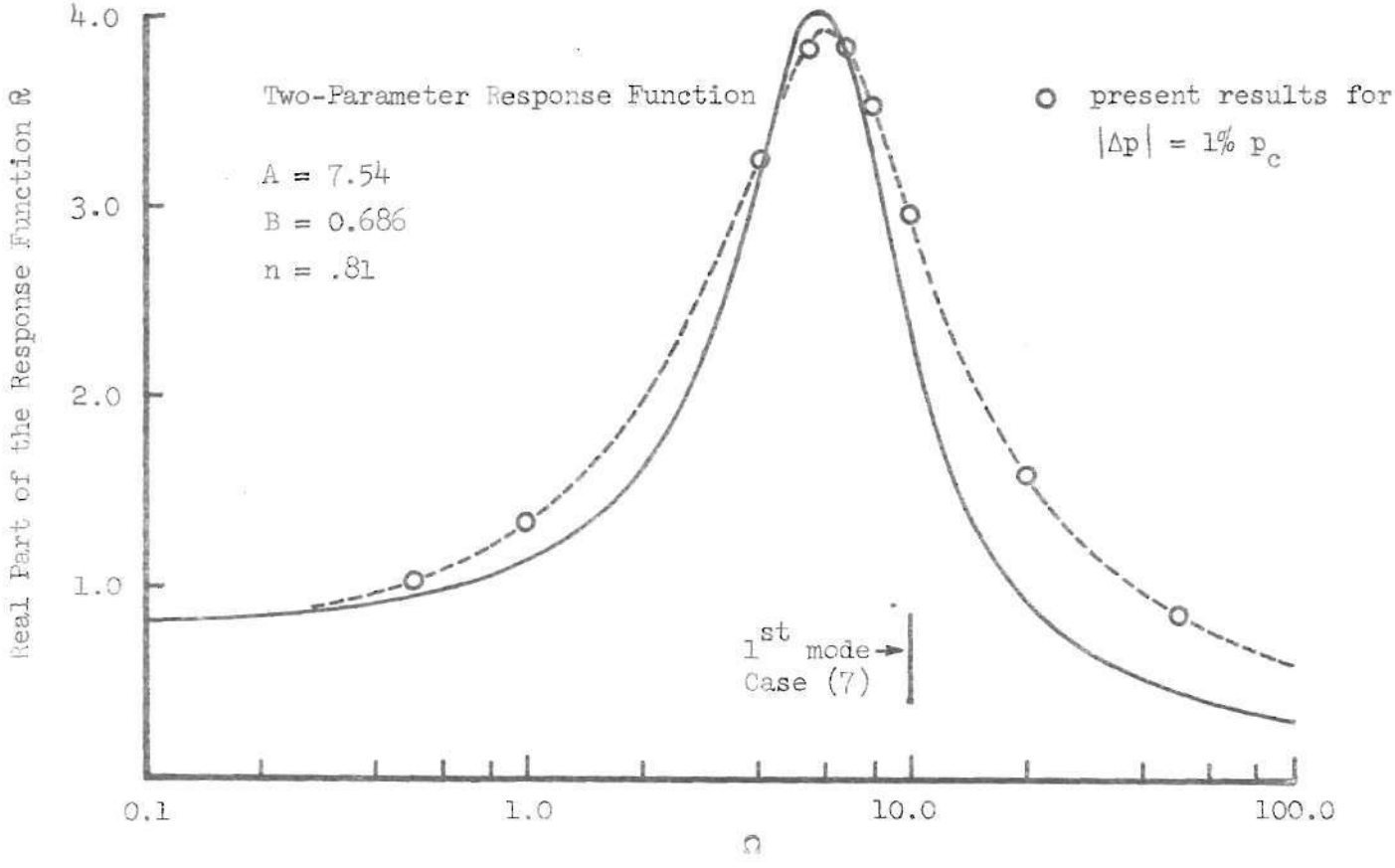

Figure 30. Combustion Response as a Function of Frequency for the Propellant System in Case (7) [$Q_s^* = -115$ cal/gm]

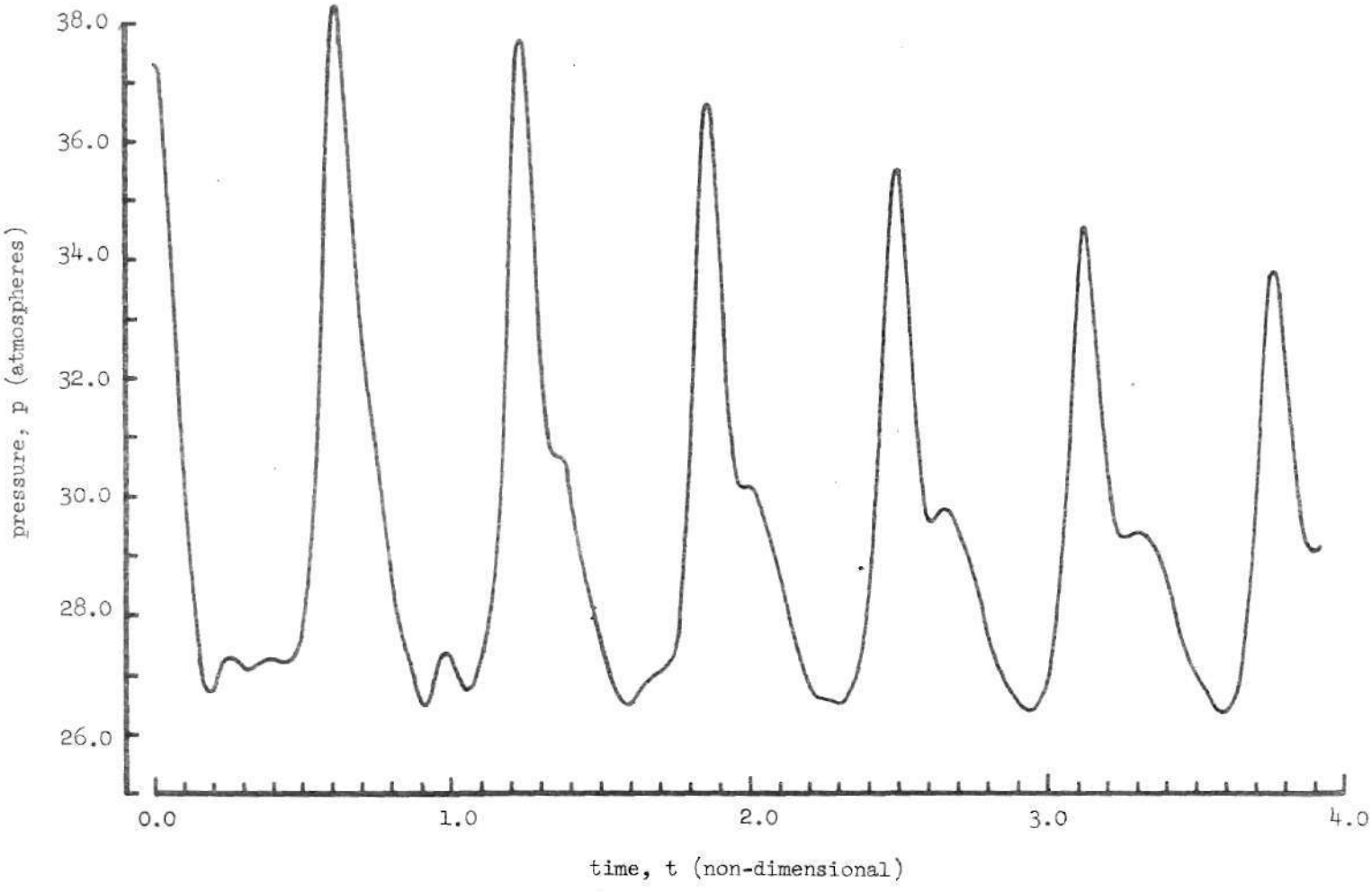

Figure 31. Pressure-Time History at the Head End of the Combustion Chamber as the Result of a Forty Percent Amplitude Continuous Disturbance on the Steady State Flow Field of Case (7)

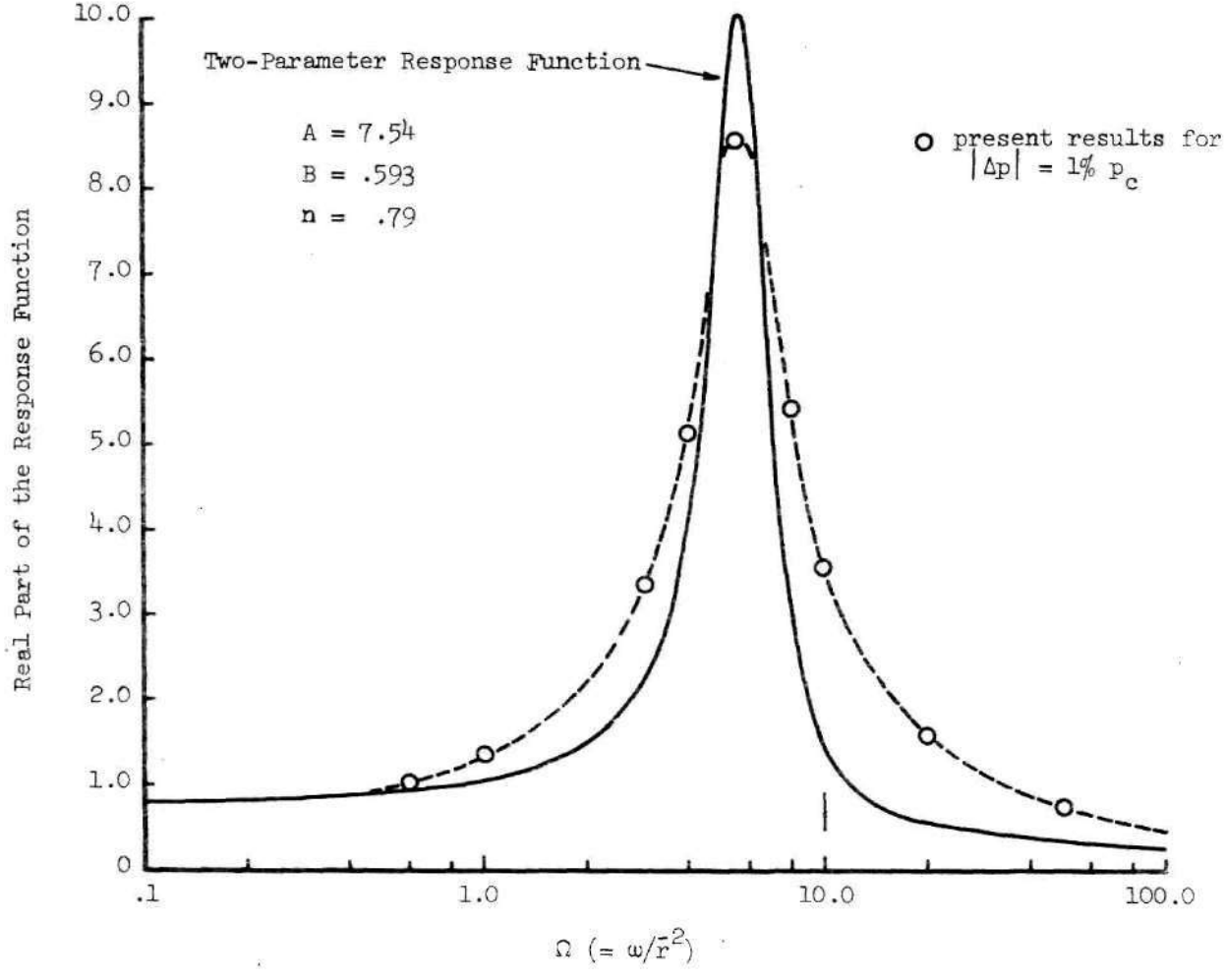

Figure 32. Combustion Response as a Function of Frequency for the Propellant System in Case (8) [$Q_s^* = -122$ cal/gm]

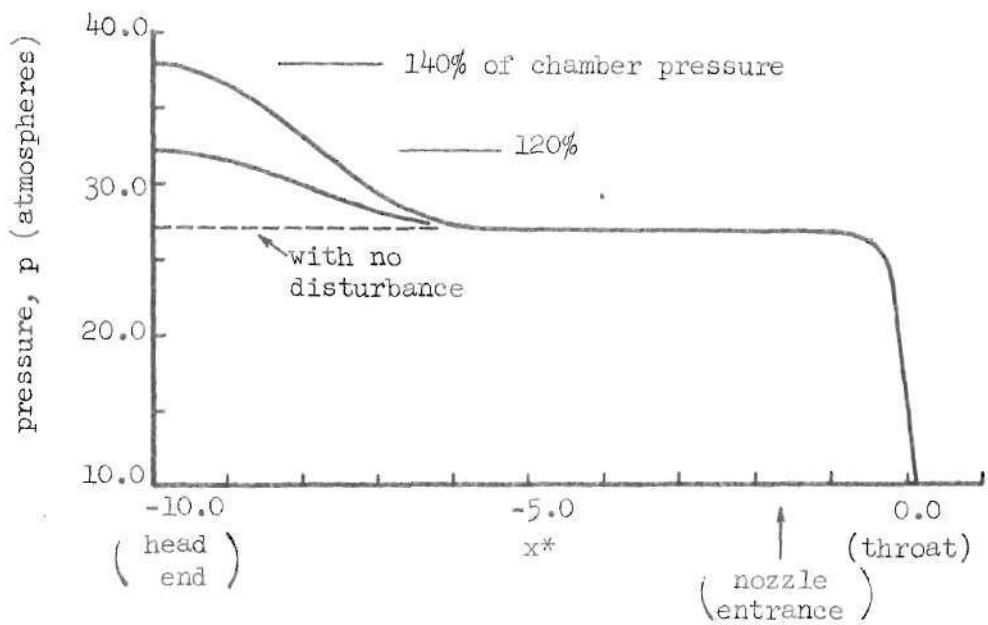

Figure 33. Continuous Type Disturbances Added to the Steady State Flow Field of Case (8)

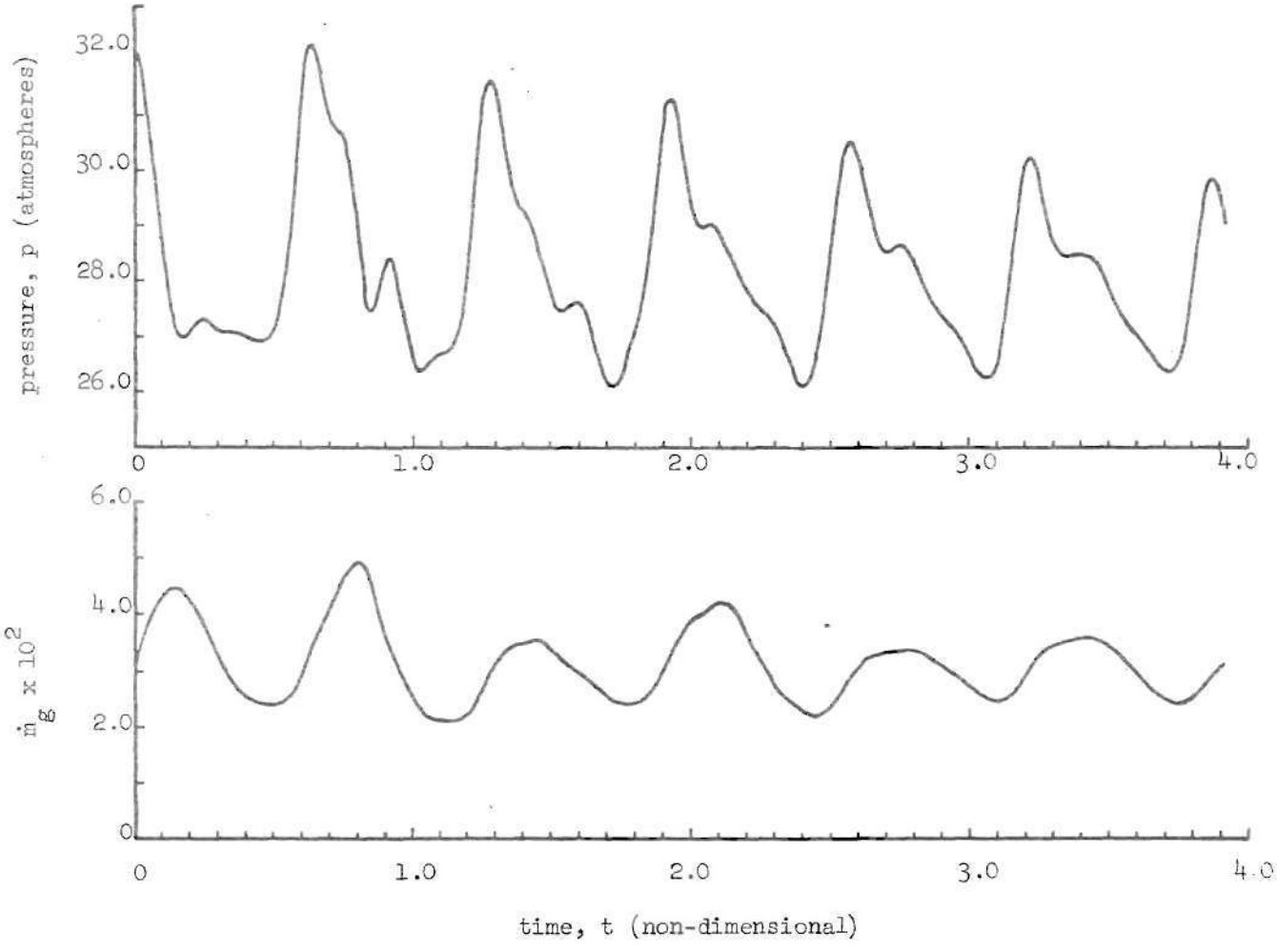

Figure 34. Time History of Pressure and Propellant Mass Flow Rate at the Head End of the Combustion Chamber as the Result of a Twenty Percent Amplitude Continuous Disturbance on Case (8)

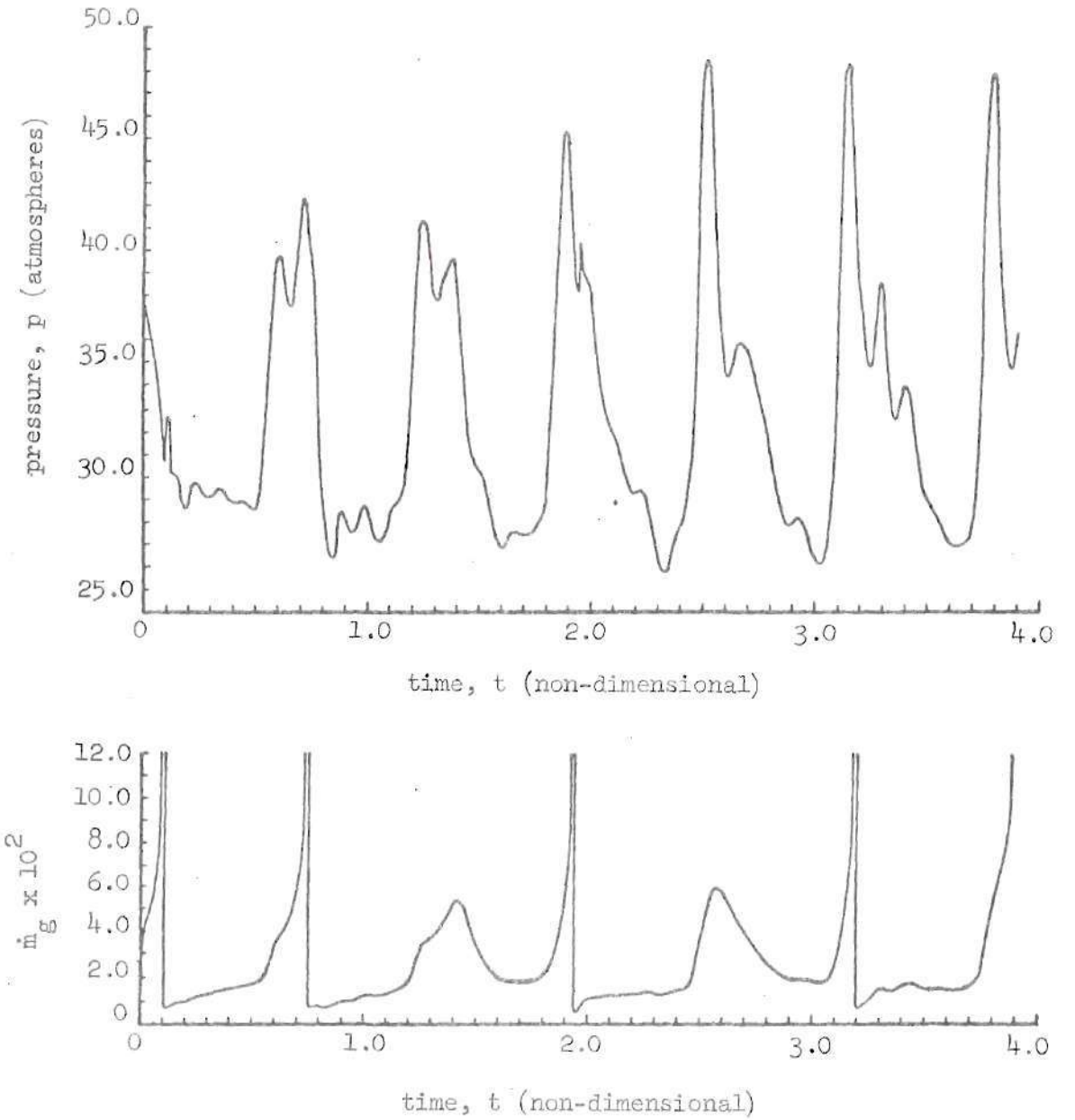

Figure 35. Time History of Pressure and Propellant Mass Flow Rate at the Head End of the Combustion Chamber as the Result of a Forty Percent Amplitude Continuous Disturbance on Case (8)

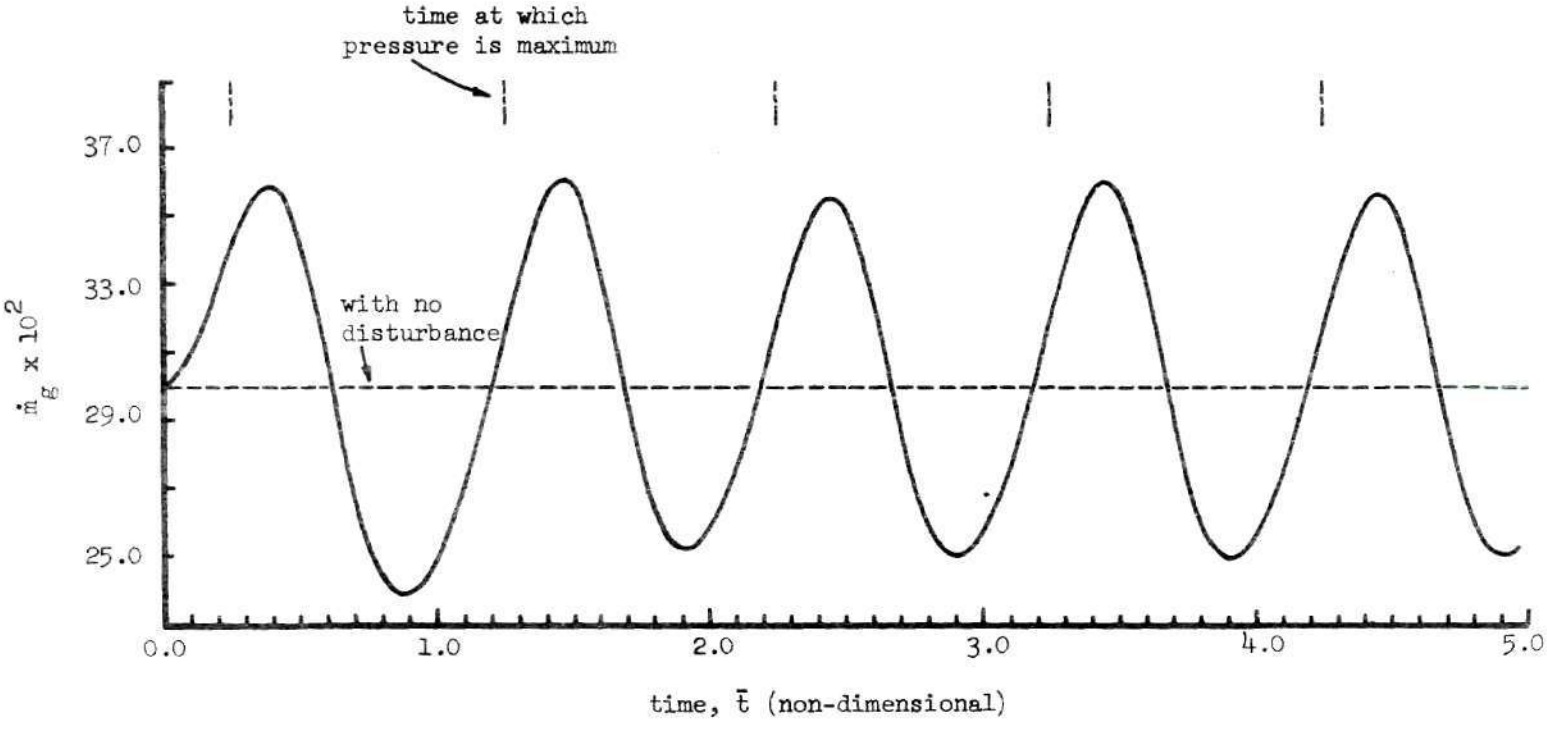

Figure 36. Combustion Response to a Five Percent Amplitude Sinusoidal Pressure Oscillation at $\Omega = 10.0$ for the Propellant System in Case (8)

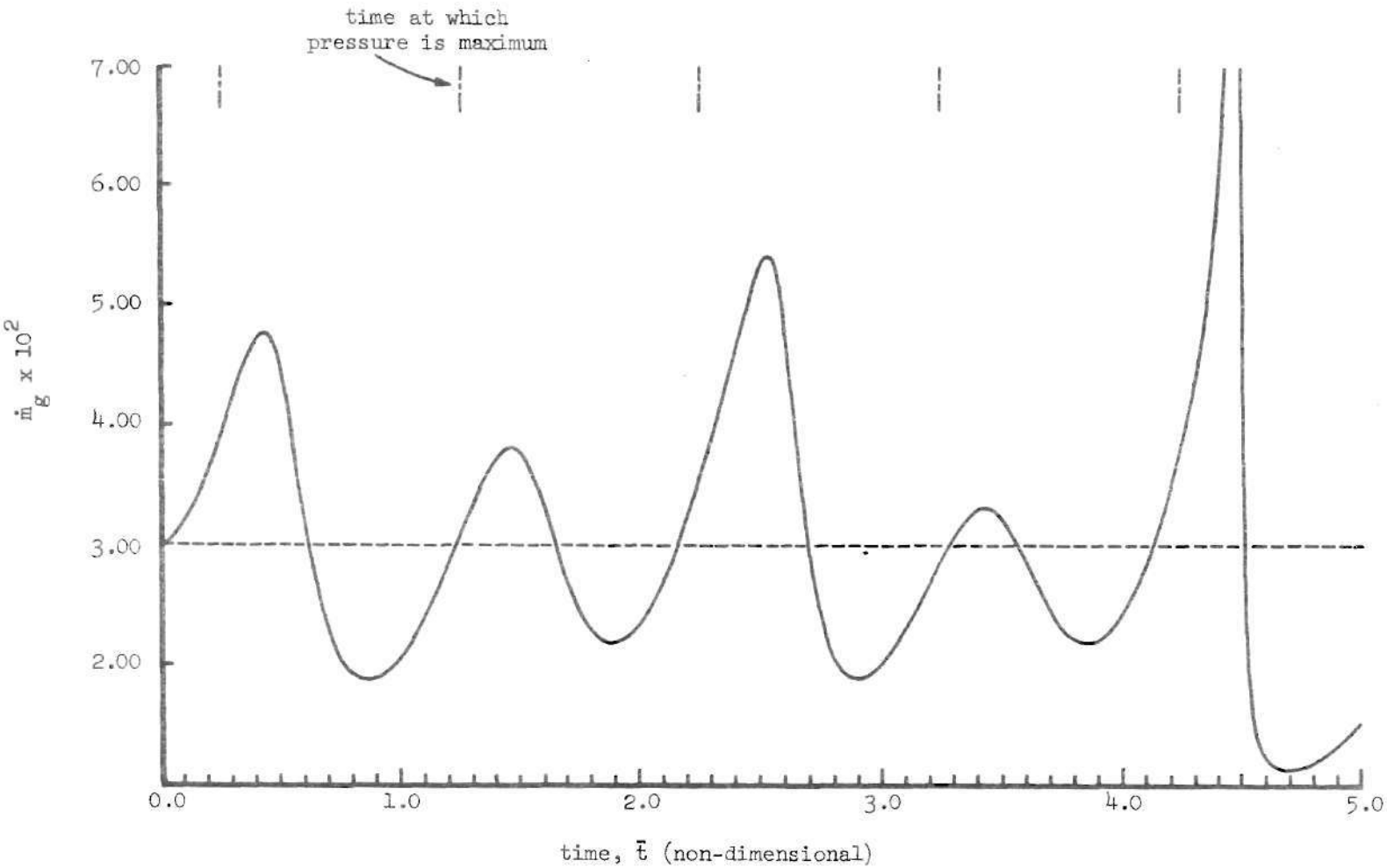

Figure 37. Combustion Response to a Ten Percent Amplitude Sinusoidal Pressure Oscillation at $\Omega = 10.0$ for the Propellant System in Case (8)

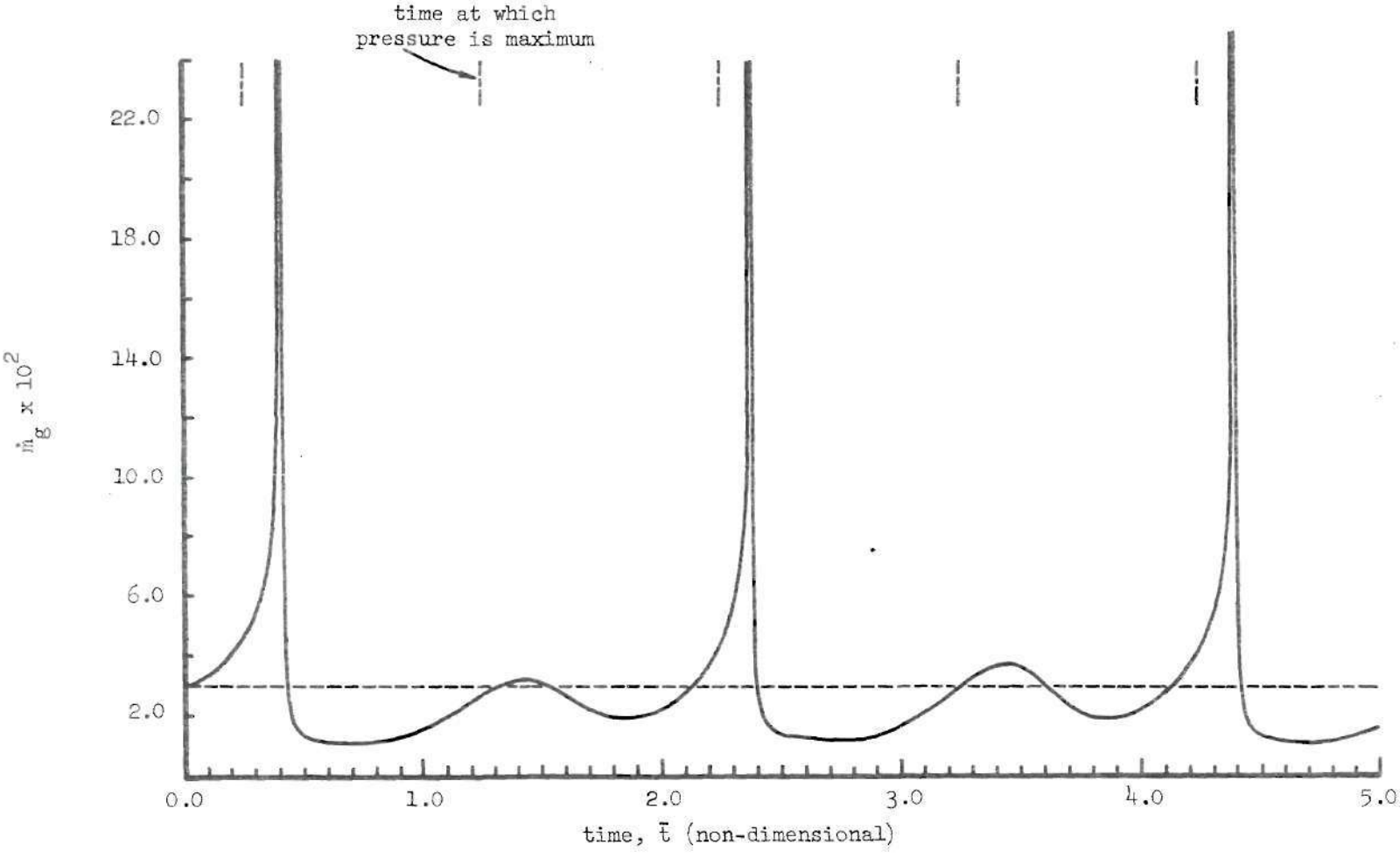

Figure 38. Combustion Response to a Fifteen Percent Amplitude Sinusoidal Pressure Oscillation at $\Omega = 10.0$ for the Propellant System in Case (8)

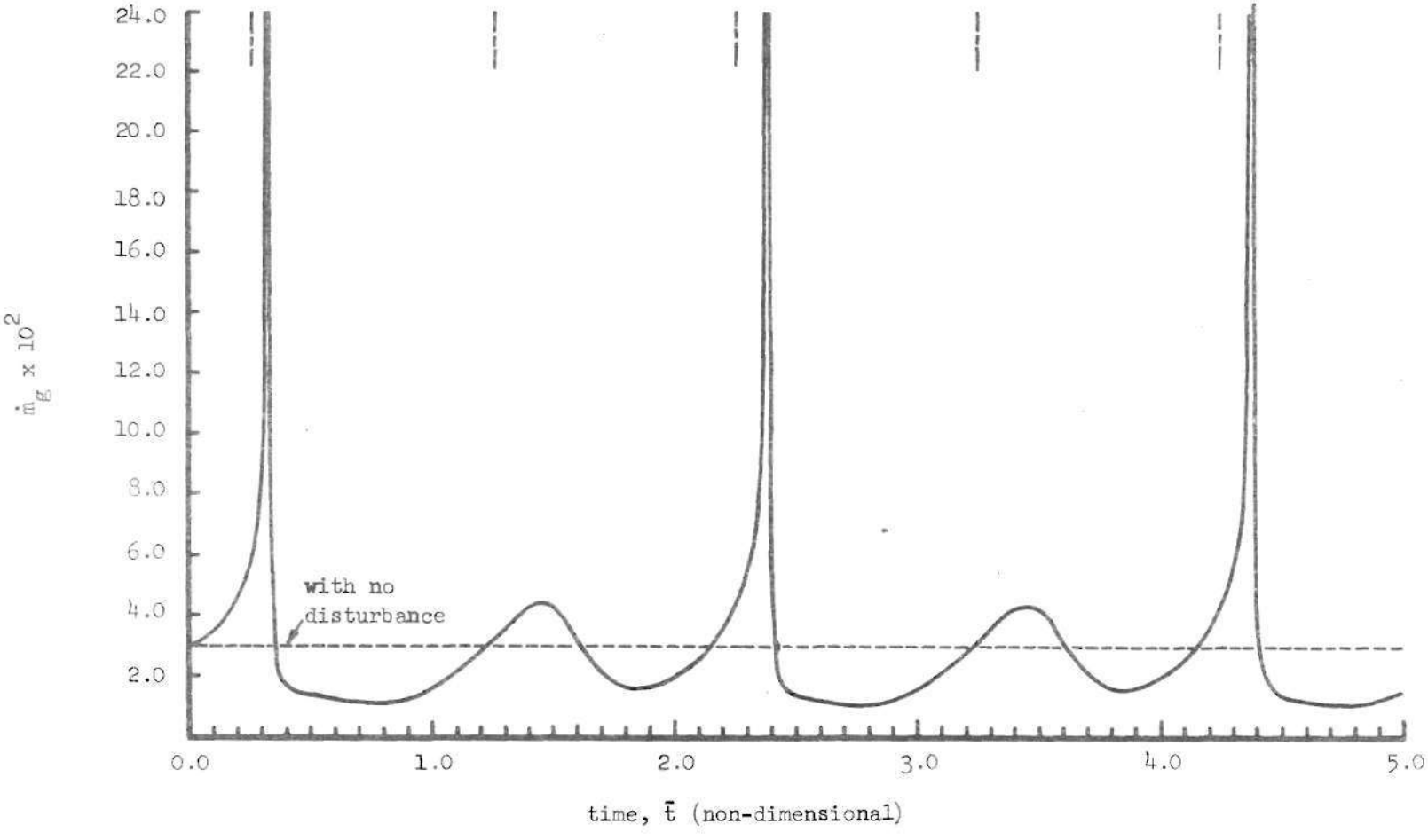

Figure 39. Combustion Response to a Twenty Percent Amplitude Sinusoidal Pressure Oscillation at $\Omega = 10.0$ for the Propellant System in Case (8)

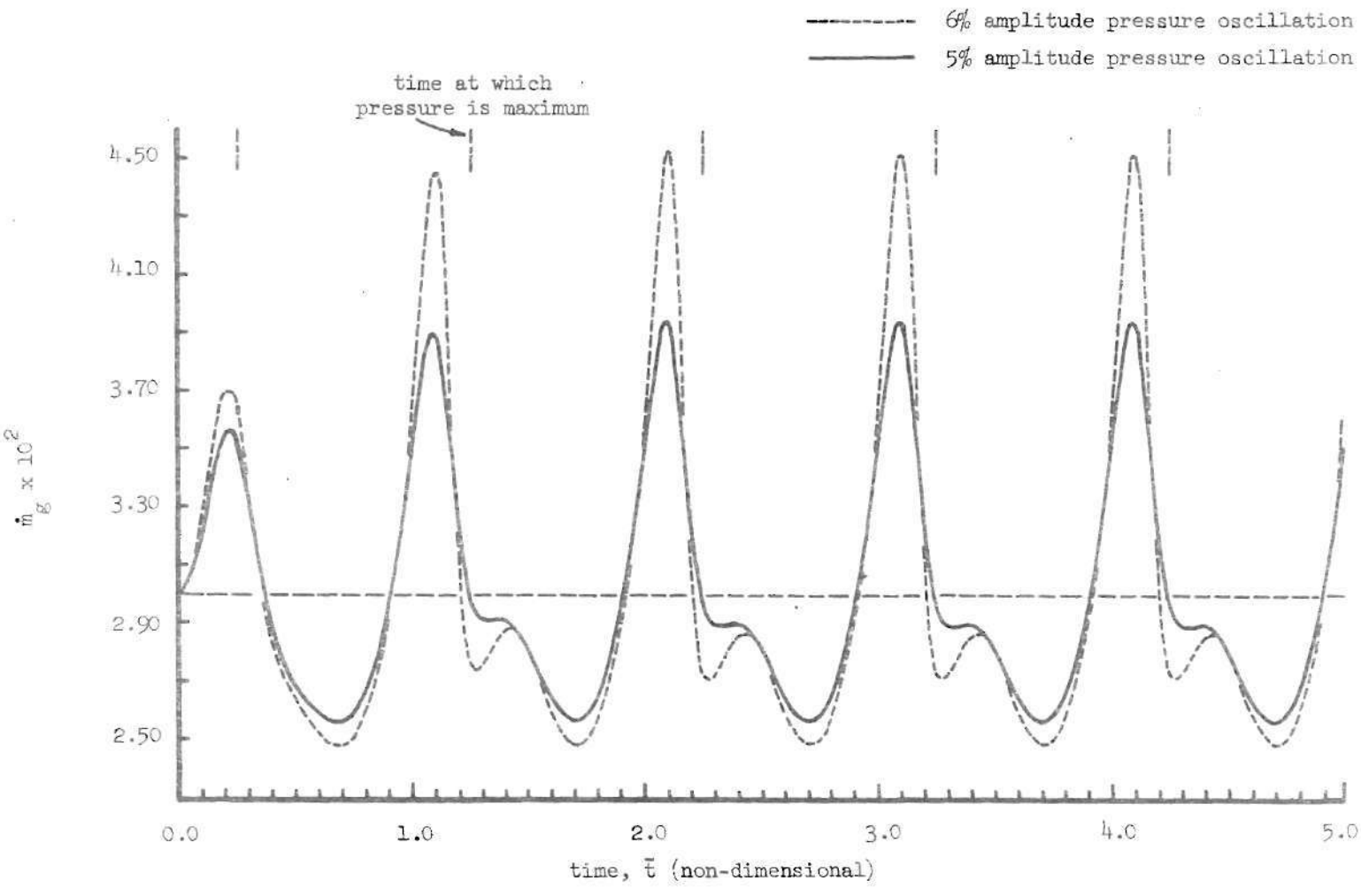

Figure 40. Combustion Response to a Five Percent and a Six Percent Amplitude Sinusoidal Pressure Oscillation at $\Omega = 3.0$ for the Propellant System in Case (8)

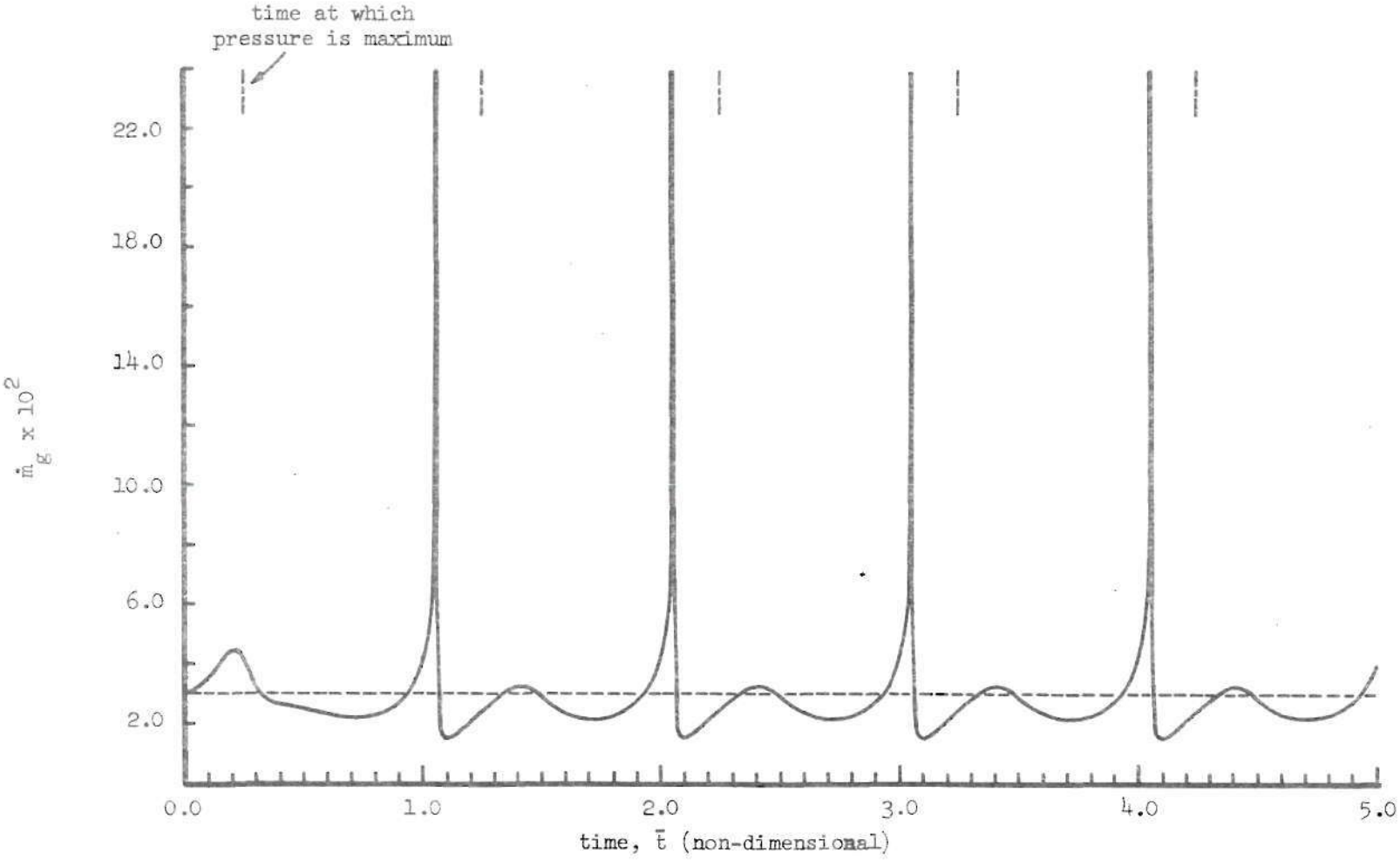

Figure 41. Combustion Response to a Ten Percent Amplitute Sinusoidal Pressure Oscillation at $\Omega = 3.0$ for the Propellant System in Case (8)

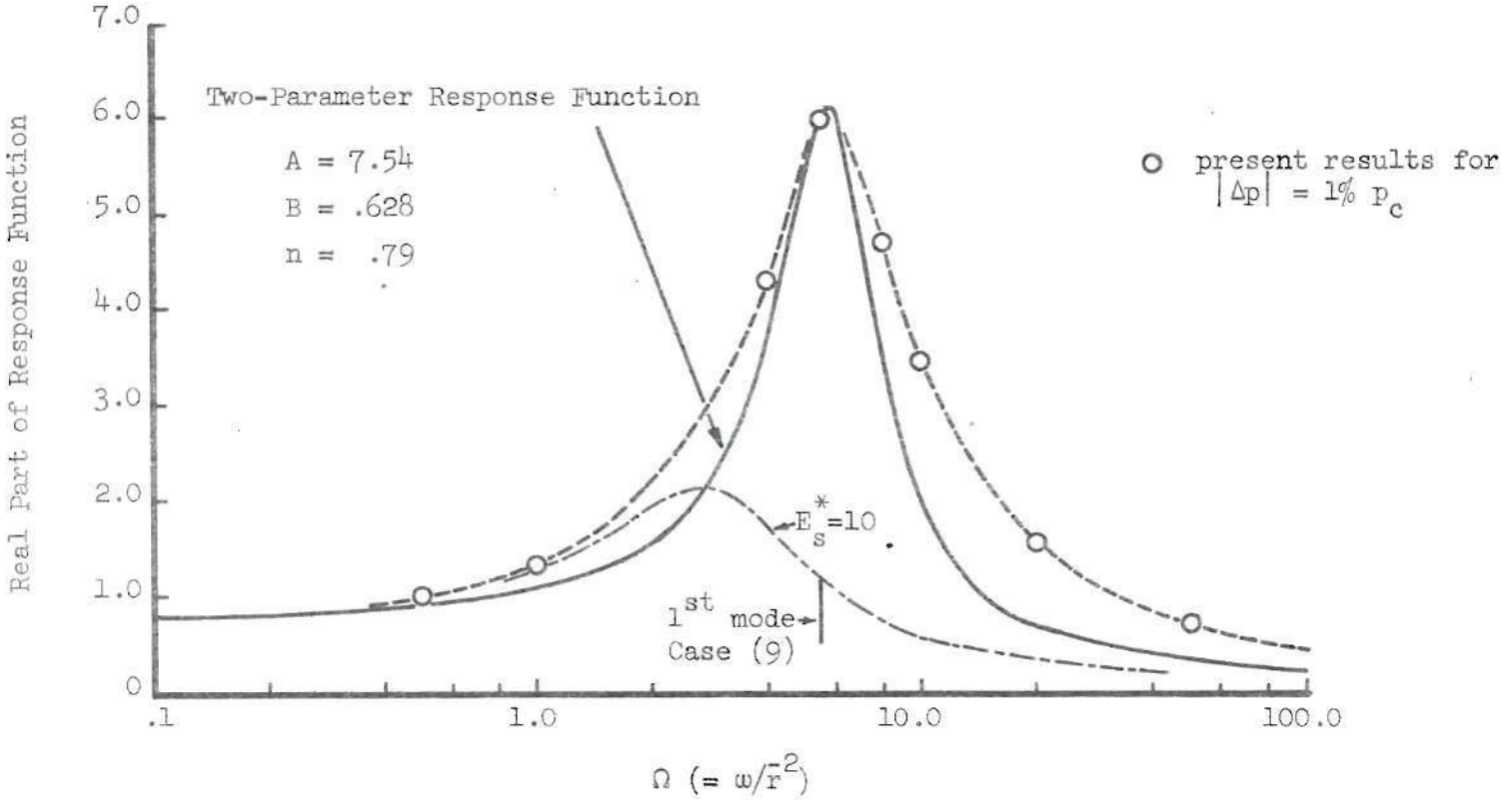

Figure 42. Combustion Response as a Function of Frequency for the Propellant System in Case (9) [Q_s^* = - 120 cal/cm]

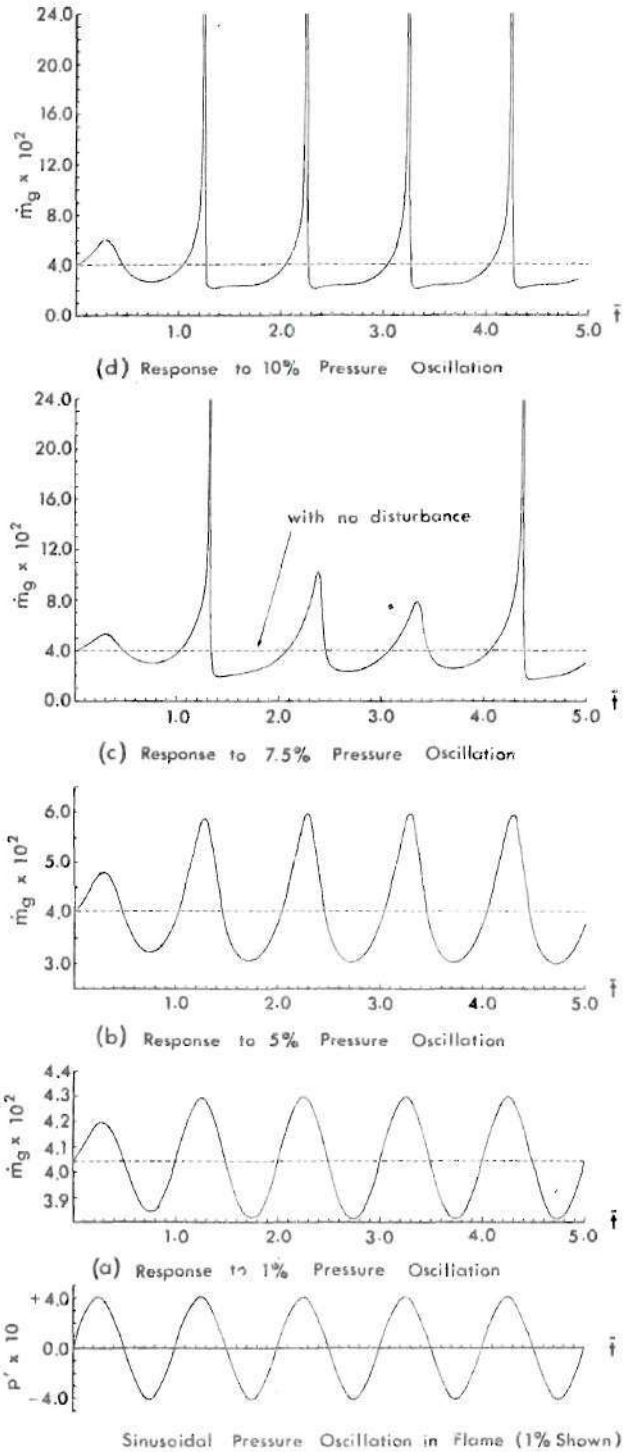

Figure 43. Combustion Response to Varying Amplitude Sinusoidal Pressure Oscillations at Ω = 5.5 for the Propellant System in Case (9)

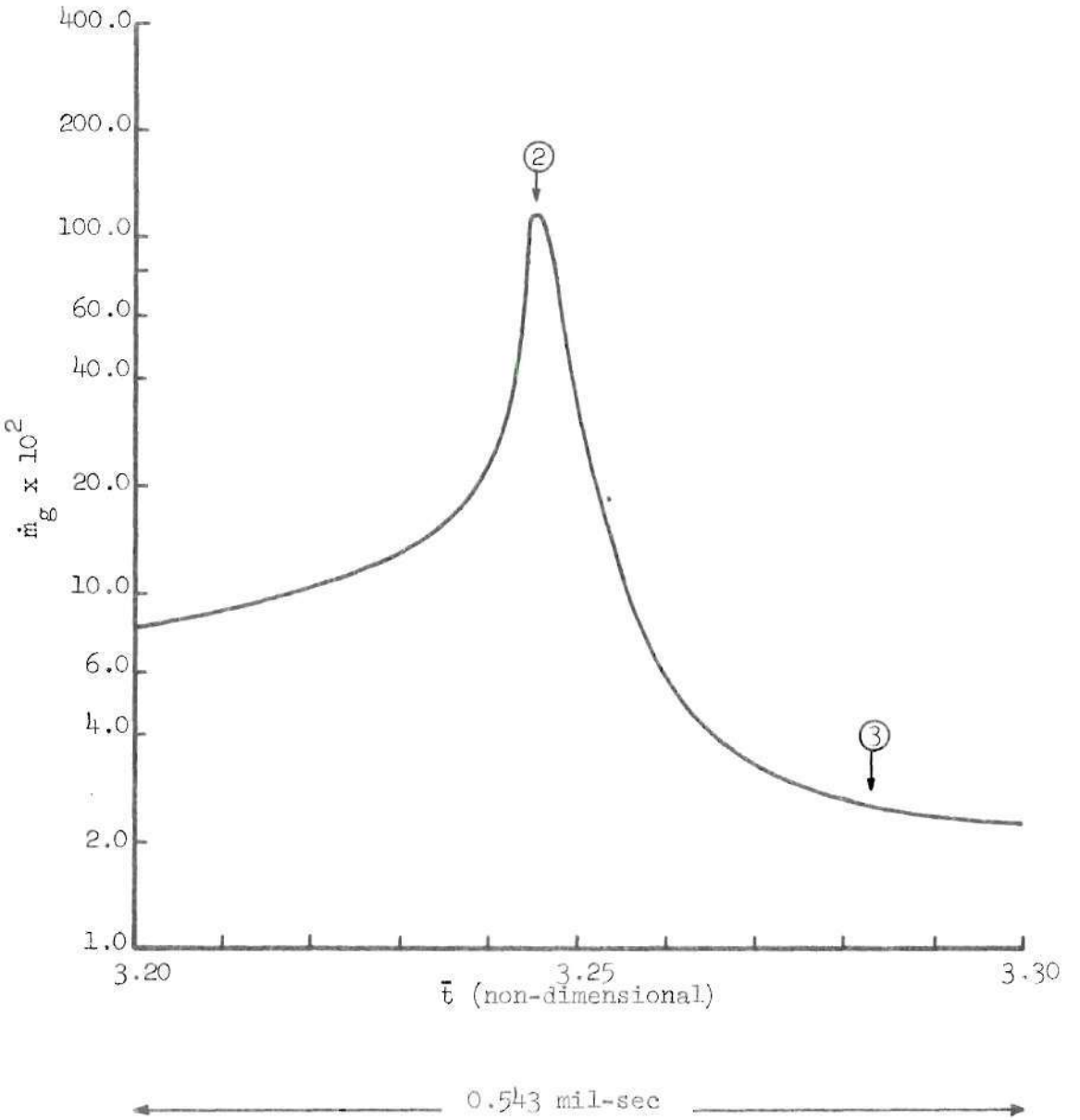

Figure 44. Expanded View of "Spike" in Propellant Burning Rate Occurring Between $\bar{t} = 3.20$ and $\bar{t} = 3.30$ in Figure 43d

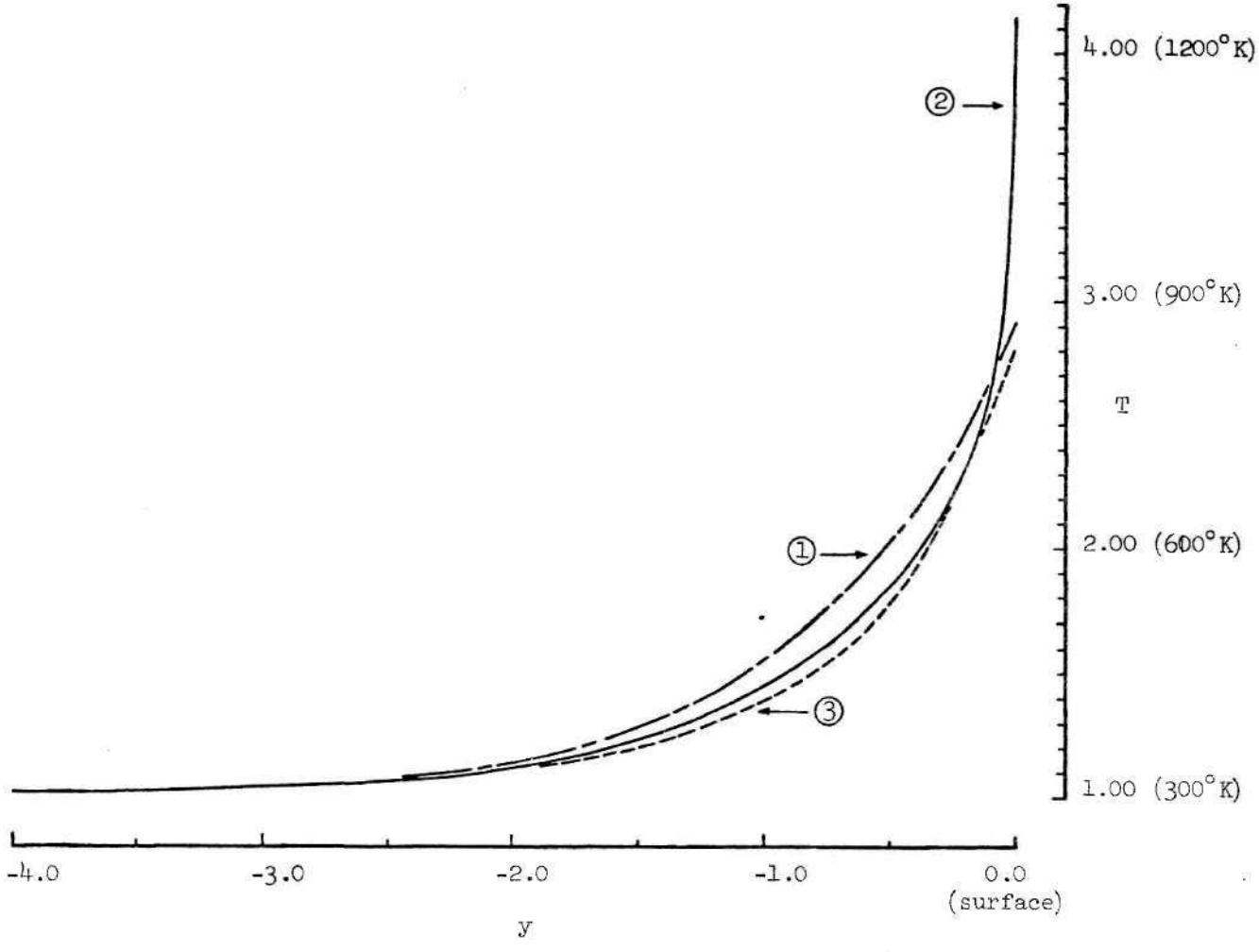

Figure 45. Temperature Distributions in Unburned Solid Propellant During Burning Rate Spike Shown in Figure 44: 1, Before ($\bar{t}$ = 3.088); 2, At Peak ($\bar{t}$ = 3.245); 3, After ($\bar{t}$ = 3.283)

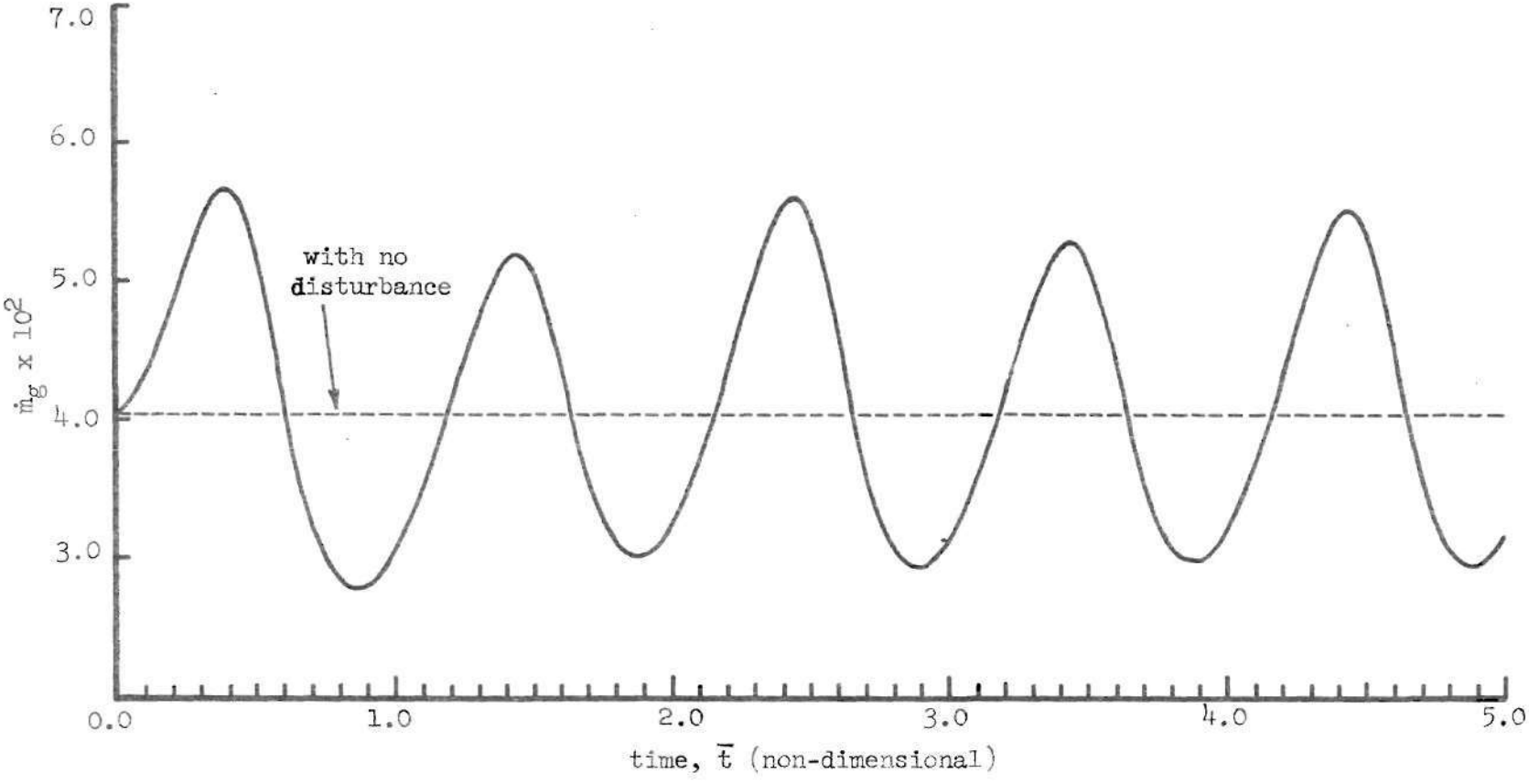

Figure 45. Combustion Response to a Ten Percent Amplitude Sinusoidal Pressure Oscillation at $\Omega = 11.0$ for the Propellant System in Case (9)

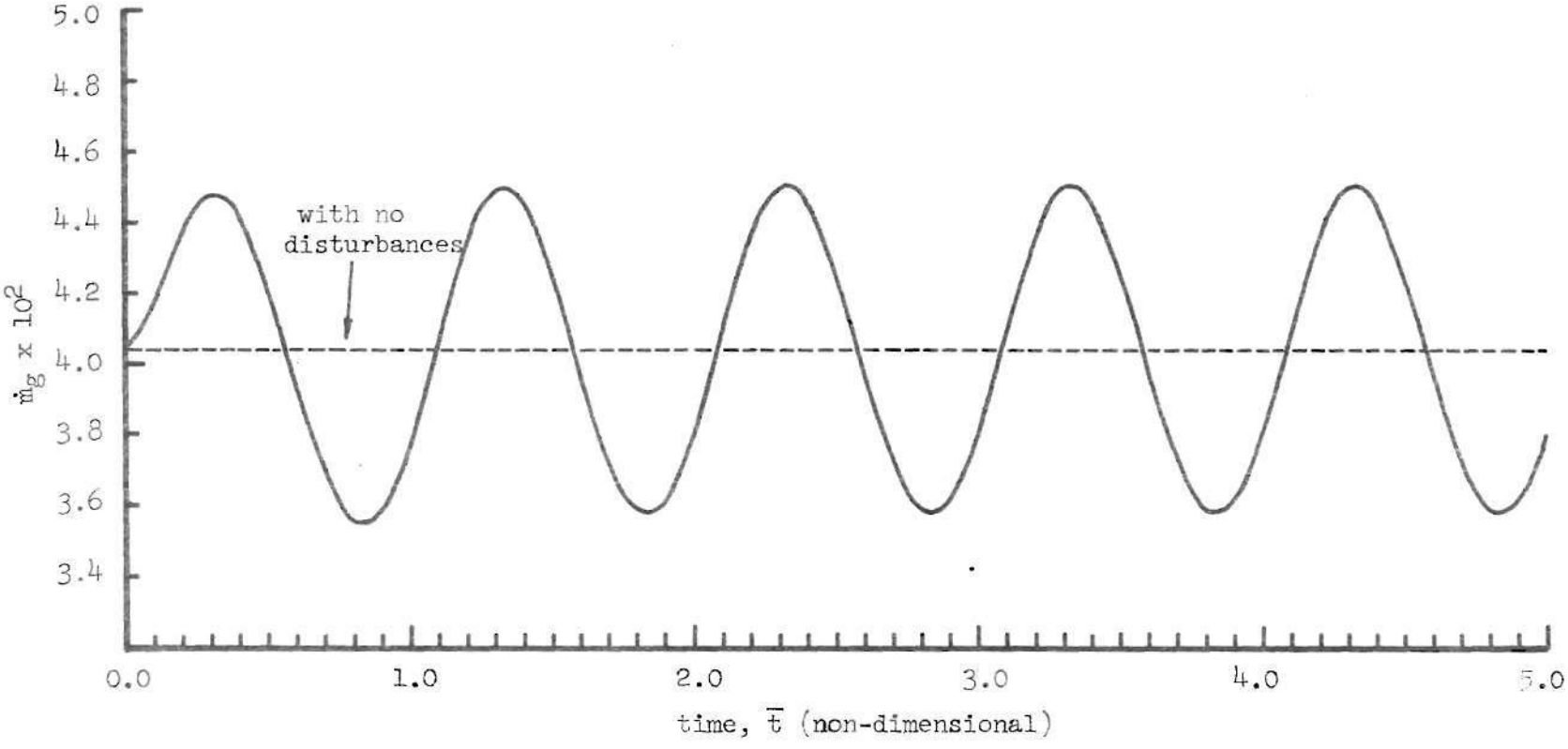

Figure 47. Combustion Response to a Ten Percent Amplitude Sinusoidal Pressure Oscillation at $\Omega = 5.5$ for the Propellant System in Case (9), Altered with $E_s^* = 10$ kcal/mole

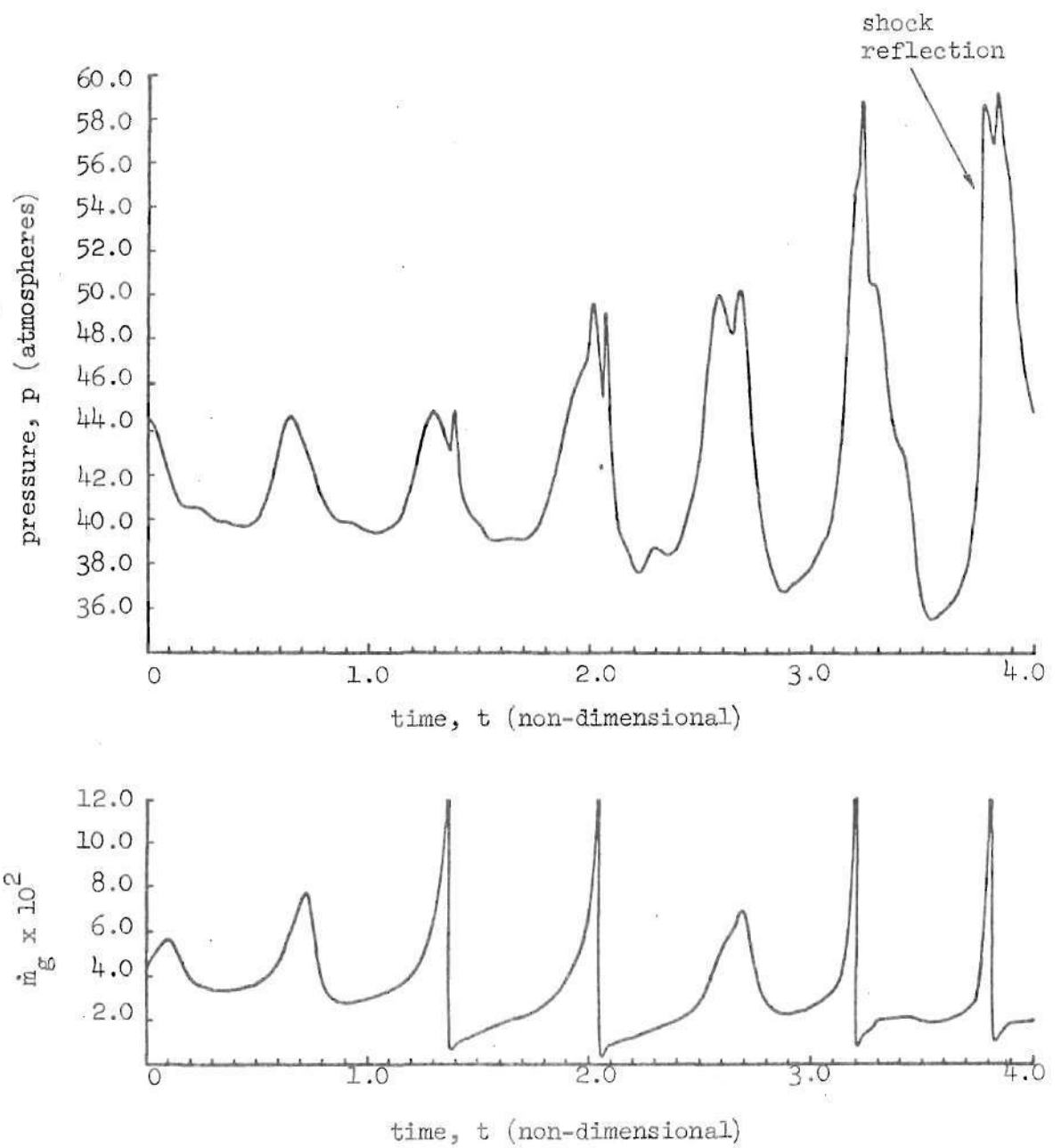

Figure 48. Time History of Pressure and Propellant Mass Flow Rate at the Head End of the Combustion Chamber as the Result of a Ten Percent Amplitude Continuous Disturbance on the Steady State Flow Field of Case (9)

LITERATURE CITED

1. Price, E. W., "Axial Mode, Intermediate Frequency Combustion Instability in Solid Propellant Rocket Motors," AIAA paper 64-146, presented at AIAA Solid Propellant Rocket Conference, Palo Alto, Calif., January 1964.

2. Price, E. W. and Dehority, G. L., "Velocity Coupled Axial Mode Combustion Instability in Solid Propellant Rocket Motors," presented at the Second ICRPG/AIAA Solid Propulsion Meeting, Anaheim, Calif., June 1967.

3. Price, E. W., "Experimental Solid Rocket Combustion Instability," proceedings of the Tenth Symposium (International) on Combustion, the Combustion Institute, Pittsburgh, Pa., 1965.

4. Fowler, J. R. and Rosenthal, J. S., "Missile Vibration Environment for Solid Propellant Oscillatory Burning," AIAA paper 71-756, 1971.

5. Bergman, G. H. and Jessen, E. C., "Evaluation of Conventional Rocket Motor Instrumentation for Analysis of Oscillatory Combustion," AIAA paper 71-755, 1971.

6. Browning, S. C., Kraskin, M., and Thacker, J. H., "Application of Combustion Instability Technology to Solid-Propellant Motor Problems," AIAA paper 71-758, 1971.

7. Brownlee, W. G., "Nonlinear Axial Combustion Instability in Solid Propellant Rocket Motors," AIAA J., Vol. 2, No. 2, pp. 275-284, (Feb. 1964).

8. Brownlee, W. G. and Roberts, A. K., "Investigations of Nonlinear Axial Combustion Instability in Solid Propellant Rocket Motors," AIAA paper 63-474, 1963.

9. Dickinson, L. A., "Command Initiation of Finite Wave Axial Combustion Instability in Solid Propellant Rocket Motors," ARS J., Vol. 32, pp. 643-644, (April 1962).

10. Brownlee, W. G. and Kimbell, G. H., "Shock Propagation in Solid-Propellant Rocket Combustors," AIAA J., Vol. 4, No. 6, pp. 1132-1134, (June 1966).

11. Roberts, A. K., Brownlee, W. G., and Jackson, F., "Combustion Instability and Design of Solid Propellant Rocket Motors," Canadian Aeronautics and Space J., Vol. 16, No. 1, pp. 21-27, (Jan. 1970).

12. Roberts, A. K. and Brownlee, W. G., "Nonlinear Longitudinal Combustion Instability: Influence of Propellant Composition," AIAA J., Vol. 9, No. 1, pp. 140-147 (Jan. 1971)

13. Capner, E. L., Dickinson, L. A., and Krier, R. J., "Driving Processes of Finite Amplitude Axial Mode Instability in Solid Propellant Rockets," AIAA J., Vol. 5, No. 5, pp. 938-945 (May 1967).

14. Marxman, G. A. and Wooldridge, C. E., "Finite-Amplitude Axial Instability in Solid Rocket Combustion," preceedings of the Twelfth (International) Symposium on Combustion, the Combustion Institute, Pittsburgh, Pa., pp. 115-127 (1969).

15. Morris, E. P., "A Pulse Technique for the Evaluation of Combustion Instability in Solid Propellant Rocket Motors," Canadian Aeronautics and Space J., Vol. 11, No. 9, pp. 329-333 (Nov. 1965).

16. Summerfield, M., Sutherland, G. S., Webb, M. J., Taback, H. J., and Hall, K. P., "Burning Mechanism of Amonium Perchlorate Propellants," in Progress in Astronautics and Rocketry - Vol. 1, ed. M. Summerfield, pp. 141-182, Academic Press, 1960.

17. Steinz, J. A., Stang, P. L., and Summerfield, M., "The Burning Mechanism of Amonium Perchlorate - Based Composite Solid Propellants," AIAA paper 68-638, 1968.

18. Cheng, S.-I., "High Frequency Combustion Instability in Solid Propellant Rockets," Jet Propulsion, Pt. 1, pp. 27-32, Pt. 2, pp. 102-109, 1954.

19. Cheng, S.-I., "On Unstable Burning of Solid Propellants," Jet Propulsion, Vol. 25, pp. 79-80, Jan. 1955.

20. Cheng, S.-I., "Unstable Combustion in Solid-Propellant Rocket Motors," Eighth Symposium (International) on Combustion, pp. 81-96, 1962.

21. Crocco, L., and Cheng, S.-I., "Theory of Combustion Instability in Liquid Propellant Rocket Motors," AGARDograph 8, Butterworths, London, 1956.

22. Crocco, L., Grey, J., and Harrje, D. T., "Theory of Liquid Propellant Rocket Combustion Instability and its Experimental Verification," ARS J., Vol 30, No. 2, pp. 159-168, Feb. 1960.

23. Crocco, L., "Theoretical Studies on Liquid Propellant Rocket Instability," Tenth Symposium (International) on Combustion, The Combustion Institute, Pittsburgh, Pa., pp. 1101-1128, 1964.

24. Grad, H., "Resonance Burning in Rocket Motors," Comm. Pure Applied Math., Vol. 2, pp. 79-102, March 1949.

25. Moore, F. K., and Maslen, S. H., "Transverse Oscillations in a Cylindrical Combustion Chamber," NACA TN 3152, October 1954.

26. Culick, F. E. C., "A Review of Calculations for Unsteady Burning of a Solid Propellant," AIAA J., Vol. 6, No. 12, pp. 2241-2255, (December 1968).

27. Beckstead, M. W., and Culick, F. E C., "A Comparison of Analysis and Experiment for Solid Propellant Combustion Instability," AIAA J., Vol. 9, No. 1, pp. 147-154 (January 1971).

28. Price, E. W., "Comments on 'Role of Aluminum in Suppressing Instability in Solid Propellant Rocket Motors'," AIAA J., Vol 9, No. 5 pp. 987-990, (May 1971).

29. McClure, F. T., Bird, J. F., and Hart, R. W., "Erosion Mechanism for Nonlinear Instability in the Axial Modes of Solid Propellant Rocket Motors," ARS J., Vol. 32, No. 3, pp. 374-378, (March 1962)

30. Hart, R. W., Bird, J. F., and McClure, F. T., "The Influence of Erosive Burning on Acoustic Instability in Solid Propellant Rocket Motors," included in Progress in Astronautics and Rocketry, Vol. 1, ed. M. Summerfield, Academic Press, N. Y., 1960, pp. 423-499.

31. Bird, J. F., Hart, R. W., and McClure, F. T., "Finite Acoustic Oscillations and Erosive Burning in Solid Fuel Rockets," AIAA J., Vol. 3, No. 12, pp. 2248-2256 (December 1965).

32. Peretz, A., Kuo, K. K., Caveny, L. H., and Summerfield, M., "The Starting Transient of Solid-Propellant Rocket Motors With High Internal Gas Velocities," AIAA paper 72-1119, 1972.

33. Culick, F. E. C., "Stability of Longitudinal Oscillations With Pressure and Velocity Coupling in a Solid Propellant Rocket," Combustion Science and Technology, Vol. 2, No. 4, pp. 179-201 (1970).

34. Levine, J. N., and Culick, F. E. C., "Numerical Analysis of Nonlinear Longitudinal Combustion Instability in Metalized Propellant Solid Rocket Motors," presented at Ninth JANNAF Combustion Meeting, Sept. 1972, Monterey, Calif. (see CPIA publication 231, Dec. 1972, pp. 141-163).

see also Technical Report, AFRPL-TR-72-88.

35. Korman, H. F. and Michele, P. L., "Nonlinear Particulate Damping of Acoustic Oscillations," presented at the Eighth JANNAF Combustion Meeting, September 1971, Monterey, Calif. (see CPIA publication 220, pp. 345-356, Nov. 1971).

36. Cheng, S. I., "Numerical Integration of the Navier-Stokes Equations," AIAA J., Vol. 8, No. 12, pp. 2115-2122 (December 1970).

37. Bowley, W. W. and Prince, J. F., "Finite Element Analysis of General Fluid Flow Problems," AIAA paper 71-602 (1971).

38. Kutler, P. and Lomax, H., "A Systematic Development of the Supersonic Flowfield Over and Behind Wings and Wing-Body Configurations Using a Shock-Capturing Finite-Difference Approach," presented at the Ninth AIAA Aerospace Sciences Meeting, AIAA paper 71-99 (1971).

39. MacCormack, R. W., "The Effect of Viscosity in Hypervelocity Impact Cratering," AIAA paper 69-354 (1969).

40. Moretti, G., "Complicated One-Dimensional Flows," PIBAL Report 71-25, Polytechnic Institute of Brooklyn, September 1971.

41. Moretti, G., "The Choice of a Time-Dependent Technique in Gas Dynamics," PIBAL Report 69-26, Polytechnic Institute of Brooklyn, July 1969.

42. Moretti, G., "A Critical Analysis of Numerical Techniques: The Piston-Driven Inviscid Flow," PIBAL Report 69-25, Polytechnic Institute of Brooklyn, July 1969.

43. Richtmyer, R. D. and Morton, K. W., Difference Methods for Initial Value Problems, Interscience Publishers, N. Y., 2nd ed., 1967 p. 300.

44. Davidon, W. C., "Variance Algorithm for Minimization," Computer J., Vol. 10, No. 4, pp. 406-411 (February 1968).

45. Straeter, T. A. and Hogge, J. E., "A Comparison of Gradient Dependent Techniques for the Minimization of an Unconstrained Function of Several Variables," AIAA J., Vol. 8, No. 12, pp. 2226-2229, (December 1970).

46. von Neumann, J. and Richtmyer, R. D., "A Method for the Numerical Calculation of Hydrodynamic Shocks," J. of Applied Physics, Vol. 21, 1950, pp. 232-237.

47. Courant, R., Friedrichs, K. O. and Lewy, H. L., "Ueber die Partiellen Differenzgleichungen der Mathematischen Physik," Math. Ann., Vol. 100, 1928, pp. 32-74.

48. Kentzer, C. P., "Group Velocity and Propagation of Numerical Errors," AIAA paper 72-153 (1972).

49. Galaher, L., Georgia Institute of Technology, private communication.

50. Kumar, R. N. and Culick, F. E. C., "Role of Condensed Phase Details

in the Oscillatory Combustion of Composite Propellants," AIAA paper 73-218 (1973).

51. Meyer, G. H., Initial Value Methods for Boundary Value Problems (Theory and Application of Invariant Imbedding), 100th Volume in the series Mathematics in Science and Engineering, ed. R. Bellman, Academic Press, N. Y., 1973.

52. Lee, E. S., Quasilinearization and Invariant Imbedding, Volume 41 in series Mathematics in Science and Engineering, Academic Press, N. Y., 1968.

53. Vichnevetsky, R., "A New Stable Computing Method for the Serial Hybrid Computer Integration of Partial Differential Equations," Proceedings of the 1968 Spring Joint Computer Conferences, AFIPS, Vol. 32, Thompson Books, 1968.

54. Sneddon, I. N., Elements of Partial Differential Equations, McGraw-Hill, 1957.

55. Most, W. J., MacDonald, B. W., Stang, P. L. and Summerfield, M., "Thrust Transient Prediction and Control of Solid Rocket Engines," Paper 68-33, presented at the Western States Section of the Combustion Institute, Menlo Park, Calif., October 1968.

56. Krier, H., T'ien, J. S., Sirignano, W. A., and Summerfield, M., "Nonsteady Burning Phenomena of Solid Propellants: Theory and Experiments," AIAA J., Vol. 6, No. 2, pp. 278-285, (February 1968).

57. Waesche, R. H. W., Wenograd, J., and Summerfield, M., "Research on Solid Propellant Combustion Instability," Aeronautical Engineering Report 564b, Dec. 1961, Princeton University.

58. Waesche, R. H. W., Wenograd, J., and Summerfield, M., "Entropy Wave Observations in Oscillatory Combustion of Solid Propellants: A Progress Report," AIAA paper 64-154, 1964.

59. Merkle, C. L., Turk, S. L., and Summerfield, M., "Extinguishment of Solid Propellants by Depressurization: Effects of Propellant Parameters," AIAA paper 69-176, 1969.

60. Peretz, A., Kuo, K. K., Caveny, L. H., and Summerfield, M., "The Starting Transient of Solid-Propellant Rocket Motors With High Internal Gas Velocities," AIAA paper 72-1119, (1972).

61. Kuo, K. K., "Theory of Flame Front Propagation in Porous Propellant Charges Under Confinement," Ph.D. Dissertation, Princeton University, August 1971.

62. Kitchens, C. W., "Characteristic Theory Applied to Flame Spreading in Porous Propellants," Ballistic Research Labs, Aberdeen Proving

Ground, October 1972.

63. Glass, I. I., and Hall, J. G., "Handbook of Supersonic Aerodynamics: Shock Tubes," Bureau of Naval Weapons, Navord Report 1488, Vol. 6, 1959.

64. Beckstead, M. W., Derr, R. L., and Price, C. F., "The Combustion of Solid Monopropellants and Composite Propellants," proceedings of the Thirteenth Symposium (International) on Combustion, The Combustion Institute, Pittsburgh, Pa., 1971, pp. 1047-1056.

VITA

Douglas Edward Kooker was born on November 2, 1942 in Cleveland Heights, Ohio and was graduated from Cleveland Hieghts High School in June, 1960. From 1960 to 1966, he attended Purdue University and was awarded a B. S. in Engineering Science in 1964 and a M. S. in Engineering Science in June, 1966. He was employed with Lockheed Missiles and Space Company, Huntsville Research and Engineering Center, Huntsville, Alabama from 1966 to 1969 as a Thermodynamics Engineer in the Aeromechanics Department. His work was involved with laminar and turbulent boundary layers, low density heat transfer, stage separation problems on the SATURN-V Rocket, and transonic flow in liquid propellant rocket engines. From 1969 to 1973, he was a graduate student in the School of Aerospace Engineering, Georgia Institute of Technology working toward the Ph.D. degree. During this time, he was supported by a three-year NDEA fellowship and a graduate research assistantship.

He is married to the former Ellyn Carol Smolik and they have one son, David Merrill Kooker.